NANYANG
TECHNOLOGICAL
UNIVERSITY

ON-LINE MONITORING OF PARTICULATE PROCESSES USING DIGITAL HOLOGRAPHY

TASLIMA KHANAM

School of Chemical and Biomedical Engineering

A thesis submitted to the Nanyang Technological University
in partial fulfillment of the requirement for the degree of
Doctor of Philosophy
2010

Acknowledgement

At the foremost, all praises to the Almighty for assisting me with patience and consistency during the whole work of my PhD studies. Then I would like to extend my most sincere acknowledgments and gratitude to a number of people whose help, support and suggestions were immensely valuable in my research.

The first person to whom I owe my deepest gratitude is my supervisor, Asst. Prof. Arvind Rajendran. I am greatly thankful to him as he accepted me as a PhD student and spent lots of his valuable time and effort in providing help, support, encouragement and guidance to enhance my ability in research. He taught me the scientific approach of thinking, writing and presenting until the end of the project. Besides my supervisor, another person was always there to help me providing continuous support, suggestions and guidance. This person is Asst. Prof. Vinay Kariwala, my co-supervisor. I also express my sincere gratitude to him for guiding me equally as my supervisor. I feel privileged to get the opportunity to conduct my research work under the supervision of such wonderful supervisors .

Secondly, I gratefully thank Prof. Anand Krishna Asundi, our main collaborator, to allow me accessing their lab and instruments facilities, and to provide valuable suggestions for relevant optical improvement in my work.

Then, I would like to offer special thanks to Dr. Emmanouil Darakis who had given his valuable time, guided me in understanding basics of digital holography and related algorithms. I also express my sincere thanks to Dr. Michel Kempkes, Mr. Di Jianglei,

Dr. Vijay Raj Singh and Dr. Xiujuan for spending their important time with me providing valuable tips.

Lastly, I sincerely express my deepest gratitude and love to my beloved parents for their support and encouragement who made my dream of higher studies a reality. I am specially thankful to my husband, Mabrur Rashedi who accompanied me for the last four years by not making me feel alone and depressed during my study in abroad and encouraged me all the time.

Abstract

For particulate processes, such as crystallization, polymerization and granulation, particle imaging has been proven to be an effective technique for on-line particle size and shape measurement. Imaging based methods extract size and shape information from acquired images using image analysis algorithms. The successful application of image analysis algorithms for conventional 2D imaging systems is not straight-forward. It is often hindered by the problems of limited depth of focus imposed by required magnification as well as undetermined perspective position and random orientation of the particles. Thus, conventional imaging systems provide 2D information about the 3D scene, which can result in inaccurate inference of particle's 3D size and shape.

In this work, we propose a novel method to accurately characterize the properties of microparticles using digital holography. In digital holography, the interference pattern between two coherent light beams is recorded. This interference pattern contains information about the entire volume of the sample which can be numerically reconstructed for focusing at different planes of the volume. Thus, 3D information can be obtained using a single hologram by reconstructing it at different depths. This distinct advantage allows digital holography to overcome the aforesaid limitations of the 2D imaging systems. This work explores the potential of digital holography as a tool for online measurement of size and shape of micro particles. The first part of the thesis deals with the development of a technique to obtain 2D information of particles. The system was validated for both spherical and non-spherical (needle shaped) particles. The results from holography are

shown to be fully consistent with those from independent techniques such as scanning electron microscopy. While 2D information is sufficient to describe spherical particles, it does not provide accurate information concerning non-spherical, especially needle-shaped particles. An accurate measurement of the lengths is possible only if the orientation can be unambiguously measured. In order to address this problem, two novel techniques have been developed which simultaneously measure the location, orientation and length of a population of fibers. These have demonstrated by careful validation using single fibers and applied to a fiber population. Finally the technique has been applied to monitor the crystallization of transparent crystals of oxalic acid and measured their growth rate.

These results adequately demonstrate the potential of digital holography as a reliable tool for the online monitoring of particulate processes.

Publications Related to the Thesis

Journal Papers

1. M. Kempkes, E. Darakis, **T. Khanam**, A. Rajendran, V. Kariwala, M. Mazzotti, T. J. Naughton, A. K. Asundi. Three dimensional digital holograhic profiling of microfibers. *Opt. Express*, 17(4):2938-2943, 2009.
2. E. Darakis, **T. Khanam**, A. Rajendran, V. Kariwala, T. J. Naughton, A. K. Asundi. Microparticle characterization using digital holography. *Chem. Eng. Sci.*, 65(2):1037-1044, 2010.
3. **T. Khanam**, M. N. Rahman, A. Rajendran, V. Kariwala, A. K. Asundi. Accurate characterization of needle-shaped particles using digital holography. Submitted to *Chem. Eng. Sci.*, 2010.
4. **T. Khanam**, A. Rajendran, V. Kariwala, A. K. Asundi. Monitoring crystal size and growth using digital holography. In preparation.

Book Chapters

1. "Digital In-line Holography and Applications", Chap. 4 in *Digital Holography for MEMS and Microsystem Metrology*, ed. Anand K. Asundi, John Wiley & Sons Ltd., submitted.

Publications in conference proceedings

1. **T. Khanam**, E. Darakis, A. Rajendran, V. Kariwala, A. K. Asundi, T. J. Naughton. Online digital holographic measurement of size and shape for crystallization processes. *Proceedings of SPIE - The International Society for Optical Engineering*, 71551(71551K):1-10, 2008.

2. **T. Khanam**, E. Darakis, A. Rajendran, V. Kariwala, A. K. Asundi, T. J. Naughton. Particle size and shape measurement using digital holography. *15th Regional Symposium on Chemical Engineering*, 2008.

3. E. Darakis, **T. Khanam**, A. Rajendran, V. Kariwala, A. K. Asundi, T. J. Naughton. Processing of digital holograms for size and shape measurements of microparticles. *Proceedings of SPIE - The International Society for Optical Engineering*, 7155(715524):1-12, 2008.

4. E. Darakis, M. Kempkes, **T. Khanam**, A. Rajendran, V. Kariwala, M. Mazzotti, T. J. Naughton, A. K. Asundi. Localization of Microfibers within Volumes Using Digital Holographic Video. *OSA Digital Holography and Three-Dimensional Imaging, Vancouver, Canada*, 2009.

5. A. Asundi, V.R. Singh, W.J. Qu, **T. Khanam**. Compact digital holographic microscope and applications. *Conference on Lasers and Electro-Optics/Pecific Rim (CLEOPR)*, Shanghai, China (Optical Society of America), 2009.

Presentations in Conferences

1. **T. Khanam**, M. Nurur Rahman, A. Rajendran, V. Kariwala, A. K. Asundi. Direct measurement of length and orientation of microfibers in solution. *American Institutes of Chemical Engineers Annual Meeting*, Salt Lake City, UT, 2010.

2. **T. Khanam**, M. Nurur Rahman, A. Rajendran, V. Kariwala, A. K. Asundi. Direct measurement of length and orientation of microfibers in solution. *9th International Workshop on Crystal Growth of Organic Material*, Singapore, 2010.

3. **T. Khanam**, M. Nurur Rahman, Di. Jianglei, A. Rajendran, V. Kariwala, A. K. Asundi. Digital holography: A novel tool for characterization of near-micron sized particles. *9th International Workshop on Crystal Growth of Organic Material*, Singapore, 2010.

4. **T. Khanam**, E. Darakis, A. Rajendran, V. Kariwala, A. K. Asundi. Two and three dimensional microparticle characterization using digital holography. *American Institutes of Chemical Engineers Annual Meeting*, Nashville, TN, 2009.

5. **T. Khanam**, A. Rajendran, V. Kariwala, A. K. Asund. 3D Micro-fiber Measurements Using Digital Holography. *4th International conference on experimental mechanics*, Singapore, 2009.

6. M. Kempkes, E. Darakis, **T. Khanam**, A. Rajendran, V. Kariwala, M. Mazzotti, A.K. Asundi, T. Naughton. Three dimensional size measurement of needle shaped particles by digital holography. *17th International Symposium on Industrial Crystallization (ISIC)*, Maastricht Netherlands, 2008.

Contents

List of Figures

List of Tables

Nomenclature

a	[μm]	Major axis length
b	[μm]	Minor axis length
D	[cm]	Distance between the point source and CCD used for recording
D'	[cm]	Distance between the point source and CCD used for reconstruction
d	[mm]	Object distance
d'	[mm]	Reconstruction distance
d_{eq}	[μm]	Circle equivalent diameter
$I(x, y)$	[-]	Intensity of recorded hologram
L	[μm]	Real length
L_p	[μm]	Projected length
L_c	[μm]	Centroid to centroid distance between two segments of projected length
$M(d)$	[-]	Lateral magnification
$N_x \times N_y$	[-]	Number of pixels of CCD array
N_z	[-]	Number of reconstructions along optical axis
O	[μm]	Actual object size
O'	[μm]	Measured object size
U_R	[-]	Reference beam
U_d	[-]	Object beam
U	[-]	Object beam at camera plane

$U_{d'}$	[-]	Object beam at reconstructed plane
(x, y)	[-]	Hologram or camera plane
(x', y')	[-]	Reconstructed image plane
$(\Delta x, \Delta y)$	[μm$\times\mu$m]	CCD pixel size
$(\Delta x', \Delta y')$	[μm$\times\mu$m]	Reconstructed image pixel size
z	[-]	Optical axis
λ	[nm]	Wavelength used for recording hologram
λ'	[nm]	Wavelength used for reconstruction
θ	[$^\circ$]	Tilt out of the camera plane

Abbreviations

ALD	Axis Length Distribution
API	Active Pharmaceutical Ingredients
CCD	Charged Couple device
CE	Circle Equivalent
CSD	Crystal Size Distribution
CLD	Chord Length Distribution
DOF	Depth of Focus
FBRM	Focused Beam Reflectance Measurement
LDHM	Lensless Digital Holographic Microscopy
PAT	Process Analytical Tool
PSD	Particle size distribution
PVC	Poly Vinyl Chloride
PVM	Particle Vision Microscope
USAF	'United States Air Force' resolution test target
2D	Two Dimensional
3D	Three Dimensional

Chapter 1

Introduction to microparticle characterization

Processing of particulates, either as intermediates or as final products is ubiquitous in chemical process industries. For instance, a significant percentage of pharmaceutical products are manufactured as solid forms. Paint, cement, detergent industries process several tonnes of solids as well. In most of these processes, the characteristics of the particles, *e.g.*, size, shape, etc. impact the corresponding physiochemical properties of the final product. Hence one of the primary aims in these industries is to monitor and measure these characteristics to control process and product requirements. Herein, we list a few industrial processes where particle sizes and shape affect the process or product quality.

- **Pharmaceutical manufacturing:** It is estimated that 80% of pharmaceutical products are marketed as solid form. Typical unit operations, where particles are involved, include crystallization, filtration, milling and granulation. Crystallization is an important process for the manufacturing of active pharmaceutical ingredients [2]. The crystallization step is usually succeeded by a series of unit operations such as filtration, washing, drying, mixing, milling and granulation, before the final product

is obtained and is ready for use [3, 4]. In all these steps, the size and shape of the particles are of key importance. For example, during filtration process one should avoid platelet shaped particles if cake resistance is an issue [5, 6]; good powder flowability and high packing density would require compact, rather than needle shaped particles [7]. Further, in pharmaceutical processes, both crystal size and shape significantly affect the dissolution properties of the drug and hence its efficacy [8, 9]. Hence, it is important to measure crystal shape and size distribution in order to ensure desired product quality.

- **Cement industry:** Cement is a gray powder that is used with water to give strength into the concrete upon hardening. Cement manufacturing process is one of the highest energy consuming processes in the world. Most of the energy in this process is used during its back and forth grinding and crushing to obtain desired particle size. The fineness of particles is a critical parameter for the performance of cement. Extremely fine particles result in large surface areas and are prone to propagate cracking due to fast settling and exothermic curing of the cement [10]. On the other hand, coarse particles result in inefficient hydration reaction which reduces the strength of the cement. Hence, maintaining particle size within the desired specification is a critical step and can be achieved by on-line monitoring.

- **Ceramic:** The production of ceramic involves the following key steps: preparation of raw materials by mining and milling of raw materials, dispersion of the ceramic powders into liquid, compacting them in a mold to form desired shape and subsequent heat treatment to form a mechanically strong ceramic product [11]. Particle size and size distribution during the milling step of ceramic powder production greatly affect the stability of ceramic dispersion process in the liquid and the compactness during molding, thereby determines the strength and the quality of the finished product [12, 13]. Therefore, particle size analysis tool is required during

the milling process to control the product quality as per requirements.

- **Food processing industry:** A wide variety of food products involve particulate matter, such as, refined sugar, chocolate, milk powder, flour, instant coffee powder, cream and so on. The taste, texture, color, dissolution rates, viscosity, packing, all these quality of these products are greatly influenced by the particle size and shape [14]. Hence to ensure a desired quality of the product, the particle size and shape measurement is very important during their processing.

- **Paints and coatings:** Paint usually consists of pigments (particles), binder (usually oil or resin) and thinner (usually an organic solvent). In paint manufacturing process, the solid pigment particles that determine the color, durability and opacity of the paint are mixed with binders which is used to hold the solids and cause them adhere to the surface to be coated. The thinner is then mixed with the paste of binders and pigments to adjust the viscosity according to the requirements [15]. It has been reported that the size and shape of pigments and resin particles greatly affect the tint strength, durability, transparency and viscosity of the paint [15]. Hence there exists a demand for rapid and accurate particle measurement tool to ensure the quality of the paint.

From the examples highlighted above it is rather obvious that an accurate and robust measurement tool is indispensable for on-line measuring of particle size and shape in particulate process. Advancements in monitoring technologies and an increasing push from regulatory authorities have prompted industries to incorporate process analytical technologies (PAT) in their manufacturing process. PAT identifies key measures of product quality in addition to relevant process variables, appropriate measurement devices, statistical and information technology tools and feedback control strategies. These all work together to ensure production of final products with the desired quality.

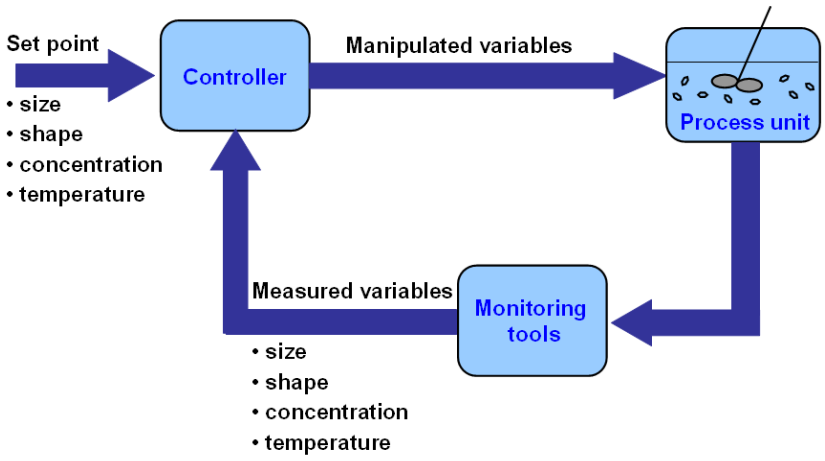

Figure 1.1: Feedback control system for a particulate process.

A schematic of feedback control scheme for a particulate process that finds it's scope within PAT framework, is shown in Fig. 1.1. The system consists of three major elements: the process unit, monitoring tools and the controller. In the process unit, key formulation or manufacturing processes are carried out. Such as, crystallization for manufacturing active pharmaceutical ingredients (API), comminution for manufacturing of cement or ground coffee, polymerization for making poly vinyl chloride (PVC) and so on. The on-line monitoring tools are used to measure key process parameters, such as particles' size, shape, solution concentration, temperature and so on. These 'measured' variables' are compared with the desired 'set-points' by the controller which then decides upon the control action by suitably adjusting the process conditions, i.e 'manipulated variables'. Similar control systems are used in emulsion polymerization [16–21], granulation processes [22, 23] and crystallization process [4,24,25]. It can be inferred from the schematic that an accurate and robust on-line monitoring tool is vital to achieve the desired control objectives. In addition to control objectives, these tools have also been used to study the kinetics of nucleation and growth of crystals [1, 26–28], sedimentation and settling of particles [29], polymer detection [19, 20] and waste water treatment [30]. Hence the development of appropriate tool for on-line and precise particle size and shape measurement is of great interest for the

researchers and industry.

The thesis is part of a program to develop tools for measuring size and shape of particles where the interest is to measure particles in the size range of 1 to 1000μm. While several particle characterization techniques are available, we limit our review to ones that have been widely used for measuring and monitoring particles characteristics. Table 1.1 summarizes some of these particle sizing methods along with their working principles, sizing ranges and measured attributes.

Table 1.1: List of commonly used particle measurement tools

Tool	*Working principle*	*Measured size range (μm) (μm)*	*Measured attribute*	*Position of the tool*
Sieve analysis	particle screening	5-10000	Particle diameter	off-line
Sedimentation method	particle settling	0.05-100	Particle diameter	off-line
Coulter counter	Electrical sensing	0.4-1200	Particle volume	off-line
Ultrasonic extinction	Ultrasound attenuation	0.01-1000	volume based PSD	on-line
Laser diffraction	Forward light scattering	0.02-2000	Scattering pattern	off-line
FBRM	Backward light scattering	0.8-1000	Chord length	in-situ/on-line
PVM	Imaging	3-1000	2D particle size	in-situ/on-line
Raman spectroscopy	Inelastic light scattering	not applicable	morphology	in-situ

1.1 Tools for particle characterization

1.1.1 Sieve analysis

Sieve analysis is relatively older technology. It utilizes a test sieve or a set of sieves of uniform openings for material classification. As materials are of different fractions, the fractions larger than the openings retain on the screen while the smaller ones pass through easily. Sieves are usually designated by a 'mesh' number, which is related to the number of parallel wires per inch in the weave of the sieve. The sizing range for sieving is from 5 μm to a few tenths of a millimeter. Although a classical technique, sieve analysis has been widely used for various off-line measurements because of its inherent simplicity in principle and procedure. The application of sieve analysis is widely found for various off-line measurements, such as, measurement of sand particles in sand control applications for efficient extraction of petroleum deposits [31, 32], measurement of granule size in granulation process [33, 34], measurement of desired grain size in crushing and milling operations [35, 36] and so on.

This method, nevertheless, carries some salient drawbacks. First of all, the application of sieve analysis is limited to off-line measurements. Secondly, result from sieve analysis varies with the method of moving the sieve or particles, the geometry of sieve surface (sieve type, fractional open area, etc.), the time length of operation, the number of particles on the sieve, and the physical properties of particles (such as their shape, stickiness, and brittleness). For example, a three-dimensional particle of any shape can pass through an opening depends on the orientation of the particle, which usually depends on the mechanics of shaking the sieve or the particle itself, as well as the time length of such shaking [37].

1.1.2 Sedimentation

Sedimentation is another classical particle characterization technique for liquid-born particles. This method works based on measuring the settling velocity of particles in a liquid at rest under a gravitational or centrifugal field. In this method particle sizes are obtained from the Stokes equation [38]. Stokes law defines the relationship between a diameter of spherical particle and it's settling velocity when it flows slowly in liquid without interference of other forces or motions. Thus, the measurement of particle size from sedimentation approach requires a system with low Reynolds number. Hence, to satisfy this conditions, the application of the method is limited to the low concentration system with particles in a certain size range. Sedimentation methods have been widely used during the past for the study of microbial ecology [39], soil testing [40], characterization of industrial mineral [41] and characterization of airborne dust in coal mines [42]. Despite its wide usage, there are some limitations associated with sedimentation. At low Reynolds numbers non-spherical particle can have random orientation. Depending on their orientation a wide range of settling velocities of particles can be experienced. Thus, for a polydisperse sample of non-spherical particles, the particle size distribution is broader than the real distribution and biased toward larger particles. In addition, in sedimentation method, all particles need to have uniform and known density as particles of different sizes may settle at the same velocity because of density variations.

1.1.3 Coulter counter

The Coulter counter is one of the oldest particle analysis tool that is still widely used for off-line particle measurement. The method is commonly applied for counting blood cells [43, 44], bacterial cells [45, 46], determining cell volume distribution [47, 48], measuring particle size distribution (PSD) in crystallization [49,50] and so on. A simplified schematic of the Coulter counter is shown Fig. 1.2. It consists a long tube with an orifice

of known diameter at the bottom. The tube filled with electrolyte solution where the particles to be characterized are homogeneously suspended. The orifice of the tube is placed within a electrical sensing zone where conduction of current is facilitated by the electrolyte. When a particle passes through the orifice, a voltage pulse generated due to the electrical impedance is recorded by an oscilloscope. While the amplitude of the voltage pulse is directly proportional to the volume of the particle, the number of pulses determines the particle count [51, 52].

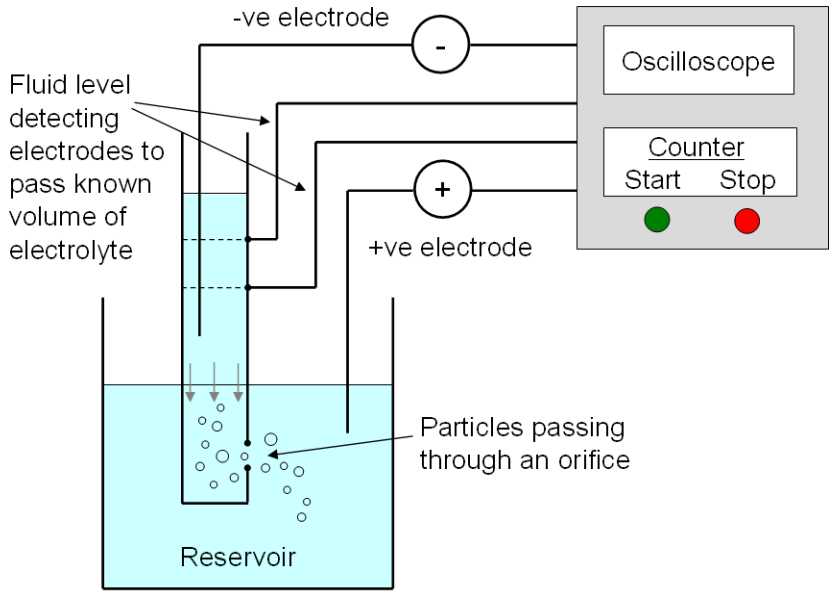

Figure 1.2: Principle of Coulter counter method.

While the Coulter counter provides rather accurate measurements of dilute concentrations of spherical particle, its performance deteriorates as the shape of the particles deviate from a perfect sphere [51]. Other limitations of these technique include the requirement of electrolytes and the clogging of the tiny orifice by the particles resulting in the difficulties of smooth measurement [16, 50].

1.1.4 Ultrasonic extinction

Ultrasonic Extinction is a popular and widely used on-line particle size analysis tool for concentrated disperse system. The use of this tool can be found in literature for the study of particle sedimentation [29, 53, 54], for the measurement of particle size during crystallization [55–59], monitoring particles' size and concentration in dense suspension and emulsions [60, 61], monitoring polymerization reaction [18, 62–64] and so on. This technique works based on the measurement of the attenuation of sound waves as a function of their frequency, typically from 1 to 200 MHz. In Fig 1.3, the schematic of ultrasonic extinction principle is shown. When sound waves of various frequencies are transmitted by an ultrasonic transducer (generator) through the concentrated suspension, presence of particles will create a discontinuity to the propagation of sound. As a result, attenuation of the sound wave is experienced which is received by another ultrasonic transducer (detector) as shown in Fig 1.3. The attenuation of the sound wave is calculated from the ratio of the signal amplitudes on the generator and the detector side. When particles are much smaller than the wavelength of sound, the attenuation is mainly the result of entrainment. When particles are much larger than the wavelength of sound the attenuation is resulted scattering. Thus the measured attenuation spectrum represents a signature for the particular suspension. If the physical properties of the system, such as material density, liquid viscosity etc., are known this attenuation spectrum pattern can be converted by a mathematical algorithm into a particle size distribution and concentration [37]. This technique can be used to measure particle size from 0.01-1000 μm over a wide concentration range (0.5 to 50% by volume).

However, retrieving the PSD from the attenuation spectrum relies on the assumption of spherical shaped particles and requires prior knowledge of mechanical, transport and thermodynamic properties of both particles and liquid medium. Hence, this method might not yield reliable results for the particulate systems where particles of different shapes are

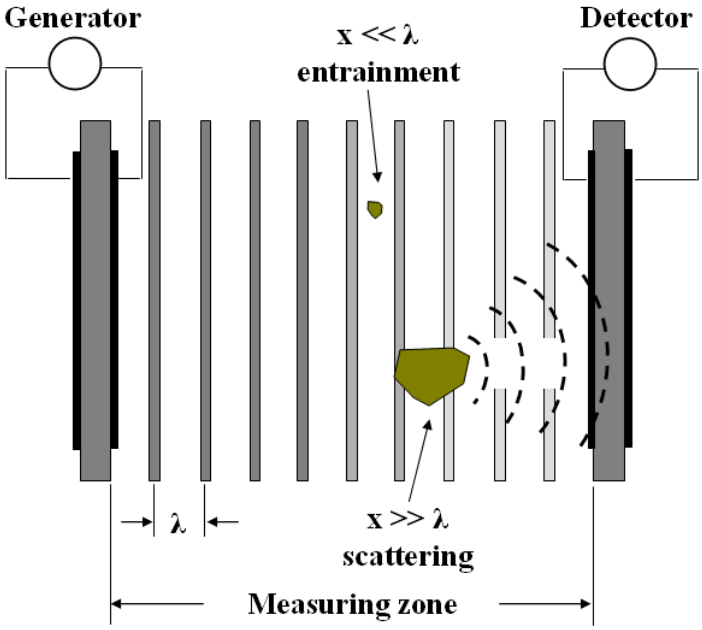

Figure 1.3: Ultrasonic extinction. 'x' refers to particle size and 'λ' is the wavelength of ultrasound wave.

present and the physical properties of the system is unknown.

1.1.5 Laser diffraction

Over the past two decades, laser diffraction has become popular and is the most widely used tool for industrial particle analysis. This instrument measures the particle size through the intensity of the scattered light by the particle as a function of scattering angle and wavelength of the light [38, 65]. The basic principle of laser diffraction method is shown in Fig. 1.4. A laser light through a set of optics creating a plane wave, is transmitted through a thin cell containing the particle suspension. Particles in the light path, scatter light at different angles based on their size and shape. The scattered and un-scattered light are passed through a Fourier transform lens and focused on a detector. The multi element detector records the information of the scattering light intensity which is a function of scattering angle, particle size, shape, wavelength of the

light and refractive index ratio of particle and medium. It should be noted that that the large particles scatter light at low angle, while small particle creates large angle scattering. The particle size distribution is then obtained from the recorded information theoretically via a deconvolution approach [38].

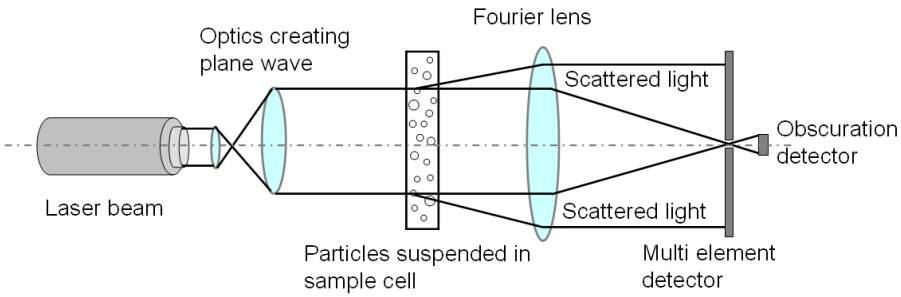

Figure 1.4: Principle of particle analysis by laser diffraction.

Although a useful technique, the inference of particle size from the scattering theory relies on the assumption of spherical shape of the particles, as the interpretation of scattering pattern of irregular or even regularly shaped non-spherical particles is complex and not easy to obtain. Thus the technique provides reliable information only for spherical particles.

1.1.6 Focused beam reflectance measurement

Focused beam reflectance measurement (FBRM) is the most commonly used in-situ measurement technique for real time particle measurement. In literature, a variety of applications of FBRM probe are reported, such as, monitoring and control of crystallization process [65], study of polymorphic transformation [66–68], determination of solubility curves and metastable limit in crystallization processes [69, 70], flocculation process design [71], characterization of plant cell cultures [72] and in-situ monitoring of cell growth [73, 74] in biological applications. This sensor works based on the principle of laser backscattering as illustrated in Fig. 1.5. This probe based tool can be directly inserted

into a reaction vessel and hence, unlike other on-line particle sizing tools, no installation of pre-dilution side-stream is required [75, 76]. The FBRM probe uses a highly focused laser beam rotating with a high speed that rapidly scans over a small region of particles suspension. When a particle comes in the field of the rotating beam, the beam hits the particle and results in backscattered light which is back propagated through the probe window and recorded by a detector. Backscattering continues until the rotating beam completes scanning from one edge to another edge of particle. The time span of scanning is multiplied by the scan speed of the rotating beam to give the distance between two edges of the particle, *i.e.,* chord length [38, 65, 77]. Besides serving as an in-situ measurement tool, the FBRM offers some other advantages. It can be used at high suspension densities. Further, thousands of chords with the size range of $0.8 - 1000\ \mu\mathrm{m}$ can be measured very rapidly yielding robust chord length distribution (CLD) [70, 78]. It is worth noting

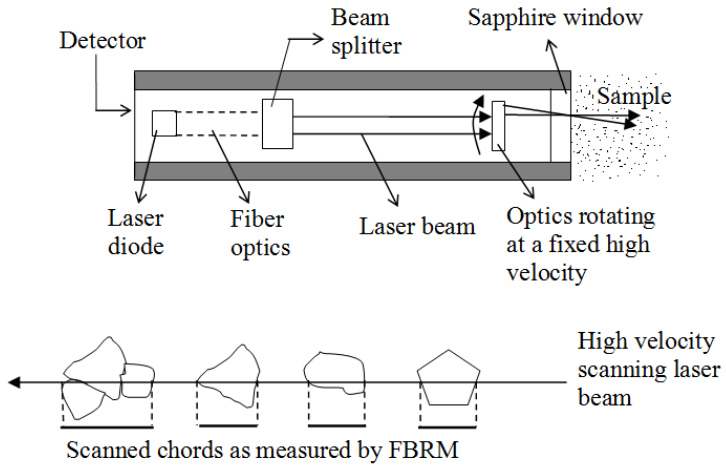

Figure 1.5: Principle of FBRM probe.

that in practical applications, CLD does not provide unambiguous information about the particle size. For practical purpose, the CLD needs to be converted to PSD. For this purpose, both theoretical and empirical models are established in literature [70, 77, 79–81].

However, better performance of the theoretical models relies only upon the assumption of the particle shape [77, 80]. Hence, applying such models on sample of unknown or random particle shape creates difficulties [77]. In addition, empirical approaches were also often used to correlate the measured CLD with known PSD measured by other particle sizing techniques, such as laser diffraction [82], imaging sensor [83], sieving [84] etc. Heath et al. [82] studied calcite and aluminum particles to compare the FBRM data with laser diffraction method. The median average values obtained from laser diffraction are compared with chord lengths data from FBRM applying different weighting factors. The square-weighted chord length showed the best correlation with the particle size measured by laser diffraction. Ruf et al. [77] developed a 3D geometrical model of CLD of a particle of general shape, that enables the transformation of PSD into CLD. They investigated the correlation between FBRM data and laser diffraction from the experimental study of ceramic beads and glass beads. For the ceramic beads, FBRM yielded broader CLD shifted towards the shorter lengths compared to the result of laser diffraction. Further, for the glass beads, two techniques yielded significant differences in measurement which were attributed to insufficient contrast between glass beads and aqueous medium.

In literature various factors that affect FBRM measurement are reported. For instance, the detection of the reflected signals by the particles through FBRM is sensitive to particle opacity, *i.e.*, identical sized particles with different opacity can result in different reflection signals, thus leading to erroneous chord lengths measurement [78]. The impact of the FBRM probe's position and orientation in a vessel on the chord length distribution is also reported in literature [70, 77, 83] . The measured CLD by FBRM is found to be sensitive to the location and orientation of the FBRM probe with respect to the flow of dispersion.

1.1.7 Direct imaging techniques

Imaging techniques, such as Particle vision microscope (PVM) probe and video microscopy, are established techniques for characterization of particle size and shape. Video microscopy can be employed on-line whereas PVM can be employed in-situ. Video microscopy is placed outside the system focusing on the particle suspension inside the processing unit through an imaging window. Illumination of the particle suspension is provided by a strobe light directed towards the imaging window [85–88]. The PVM probe uses a charged couple device (CCD) camera with light sources fitted into the probe. Thus, this probe can be placed inside the particle suspension directly [69]. Acquired images from these techniques undergo image analysis to obtain quantitative information of size and shape of particles [89, 90]. Image analysis thus offers direct information about particle size and shape, which is not possible from other techniques.

For the last few years online high speed imaging has shown to be a promising tool for real time particle size and shape measurement. Several research groups have been exploring the efficient use of imaging tool for monitoring and controlling crystallization process [26–28, 87], for the detection polymerization bubbles in emulsion polymerization [91], for the study of precipitation process [92], for atmospheric haze detection [93], etc. The imaging techniques reported in these studies are based on two-dimensional (2D) imaging of three-dimensional (3D) real scene. Different approaches have been suggested to extract size and shape information from the projections. Although direct imagine is a powerful tool compared to traditional one, it has a few important shortcomings. Firstly, the segmentation of 2D image for extracting particle size and shape can be challenging due to the limited depth of focus (DOF) of the camera imposed by the required magnification. Images containing particles on the focal plane provide sharp contrast, while particles that are out of the focal plane are blurred [4, 86, 87]. As a result, image analysis often falsely identified out-of-focus particles together with the focused particles and measure their sizes assuming

constant magnification throughout the image depth. This assumption results in inaccurate measurement of particle size. Secondly, 2D imaging systems provide projections of the particles showing their orientation only on the 2D image plane. Hence the retrieval of the real size of particles from the projections requires knowledge of particle orientation out of the 2D image plane [88, 90, 94]. In practical situations such information is seldom known. Recently efforts have also been made for the restoration of the 3D information of particles from 2D images using model based measurement methods [79, 95]. However, these methods require assumption of perfect particle geometry and random orientation of particles in 3D, thereby making these methods highly idealized. Hence, application of such a method to particulate suspensions encountered in practice requires proper tuning. Apart from these, attempts have also been made to reconstruct the 3D shape of the particle directly from the stereo-vision system using two or more synchronized camera heads [88, 94]. However, this stereoscopic concept of imaging imposes some complications as the cameras used in the setup must be focused on the same spot of particle flow or dispersion and must be properly calibrated to obtain the same point in focus. In addition, the technique is only capable to measure single particle at a time in the measuring volume [94]. It is worth pointing out that in addition to direct imaging techniques, another technique, namely Raman spectroscopy, is also used to identify crystals' structure. The pros and cons of this technique have been discussed in the next section.

1.1.8 Raman Spectroscopy

Raman Spectroscopy is one of the most prominent techniques for in-situ and quantitative identification of solid-state forms in slurries [66, 67, 96]. This technique works on the principle of inelastic scattering of monochromatic light. In inelastic scattering, frequency of the photons changes subsequent to the interaction with a sample. Raman spectroscopy records the amount of scattered light at different wavelengths by a sample when the sample

is exposed to a field of monochromatic laser beam. The wavelength of the scattered light, which are different from the incident light, arise from the interaction between incident photons and different atomic or molecular bonds present in the sample. Hence each difference in wavelength between incident and scattered light represents a fingerprint for a particular chemical bond and provides information about vibrational, rotational and other low frequency transitions in molecules [97]. Thus Raman spectroscopy is well suited for in-situ quantitative measurements of polymorphic composition in solution crystallization [67]. Raman spectroscopy has the following advantages: it can be used for monitoring solid and liquid phases simultaneously; it does not require sample preparation and it can be useful for remote sensing as well [67].

This technique does not provide information of particle size measurement. Calibration of Raman spectra for quantitative measurements of polymorphic composition is also required and difficult as Raman signals from different components present in the system are affected by the particle size distribution [66]. Hence, reliable quantitative measurements by Raman spectroscopy depends on corrections for particle size effects [66].

1.2 Scope and objectives of the thesis

Digital holography is a novel tool that helps overcome some of the limitations of classical imaging techniques. Digital holography records the interference pattern between two coherent light beams, while conventional imaging techniques record only the intensity distribution of the incident light. The interference pattern recorded contains information about the entire volume of the sample which can be numerically reconstructed for focusing at different planes of the volume [98]. The application of digital holography can be found in literature for the study of micro-electro-mechanical systems (MEMS) [99, 100], biological applications [101] and particle image velocimetry [102, 103].

The role of holography in the field of particle analysis has been known for some time

but very limited attempts have been made for on-line particle analysis [104–111]. Some of these studies are based on direct fringe analysis of the hologram without reconstruction. These approaches assume spherical shape of the particles for estimating the size and location of the particles [106, 108]. Hence their application to non-spherical particles is limited. Most of other studies dealing with particle size measurement from the numerical reconstructions of the hologram considered particles with spherical shape only. Further, most studies in literature deal with measurement of single particle and do not adequately address the characteristics (size and shape distribution) of particle population which is of high practical importance [105, 107, 110]. More importantly, no efficient and automated image analysis are performed for the segmentation of particles in conjunction with numerical reconstructions of the hologram. Hence these methods cannot be applied for on-line particle measurement.

A few studies are found that deal with the measurement and localization of non-spherical particles, such as, measurement of microfibers [112–114]. However these methods are limited to the measurement of the fibers in the plane of the camera, or require *a priori* knowledge about the orientation of the fibers in 3D or size of the object to estimate the real lengths. Hence, these studies are not adequate for several practical situations, *e.g.*, measuring true sizes and shapes of fiber population oriented randomly in a solution. It is clear from the above discussion that though digital holography has the potential to measure particles, on-line characterization of particles' size and shape using digital holography still remains a major challenge. Hence, we envisage that the unique 3D imaging capability of digital holography could be used efficiently for the measurement of particle size and shape in a volume. This could potentially result in a novel tool for on-line monitoring of particulate processes in various chemical industries.

The objective of this work is to develop digital holography based sensor for on-line measurement of particle size and shape. We limit ourselves to particle sizes in the range of

10 to 1000μm, a range of practical interest. To achieve this goal, the thesis aims to address the unexplored issues associated with on-line size and shape measurement of particles for particulate process. The specific aims of this work are:

- To investigate the capability and methodology of lensless digital holographic microscopy (LDHM) for imaging and measurement of microparticles in solution.
- To develop automated image analysis routine in combination with digital holographic imaging requirements for on-line size and shape measurements.
- To benchmark the use of digital holographic measurement method using opaque microparticles with wide ranges of sizes and shapes.
- To investigate the performance of digital holographic measurement technique for the measurement of particles in static, flowing, wet and dry conditions.
- To develop 3D image analysis for randomly oriented particles in volume for simultaneous measurement of size, location and angle of orientation and to benchmark the method in comparison with independent measurement techniques.
- To implement the digital holographic measurement method for the measurement of crystals in solution.

1.3 Thesis structure

The thesis is organized as follows:

The principle, recording and reconstruction procedure of digital holography are discussed in detail in Chapter 2.

In Chapter 3, an algorithm is developed for automatic measurement of the size and shape of microparticles from the recorded hologram. The method is then benchmarked using

microparticles with wide variety of sizes and shapes. The performance of the method for static and suspended particles is also analyzed.

In Chapter 4 a novel algorithm is developed for simultaneous measurement of size, position and orientation of needle shaped particles in solution. The method is validated by the measurement of single fiber of known length. The applicability of the method in solution is also demonstrated using microfibers suspended in water.

Some limitations involved in the measurement method developed in Chapter 4 are overcome in Chapter 5. This chapter introduces an improved algorithm for the simultaneous measurement of size, position and orientation of needle like particles. The performance of the new method is compared with the methods developed in previous chapters. Finally, the method is applied for the measurement of population of microfibers in solution.

In Chapter 6, the algorithm developed in Chapter 5 is used to measure the size and shape of transparent crystals in solution. The method is also used to monitor the growth of crystal size distribution of oxalic acid during crystallization.

Finally, Chapter 7 discusses the conclusions of this work and provides directions for future research.

Chapter 2

Holography and holograms

2.1 Principle

Holography in contrast to photography is a method to record three-dimensional (3D) information of objects. The wavefront scattered by any illuminated object contains both amplitude and phase information. Conventional recording materials, however, only respond to the intensity. To obtain the full 3D information, it is also important to record the phase information. Hence, the recording medium requires phase to be converted into variations of intensity. Holography does this by introducing a coherent light source to illuminate the object. In this technique, the interference pattern between two coherent light beams, one is from direct illumination and other is from scattered wave by the object, is recorded as hologram. In the case of illumination with a spherical wavefront it consists of concentric fringes centered on the optical axis as shown in Fig. 2.1. The intensity at each point of this pattern now also depends on the phase of the object wave and thus the hologram contains information of both its phase and amplitude.

To explain this technique, a typical optical set-up for traditional free-space in-line digital holography, shown in Fig. 2.2(a), is used. In this configuration, a strongly coherent light source (laser) illuminates an object. A part of the light is diffracted by the object creating

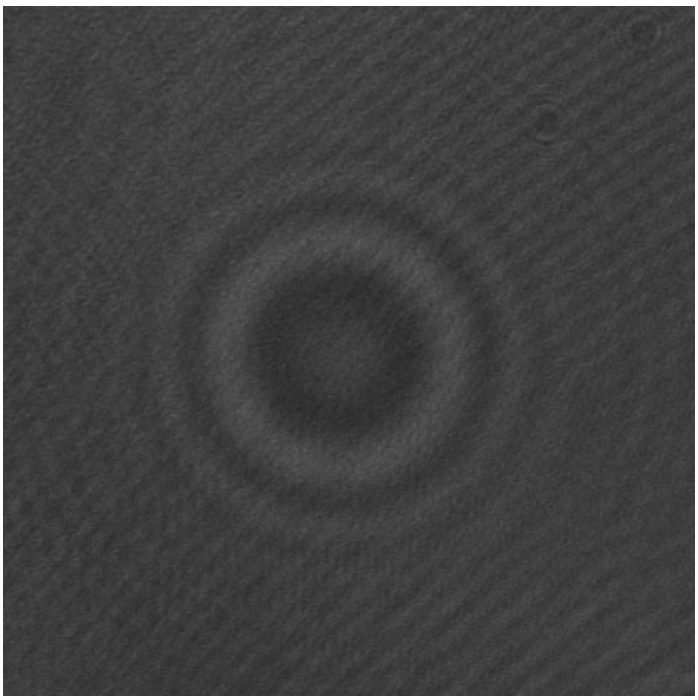

Figure 2.1: Concentric interference fringes.

the 'object beam', while another part, called 'reference beam' remains un-diffracted. The object can be considered to be made up of a large number of point sources distributed in a three dimensional space. Each point of the object will interfere with the reference and produce fringes which is recorded by a light sensitive medium, *e.g.*, photographic film [98]. The recorded interference pattern is called a hologram. When the hologram recorded by the photographic film (after subsequent chemical film development) is illuminated with the light of same wavelength as before, in the absence of the object, two diffracted waves are obtained. One reconstructing a virtual, undistorted image in the object's former position and another one with the same amplitude but the opposite phase, producing a real image as shown in Fig. 2.2(b). The object field of view corresponds to the virtual image field of view, so the virtual image corresponds to the true image while the real image is often called conjugated or twin image. By use of this method a complete three-dimensional image of the object can be produced which exhibits all effects of perspective and depth of focus. Unlike conventional microscopy, holography does not use any focusing optics. Hence, in

comparison with other 2D imaging techniques, holography offers a unique characteristic of restoring 3D volume information from a single hologram acquisition [98].

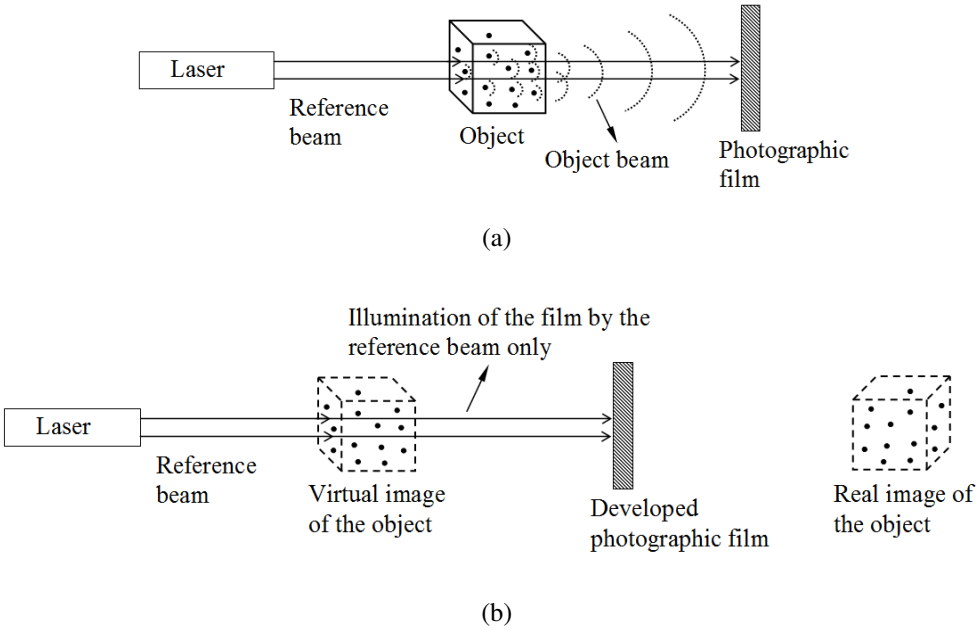

Figure 2.2: Principle of holography: (a) A typical set-up for recording of a hologram; solid lines correspond to reference beam and dotted curves correspond to object beam. (b) Reconstruction of the hologram.

Although the use of high definition photographic films for the recording of particle holograms allows the study of samples with with high-resolution, but it suffers from increased processing time required for film development and subsequent digitization of the reconstructions. With digital recording of holograms using a charged couple device (CCD), the chemical processing step for the film development is eliminated. Hence, it provides the possibility to perform software based numerical reconstruction, which substantially increases the practicability of the method for on-line application. The resolution achievable by digital holographic systems might not be as high as the one obtained with holograms recorded on high-resolution films, but the ease of processing has made digital holography more attractive for particle analysis.

2.2 Digital in-line holography

In digital holography, the hologram constituting of the interference between plane reference wave and the waves scattered by the object, is directly recorded and stored as a digital image using a CCD. Subsequent reconstruction is carried out numerically. Unlike the most commonly used off-axis approach, the in-line approach of holography uses a single beam to illuminate the object, hence the diffracted light by the object cross-section acts as the object beam and the directly transmitted light acts as the reference beam. Thus the interference of the object and reference waves that propagate along the optical axis constitutes the in-line hologram. In comparison to the off-axis setup, in-line geometry helps to relax the spatial resolution requirement on CCD sensor and provides larger field of view with higher imaging resolution [115].

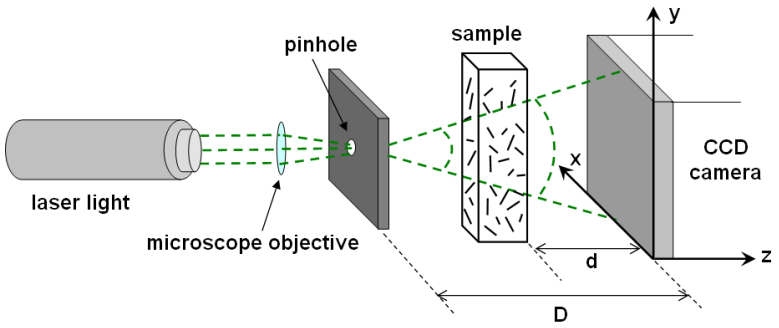

Figure 2.3: Schematic of digital in-line holographic recording set-up.

The setup for the recording of the digital in-line holograms is shown in Fig. 2.3. A laser beam is focused by a microscopic objective lens onto a pinhole, which is located at a distance D from the recording camera. The resulting spherical diverging beam originating from the pinhole illuminates the object, a diffusely reflecting body which is located at a distance d from the recording camera. One part of the illuminating beam passes through the object without being diffracted and acts as the reference beam, U_R. Another part of the illuminating beam is diffracted by the object, generating the object beam, U_o, which

propagates towards the recording camera. The resulting interference between the reference and the object waves constitutes of the hologram on the CCD surface. It is noted that the diffraction pattern produced on the CCD surface is geometrically magnified, when the object and reference beam interfere along the optical axis, as can be seen from Fig. 2.3. Hence, the set-up shown in Fig. 2.3 is referred as lensless in-line digital holographic microscopy (LDHM) [98, 105, 116].

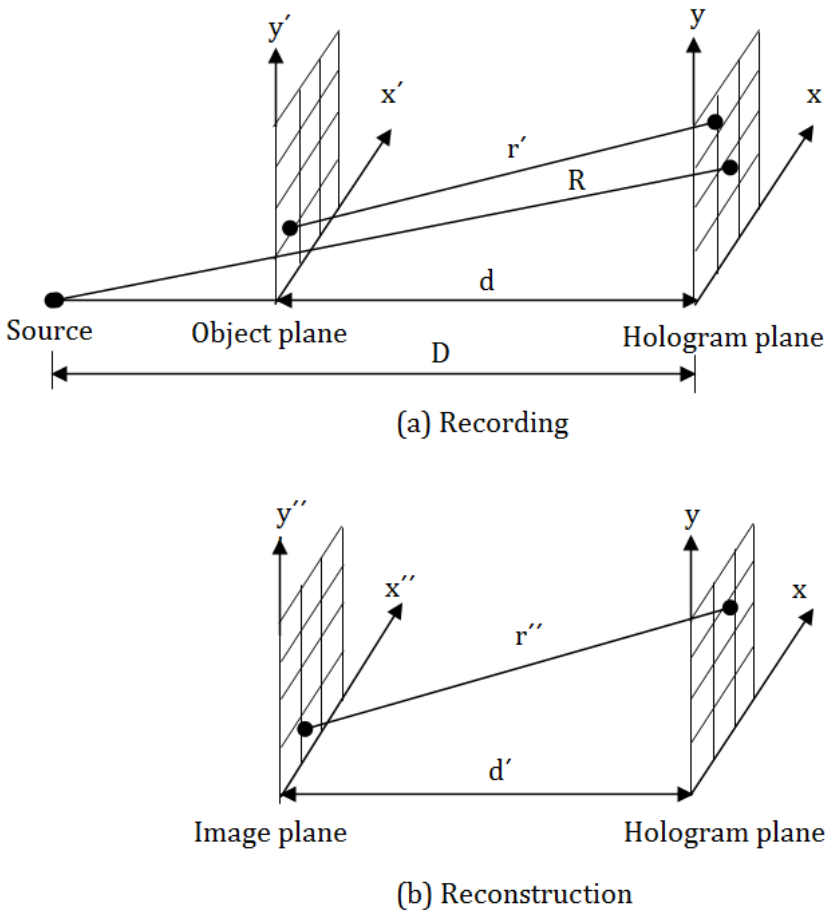

Figure 2.4: Geometry of digital in-line holography: (a) Recording and (b) reconstruction.

The geometry of digital in-line holography is shown Fig. 2.4. The pinhole functions as a point source and emits by approximation a spherical diverging reference beam U_R at the

hologram plane which can be expressed as [98]

$$U_R(x,y) = \frac{\exp\left(-i\frac{2\pi}{\lambda}\sqrt{D^2+x^2+y^2}\right)}{\sqrt{D^2+x^2+y^2}}, \tag{2.1}$$

where x and y are the spatial coordinates on the camera plane, λ is the wavelength of the laser beam and $i = \sqrt{-1}$. The term $\sqrt{D^2+x^2+y^2}$ (distance R in Fig. 2.4) describes the distance between point source and a point on the camera plane.

The object beam U_o at the camera plane can be expressed by the Fresnel-Kirchhoff integral as [98]

$$U_o(x,y) = \int_{-\infty}^{+\infty}\int_{-\infty}^{+\infty} U_o(x',y')\frac{\exp\left[-i\frac{2\pi}{\lambda}\sqrt{(x'-x)^2+(y'-y)^2+d^2}\right]}{\sqrt{(x'-x)^2+(y'-y)^2+d^2}} cos\Theta dx'\,dy', \tag{2.2}$$

where x', y' are the spatial coordinates on the object plane. The term $\sqrt{(x'-x)^2+(y'-y)^2+d^2}$ (distance r' in Fig. 2.4) describes the distance between a point on the object plane and a point on the camera plane. $cos\Theta$ is the inclination factor which normally can be set $cos\Theta = 1$ due to the small angles between the hologram normal and the rays from the hologram to the image points.

Unlike in the conventional imaging plane, wavefront emanating from each point of the object reaches every point of the CCD and thus every portion of the hologram obtains complete information on the amplitude and phase distributions of the object field in the form of the interference pattern. The resulting intensity of the hologram captured by a CCD camera can be expressed as

$$\begin{aligned} I(x,y) &= |U_R(x,y) + U_o(x,y)|^2 \\ &= |U_R(x,y)|^2 + [U_R^*(x,y)U_o(x,y) + U_R(x,y)U_o^*(x,y)] + |U_o(x,y)|^2 \end{aligned} \tag{2.3}$$

The right hand side of Eq. 2.3 consists of four terms. The first term $|U_R(x,y)|^2$ refers

the directly transmitted beam. The second two terms, *i.e.* the sum in square brackets, are hologram terms as they consist of superposition of reference and object wave. Asterisk ,'*', indicates the complex conjugate of the corresponding term. The fourth term, $|U_o(x,y)|^2$, is referred to as the self interference term, containing the interference between the scattered waves. Typically this term is very small compared to the other three and thus becomes negligible.

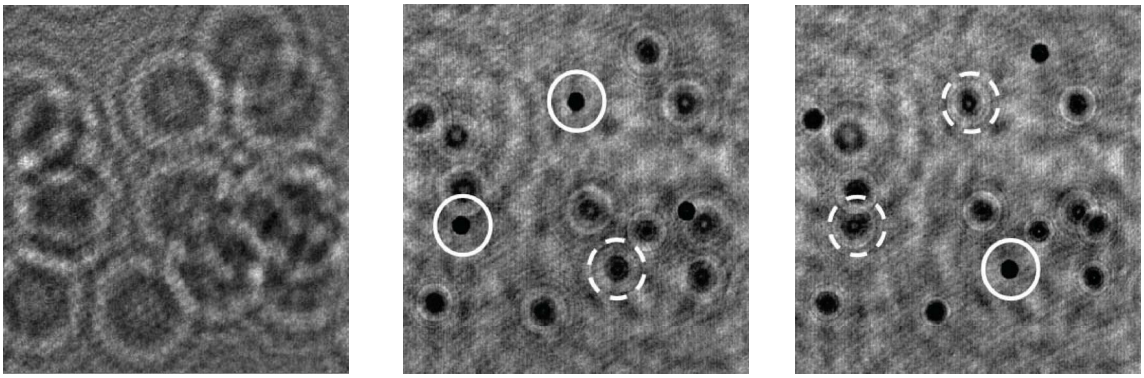

(a) (b) (c)

Figure 2.5: Digital holographic microscopy of polymer spheres suspended in water (a) Hologram; (b) a sample reconstruction at distance d_1; (c) reconstruction at a different distance d_2. Solid circles indicate particles focused at the chosen reconstruction depth.

Figure 2.5(a) shows an example of a digital hologram of a population of polymer spheres suspended in water. For the reconstruction of the hologram at a distance d', *i.e.* at the image plane (x'', y''), $I(x,y)$ has to be multiplied by the reference wave and then propagated using the Fresnel-Kirchhoff integral as [98, 105]:

$$U_o(x'',y'') = \int_{-\infty}^{+\infty}\int_{-\infty}^{+\infty} I(x,y)U_R(x,y)\frac{\exp\left[-i\frac{2\pi}{\lambda}\sqrt{(x-x'')^2+(y-y'')^2+d'^2}\right]}{\sqrt{(x-x'')^2+(y-y'')^2+d'^2}}dx\,dy, \tag{2.4}$$

where x'', y'' are the spatial coordinates in the image plane. The term $\sqrt{(x-x'')^2+(y-y'')^2+d'^2}$ (distance r'' in Fig. 2.4) describes the distance between a point on the image plane and a point on the camera plane. For $d' = d$ and when quantization

and other digitizing errors are negligible, the reconstructed wave $U_o(x'', y'')$ equals to the object wave $U_o(x', y')$.

Eq. 2.4 can be interpreted as superposition integral [98, 117]:

$$U_o(x'', y'') = \int_{-\infty}^{+\infty} \int_{-\infty}^{+\infty} I(x, y) U_R(x, y) g(x'', y'', x, y) dx\, dy, \tag{2.5}$$

where the impulse response $g(x'', y'', x, y)$ is given by

$$g(x'', y'', x, y) = \frac{\exp\left[-i\frac{2\pi}{\lambda}\sqrt{(x - x'')^2 + (y - y'')^2 + d'^2}\right]}{\sqrt{(x - x'')^2 + (y - y'')^2 + d'^2}} \tag{2.6}$$

According to Eq. 2.5 the linear system characterized by $g(x'', y'', x, y) = g(x''-x, y''-y)$ is space invariant. The superposition integral can be regarded therefore as a convolution [98]. Hence, the diffraction integral in Eq. 2.4 can be numerically solved by the convolution approach [98, 117, 118]. The convolution theorem states that the Fourier transform of the convolution of $I.U_R$ with g, is the product of the individual transforms $F\{I.U_R\}$ and $F\{g\}$. Hence, $U_o(x'', y'')$ can be calculated by first Fourier transforming $I.U_R$, then multiplying with the Fourier transform of g, and taking the inverse Fourier transform of this product. Total three Fourier transforms are necessary for the whole process which can be carried out using efficient FFT-algorithm. In short notation, the reconstruction of the hologram at the image plane is:

$$U_o(x'', y'') = F^{-1}\{F(I.U_R).F(g)\} \tag{2.7}$$

The diffraction integral can also be solved by another approach, namely, Fresnel-approximation. In the Fresnel approximation method, the resulting image size changes depending on the wavelength and distance of the object from the CCD, while in the convolution approach the size of the resulting image does not change with these

parameters [98, 117]. In our study we solved Eq. 2.4 to obtain the reconstruction of the scene at a desired distance by convolution approach, where the pixel size of the reconstructed image ($\Delta x''$, $\Delta y''$) equals the pixel size of the recording camera (Δx, Δy), *i.e.* $\Delta x'' = \Delta x$ and $\Delta y'' = \Delta y$ [98, 105]. Figures 2.5(b) and 2.5(c) show sample reconstructions, at two different depths, obtained from the hologram shown in Fig. 2.5(a). As can be seen, objects at different positions along the z axis (optical axis) come into focus as d changes. It is worth emphasizing that the two reconstructions are obtained from the same hologram and hence it is possible to overcome the focusing issue that is encountered in classical imaging techniques. This is an unique advantage of holography. It is worth noting that the diverging beam used in the set-up introduces magnification allowing the study of smaller particles. This magnification is a function of the reconstruction distance. Hence, lateral magnification is defined as $M(d) = O'(d)/O$, where $O'(d)$ is the measured size of the object at distance d and O is the original object size. This magnification can be introduced by changing the distance between the point source of the spherical reference wave and the CCD, or the wavelength that is used for the reconstruction as [98]

$$M(d) = \left(1 + \frac{d}{D'}\frac{\lambda}{\lambda'} - \frac{d}{D}\right)^{-1}, \tag{2.8}$$

where D' is the pinhole to CCD distance and λ' is the wavelength which is used for the reconstruction. By changing D' and λ', the distance d', where the object will appear focused, also changes as [98]

$$d' = \left(\frac{1}{D'} + \frac{\lambda'}{\lambda}\frac{1}{d} - \frac{1}{D}\frac{\lambda'}{\lambda}\right)^{-1}. \tag{2.9}$$

The LDHM setup which has been described above has some distinct advantages. Firstly, it offers the possibility to focus an object at different focusing depth by numerical reconstruction from a single recording. The use of convolution based reconstruction

method simplifies the spatial localization of the particles as it overcomes the pixel resizing problem which causes shifting of the x-y location of the particles for different depth of the reconstructed images. Secondly, the lensless diverging setup offers magnification of the object as a function of image depth without any microscope objective (MO) lens. Thus, it allows the study of smaller particles within a full 3D volume. As the setup does not use any MO lens for magnification, the setup is free from lens aberration. Thirdly, it minimizes the effects of the twin image since the twin image is well out of focus for the depths where the particles appear focused [107, 119].

Chapter 3

Two-dimensional measurement of microparticles

3.1 Introduction

Digital holography is an effective three-dimensional imaging technique, with the potential to be used for particle size measurements. A digital hologram can provide reconstructions of volume sample focused at different depths, overcoming the focusing problems encountered by other imaging based techniques. Several particle analysis methods discussed in the literature consider spherical particles only [107, 118, 119]. With the object sphericity assumption in place, analysis of the holographic data can be significantly simplified. However, there are applications, such as particle analysis and crystallization monitoring, where non-spherical particles are often encountered. This chapter focuses on benchmarking digital holographic microscopy for measurement of particle size distribution of a population of microparticles for both spherical and arbitrarily shaped particles. For this purpose an automated algorithm called '2D projection algorithm' for identification of particles from recorded hologram and subsequent size and shape measurement is proposed. Experimental results using holograms of spherical and non-spherical particles demonstrate

the performance of the proposed measuring algorithm. Part of this chapter has been published elsewhere [120–122].

3.2 Methodology for 2D measurement of micro-particles

There are several algorithms available for extraction of particle properties, such as size and location, from the hologram without reconstruction [106, 108, 123]. These algorithms, however, assume that the particles are spherical and hence cannot be used for accurate size and shape measurement of non-spherical particles. In this section, we propose a method for obtaining the particle information from reconstructions of recorded hologram at several depths. For easier illustration, the overall algorithm is pictorially represented in Fig. 3.1. Details of the proposed algorithm for processing the hologram and subsequent image analysis for particle characterization are discussed in the following sections.

3.2.1 Numerical reconstruction and background correction

In order to study a volume of the sample, first each hologram needs to be reconstructed at several reconstruction depths. Reconstructions are carried out using the method described in Section 2.2 covering the volume to be studied with sufficiently small depth steps. The distance between successive reconstructions depends on the minimum size of the particles to be studied. Hence, several particles will appear at each reconstructed image as either focused or out of focused particles. A sample hologram and reconstructed image is shown in Fig. 3.2(a) and 3.2(b), respectively. As shown in Fig. 3.2(a), the background of the reconstructed hologram is not uniform. The bright background is due to the zero order of the reconstruction, which is also contaminated by noise caused by speckle due to the coherent illumination, the twin image and non-uniform illumination. One approach to reduce the zero order term from the reconstruction is to high-pass the

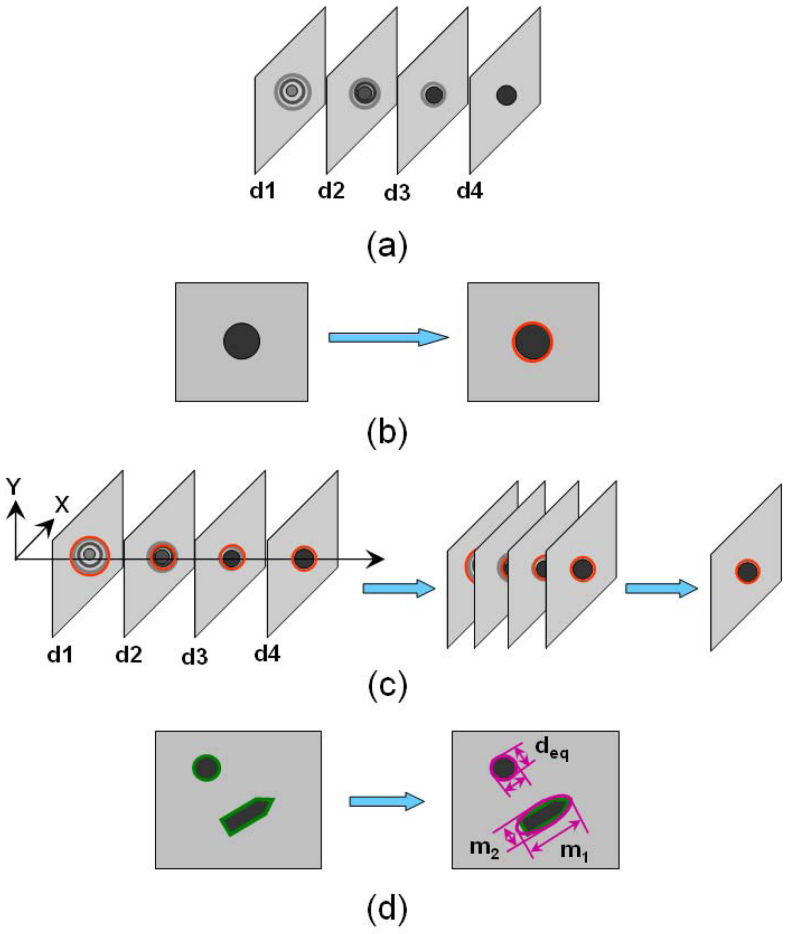

Figure 3.1: Steps for hologram processing algorithm: (a) Numerical reconstruction at several depths; (b) image segmentation using Canny edge detection; (c) localization of a particle; and (d) particle size and shape measurement, d_{eq} denotes the equivalent diameter for spherical objects, while m_1 and m_2 represent the major and minor axes for non-spherical particles.

hologram with a low-cutoff frequency filter before reconstruction [98]. Another approach is to record the reference wave (without the object) and subtract it from the hologram prior to reconstruction [107]. The latter approach, however, is impractical for real time monitoring as the sample needs to be removed from the system regularly in order to record the updated images of the reference wave. In all cases, we have noticed that the suppression of the zero order term affects the particles by either blurring or changing their perimeter leading to erroneous size measurements. In the following section, we propose an edge detection-based technique for particle segmentation which is immune to the presence of zero order term and other irregularities of the background, thus eliminating the need for preprocessing the hologram.

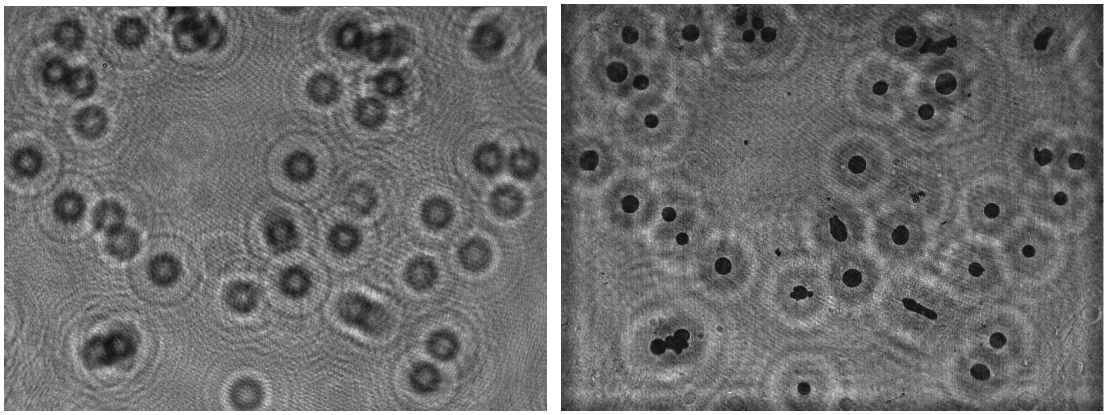

(a) (b)

Figure 3.2: Example of digital hologram and reconstructed image of ceramic beads on glass slide: (a) One of the recorded digital holograms, (b) Example of a reconstructed image.

3.2.2 Image segmentation

A possible approach for image segmentation involves thresholding the intensity of the reconstruction [124]. In threshold-based segmentation, pixels with intensity value lower than the threshold are considered to belong to a particle, while pixels with intensity values higher than the threshold are considered to be background [89, 125]. In general, the

selection of an appropriate threshold value can be difficult. An inappropriate choice for threshold value results in identification of noise, *e.g.*, impurities in the sample solution, shot noise from the laser, diffraction effects from multiple objects, etc., present in reconstructed holograms as particles or unidentified particles. Furthermore, imperfections such as non-uniform illumination of the hologram lowers the performance of threshold-based segmentation. Some additional details regarding the drawbacks of threshold-based segmentation are given elsewhere [122].

After numerical reconstructions, we use Canny edge detection at each reconstructed image for particle segmentation [126]. In this edge detection technique, a Gaussian filter with standard deviation, σ, is first applied to the reconstruction to reduce the effect of noise. Subsequently, the edges are detected by examining the gradients of intensity for local maxima. Here, thresholding with hysteresis is used to classify the identified maxima using two threshold values, t_L and t_H ($t_H > t_L$). Maxima with a value lower than t_L are identified as not being edges. Similarly, maxima with a value higher than t_L are identified as edges. Maxima with value between t_L and t_H are identified as edges only if they are connected to identified edges [89]. Apart from good localization, the use of edge detection-based particle segmentation on digital holograms also has the advantage that highly unfocused particles are not detected, as particles are usually surrounded by strong edges only close to their best focusing point.

For every reconstruction, the edge detection algorithm results in a binary matrix with ones corresponding to pixels where edges are detected and zeros elsewhere. To identify particles from this matrix, dark areas completely enclosed by edges are filled to form blobs, which are considered as possible particles. Open-ended lines are removed by erosion followed by dilation in order to eliminate noisy formations that frequently appear in the background. This, in principle, does not change the size of the identified blobs. To avoid identifying noise as particles, blobs with diameter less than a cut-off value are

removed. Further, blobs touching the edges of the reconstruction window are also removed, as these particles are partially located outside the reconstruction. Finally, a set of blobs corresponding to particles detected in the reconstruction under consideration is obtained.

The edge detection algorithm requires the selection of 3 parameters: the standard deviation of the filter, σ, and the two thresholds, t_L and t_H. A large σ value results in a Gaussian filter with large width, which may affect the size of small particles causing erroneous size measurements. Thus, σ is selected such that the filtering operation does not alter the size of the particles under investigation. On the other hand, the thresholds t_L and t_H only affect the number of identified particles and not their sizes. High values lead to identification of fewer particles (particles with very sharp edges), while lower values lead to false positives (areas surrounded by sharp edges). The false positives correspond to fringes caused by the twin image or out of focus particles and are much brighter than focused particles. As a result, they can be easily identified and neglected based on their average intensity. The performance of the algorithm is not very sensitive to the selection of these parameters. In this work, t_L and t_H are chosen as 0.3 and 0.6, respectively, and the same set of parameters have been used for the different experimental results presented in Section 3.3 and were found to give good results for holograms recorded under different conditions and containing particles of different size ranges.

3.2.3 Localization of particles

As the particle segmentation step is applied to every reconstruction of the hologram, a single particle may be identified in several reconstructions. Further, the magnification depends on the reconstruction distance. Thus, the best focusing depth needs to be determined for accurate size and shape measurement, *i.e.,* particle localization has to be performed.

To find the best focusing depth, blobs with overlapping spatial positions at different

reconstruction depths are given identical labels. Subsequently, the mean intensity and the variance of each reconstruction is calculated [127]. The reconstruction depth at which these parameters show a minimum is taken as the best focused depth. Normalized depth profiles of the mean intensity and the variance of the intensity for one particle are shown in Fig. 3.3, where best focusing depth is obtained 32.25 mm. Particles with minimum of the focusing metric occurring at the first or last examined depth, are likely to be located outside the examined depth range and hence are ignored to avoid erroneous measurements.

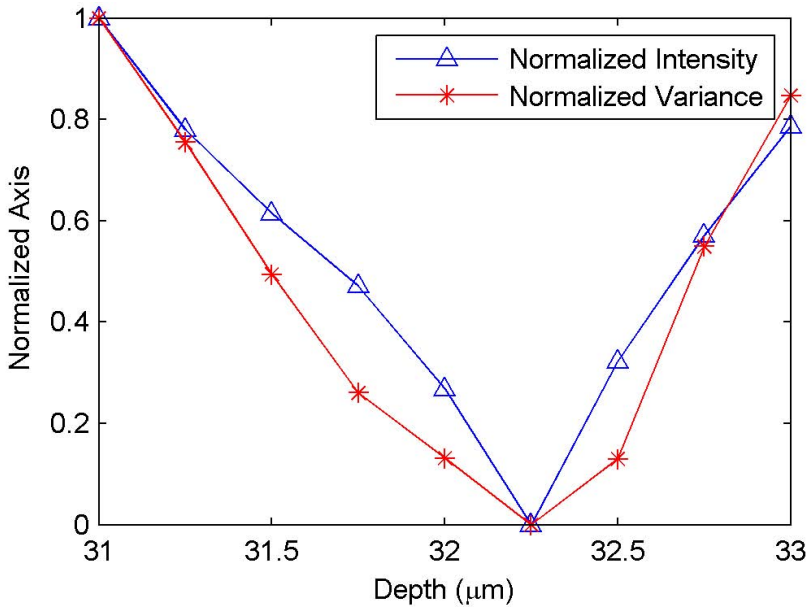

Figure 3.3: Depth profile of the normalized focusing metrics (mean intensity and variance of the intensity) for one particle. The best focusing depth for this particle is 32.25 mm.

3.2.4 Particle size and shape measurements

Particle segmentation and focusing provide the area occupied by each particle at its best focusing depth. In general, the particles are not spherical and thus the identified regions are not circular. As a result, it is not always easy to measure their sizes. However, several metrics are available for characterizing non-spherical particles. The most commonly used metrics are circle equivalent diameter, aspect ratio and solidity or convexity. These shape

factors, illustrated in Fig. 3.4, are briefly discussed next.

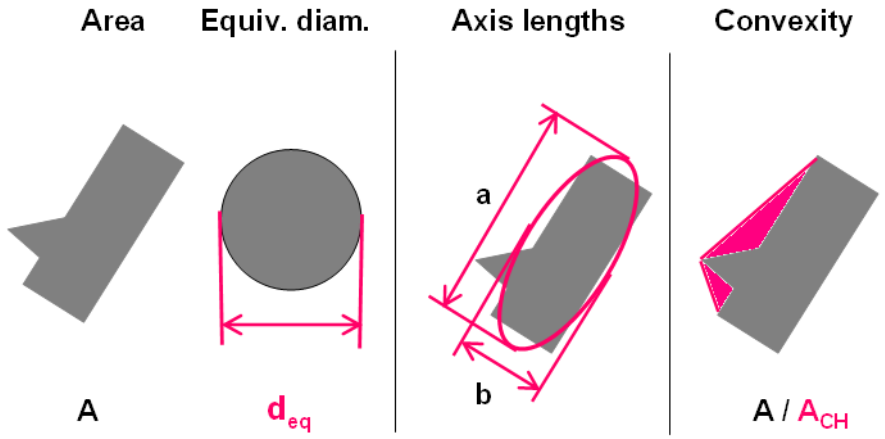

Figure 3.4: Commonly used shape factors

1. **Circle equivalent (CE) diameter:** Usually it is convenient to describe particle size using a single parameter which is most commonly calculated as circle equivalent (CE) diameter. CE corresponds to the diameter of a circle with the same projected area as the object. This parameter is used for the systems that are spherical, or close to spherical. The CE diameter for very different shaped particles could be characterized as identical simply because of having similar equivalent areas [128].

2. **Axis lengths:** It is a measure of elongation of particles and is defined as the ratio of major axis, a, to minor axis, b, length of the fitted ellipse with the same normalized second central moment as the identified area (aspect ratio $= a/b$). This metric is used for non-spherical particles that have one characteristic length sufficiently longer than the others [95]. Particles that are perfectly symmetrical in all axes, such as sphere, cube, will have aspect ratio of 1 and those with values larger than 1 will have an elongated shape. Hence, axis length distribution (ALD) provides 2D size and shape information [128].

3. **Convexity:** It is a ratio of the area of the particle (A) to its convex hull area (A_{CH}) (convexity $= A/A_{CH}$) and hence, is a measure of surface roughness of a particle. The convex hull area is obtained from the area of the smallest convex polygon that contains the identified region. This metric is used for distinguishing single particle and agglomerates or fragmented particles. Generally, convexity for single particles are much more larger than agglomerates or particle fragments [128].

Naturally, the distribution of equivalent diameter corresponds to the particle size distribution (PSD) of particles, if the particles are spherical.

As mentioned earlier, the system introduces magnification. Thus, the measured values (equivalent diameter and axes lengths) need to be converted to true values using the magnification factor M as

$$r = \frac{r_{pixels}\Delta x}{M_{d_o}}, \tag{3.1}$$

where r_{pixels} is the measured size of the particle in pixels, Δx the size of a pixel on the CCD camera, and M_{d_o} is the magnifying factor at the best focusing depth of each particle.

3.3 Experiments and results

In this section, several experiments are presented to verify the performance of the algorithm described in Section 3.2. The experimental set-up shown in Fig. 3.5, was used with a green laser (Lambda Photometrics DPGL3020, Harpenden, UK) of wavelength, $\lambda = 532$nm, a 60$\times$ microscope objective lens and 1 μm pinhole. The distance between point source and the CCD camera (The Imaging Source DMK41BF02, Bremen, Germany) for recording as D = 62 mm and for the reconstruction a point source to CCD camera distance $D' = 100 \times D = 6200$ mm was used. The camera used for the experiments had 1280 $\times$ 960 square pixels of size $\Delta x = \Delta y = 4.65\mu$m. Prior to all experiments the set-up was tested

with United States Air Force(USAF) resolution target. The obtained resolution was ≈ 7 μm for D = 62 mm.

The characteristics of the different samples used in this study are listed in Table 3.1. The threshold values for all the experiments were chosen as $t_L = 0.3$ and $t_H = 0.6$.

Table 3.1: Characteristics of various particles used in the study

Experimental system	*Average mean size*	*Shape*	*Opacity*	*Specific gravity*
Ceramic beads on glass slide	Diameter ≈ 80 μm	Spherical to elliptical	Opaque	High
Polymer microspheres in flow system	Diameter 40 μm	Spherical	Opaque	Medium
Microspheres in suspension	Diameter 10 μm	Spherical	Opaque	Medium
Single fiber on glass slide	Diameter ≈ 9 μm, length = 1320 μm	Needle	Opaque	Low
Carbon fibers in suspensions	Diameter ≈ 9 μm, length $\approx$ 50–500 μm	Needle	Opaque	Low

The standard deviation of the Gaussian filter was chosen $\sigma = 1.5$ for the first and second experiment in Table 3.1. Sigma, $\sigma = 1.5$ results in a filter size of 6×6 pixels. This filter length has been found to give good noise reduction without affecting the size of the smallest particles studied in these experiments which had a diameter of 40 μm or 17 pixels particles. These parameters were retained for the first two experimental systems listed in Table 3.1. In the 3rd experimental system, particles with a diameter of 10 μm, due to the small size of these particles, no Gaussian filtering was used prior to the edge detection. In the 4th and 5th experiments, carbon fibers of 9μm diameter and varying length were used, hence the Gaussian filter size was reduced to $\sigma = 1$.

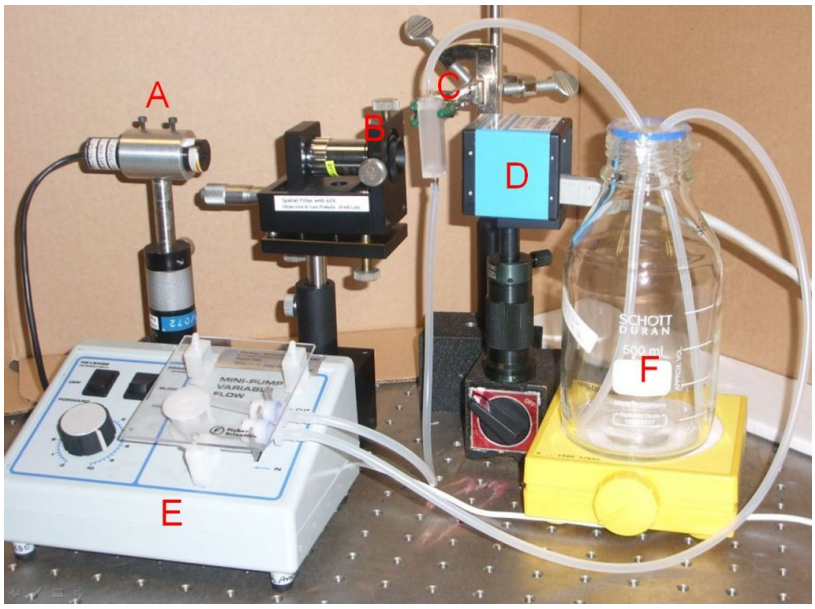

(a)

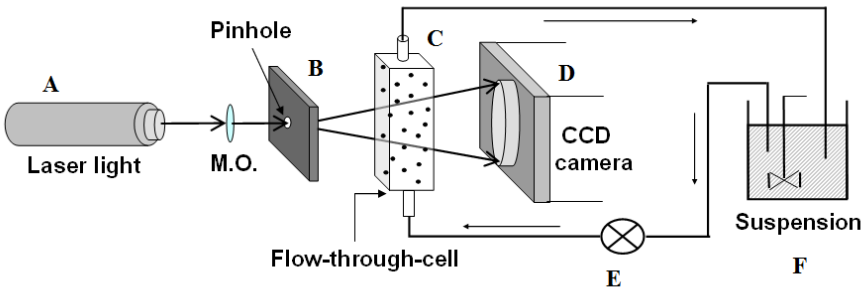

(b)

Figure 3.5: Experimental set-up of digital in-line holography: (a) An image of digital in-line holography set-up. (b) Schematic of the setup for flow-through system; M.O. stands for microscopic objective lens. A. Laser; B. Pinhole; C. Sample holder (holding flow-through-cell); D. CCD camera; E. Pump and F. Circulating liquid container placed on magnetic stirrer. 'E.' & 'F.' components are required for imaging of flowing suspension.

3.3.1 Verification of focusing algorithm

This section describes the set of experiments that were used to verify the accuracy of the localization step. For these experiments, the object consisted of seven ceramic beads with average sizes $\approx$ 80 μm positioned on a glass slide. The slide was positioned in the place of the object shown in Fig 3.5, normal to the optical axis so that the particles were located at the same depth. A hologram of this slide was captured. The slide was then consecutively displaced by 1 mm along the optical axis and a hologram was recorded for each displacement. The experiment was then repeated for a slide displacement of 0.1 mm. In both cases, the displacement was achieved with a device that had an accuracy of $\pm$ 0.1 mm. Following this, the focusing algorithm described in Section 3.2.3 was used to find the best focusing point for the particles of each hologram. In the case of 1 mm displacement, the algorithm was used to find the best focusing point within a depth range of 27.5 to 32.5 mm and in the case of 0.1 mm within a range of 20 to 34 mm. In both cases, the depth size between two consecutive reconstruction was selected as 50 μm. Following the focusing of the particles the depth of the slide for each position was estimated by averaging the depth of the particles.

Table 3.2 shows the measured slide positions for 1 mm and 0.1 mm displacements. The best focusing depth of the particles and the estimated slide positions are shown in Fig. 3.6(a) for the displacement of 1 mm and in Fig. 3.6(b) for the displacement of 0.1 mm. As can be seen in Table 3.2 and Fig. 3.6, the maximum observed error between the measured and the expected slide displacement is 120 μm. This translates into a 0.35 % error in the magnification, which is negligible.

3.3.2 Ceramic beads on glass slide

In order to verify the performance of the particle measurement algorithm, ceramic beads (Microbeads AG, Switzerland) with average size of $\approx$80 μm were used. This experiment

Table 3.2: Numerical results of the focusing algorithm for measuring the displacement of glass slide positions.

(a) 1 mm displacement

d (mm)	*Measured displacement* (mm)	*Expected displacement* (mm)	*Error* (mm)
32.26	–	–	–
31.19	1.07	1	0.07
30.11	1.08	1	0.08
29.03	1.08	1	0.08
27.91	1.12	1	0.12

(b) 0.1 mm displacement

d (mm)	*Measured displacement* (mm)	*Expected displacement* (mm)	*Error* (mm)
32.14	–	–	–
32.06	0.08	0.1	-0.02
31.94	0.12	0.1	0.02
31.81	0.13	0.1	0.03
31.73	0.08	0.1	-0.02

consisted of imaging a population of ceramic beads placed on glass slide. The slide was positioned normal to the optical axis so that the diverging beam of the light illuminates an area of glass slide containing a population of ceramic beads. A series of experiments were carried out in a similar fashion to account for a population of particles. The recorded holograms were processed following the procedure described in Section 3.2. For the reconstruction of each hologram, a step size of $50\ \mu\mathrm{m}$ covering a volume of depth size of $3\ \mathrm{mm}$ was used, *i.e.* the volume of 3 mm depth was sliced at 60 different steps. In addition, an scanning electron microscopy (SEM) was used to record several images of different particles taken from the same population. The SEM images were segmented using Canny edge detection, using the same parameters used for the segmentation of reconstructed image of hologram to extract the particles (bright areas). It should be mentioned that in the case of SEM, focusing was performed manually during the recording, and the magnification was provided automatically by the instrument. Hence, the size of each particle was measured considering the magnification of the SEM. On the other hand, in the case of

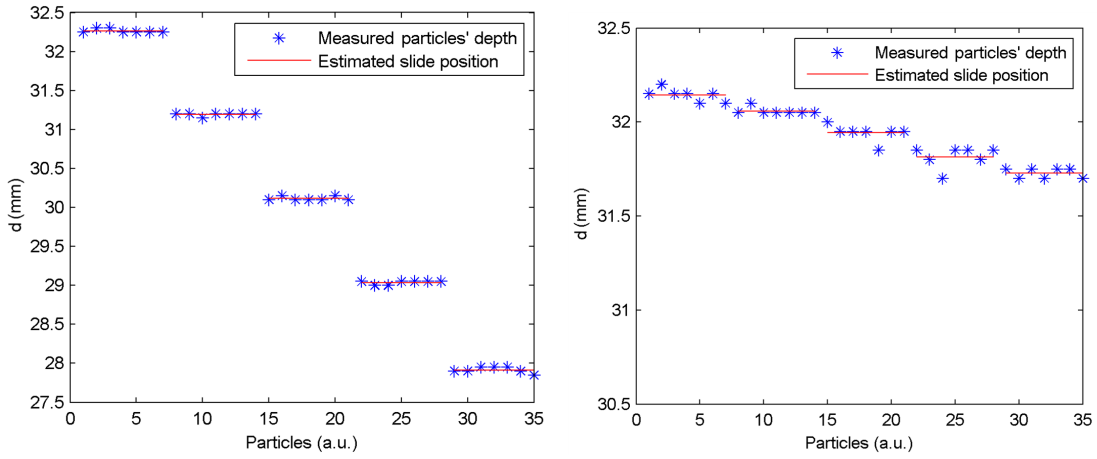

(a) (b)

Figure 3.6: Verification of the focusing algorithm: (a) for 1 mm displacement; and (b) for 0.1 mm displacement. Asterisks show the measured position of the particles and the lines show the estimated slide depth (average depth of the particles).

digital holography focusing and the calculation of the magnification factor was performed by the algorithm.

One of the experimentally recorded holograms and SEM images of ceramic beads are shown in Fig. 3.2(a) and Fig. 3.7(a), respectively. Figure 3.2(b) shows the corresponding reconstructed image of the hologram. The algorithm described in Section 3.2 identified 377 different particles from several holograms. In comparison, 615 different particles were measured from the captured SEM images. The resulting PSD measurements from the holography and the SEM experiments are shown in Fig. 3.7(b). The mean particle size identified from the holographic microscopy and the SEM are $80.24 \pm 14.46\mu$m (mean $\pm$ standard deviation) and $79.23 \pm 13.79\mu$m , respectively, showing good agreement. Hence, the results of this experiment verified the accuracy of the digital hologram based particle measurement algorithm.

The axis length distribution (ALD) of ceramic beads from the holograms are shown in Fig. 3.8. It can be seen from Fig. 3.8 that the major to minor axis length ratio, or aspect ratio for most of particles is close to 1, showing the sphericity of the particles. It can also

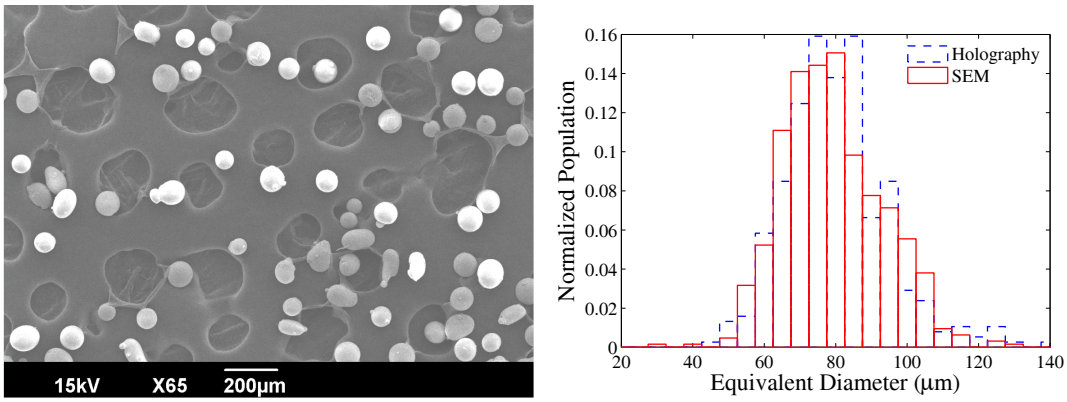

(a) (b)

Figure 3.7: Digital holographic microscopy data of ceramic beads on glass slide: (a) Example of an SEM image of ceramic beads. Bright areas correspond to particles whereas dark circular areas on the background are irregularities of the sample holder, and (b) Comparison of PSD obtained from digital holography and SEM.

be noted from Fig. 3.8 that some particles are not perfectly symmetrical leading to aspect ratios greater than 1. Visual inspection of particles from reconstructed hologram shown in Fig. 3.2(b) clearly indicates these particles.

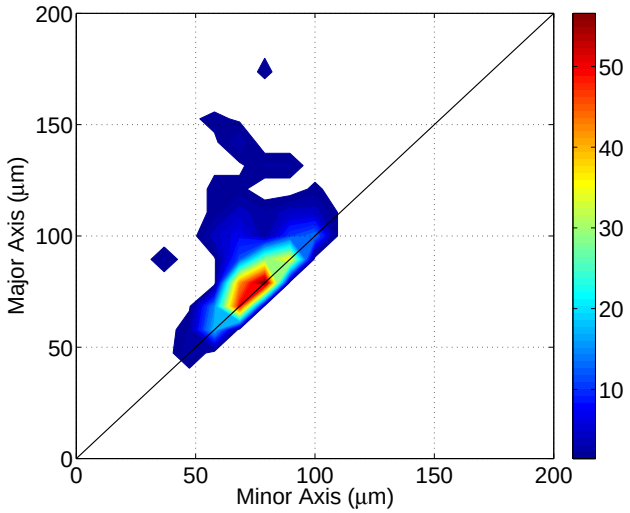

Figure 3.8: Axis length distribution of spherical ceramic beads.

3.3.3 Polymer microspheres in flow-through system

For this experiment, the object used in the set-up consisted of a flow cell with flowing particle suspensions. The schematic of this set-up was shown in Fig. 3.5(b). The National Institute of Standards and Technology (NIST) certified polymer microspheres manufactured by Duke Scientific Corporation, USA with mean diameter of $40.25\ \mu\mathrm{m}$ and standard deviation of $0.32\ \mu\mathrm{m}$, were continuously pumped from a beaker through circulation loop using a peristaltic pump. The particles flowed through a quartz flow cell with dimensions $12.5\ \mathrm{mm(L)} \times 12.5\ \mathrm{mm(W)} \times 65\ \mathrm{mm(H)}$ and optical path length of $10\ \mathrm{mm}$ at a flow rate 5 mL/min. Holograms were captured using the CCD at the speed of one frame per second. Reconstructions were carried out with a distance of $50\ \mu\mathrm{m}$ between each other covering a volume of depth size of $8\ \mathrm{mm}$, *i.e.,* 160 steps. The purpose of using this flow cell system is to represent the practical situations that is commonly encountered in most particulate processes, such as crystallization.

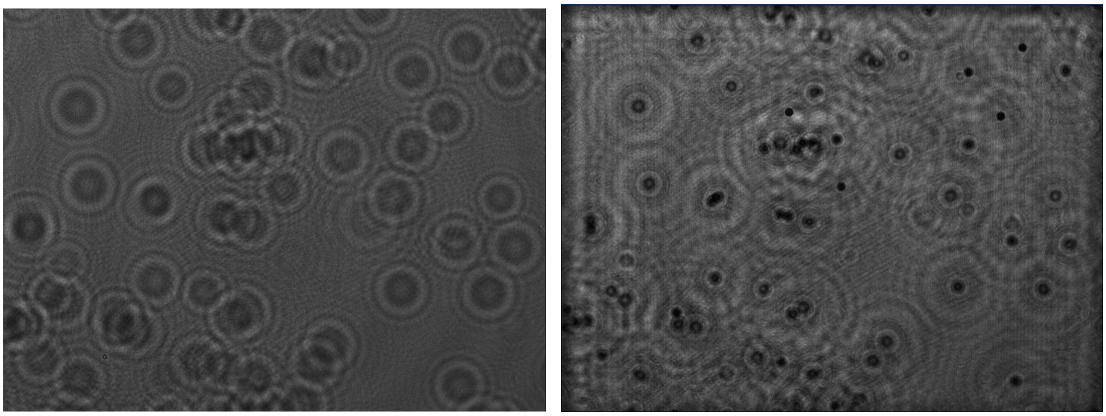

(a) (b)

Figure 3.9: Digital holographic microscopy images of $40\ \mu\mathrm{m}$ polymer microsphere suspension through flow cell: (a) A recorded digital hologram and (b) Example of a reconstructed image.

Figure 3.9(a) shows one of the recorded holograms and one of the corresponding reconstructed images is shown in Fig. 3.9(b). By analyzing nine holograms, the algorithm identified 437 different particles. The resulting PSD and ALD are shown in Fig. 3.10(a)

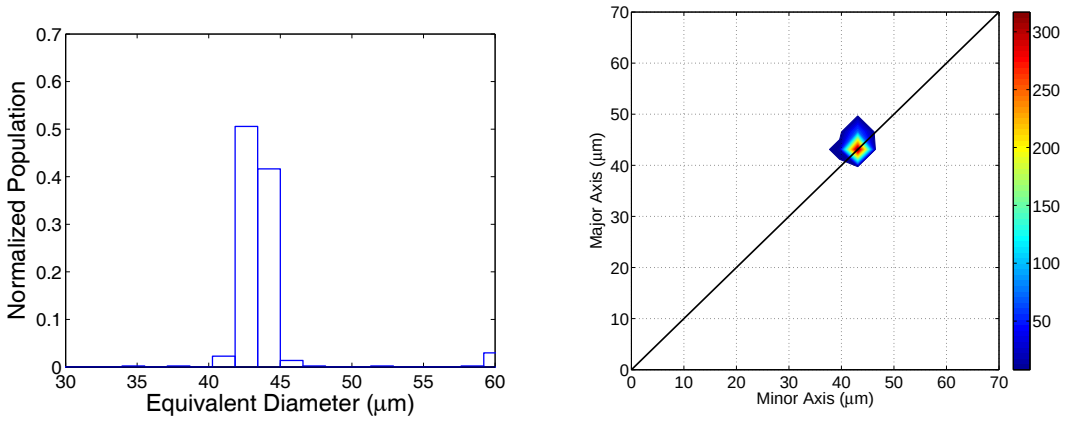

(a) (b)

Figure 3.10: Digital holographic microscopy data of 40 μm polymer microsphere suspension through flow cell: (a) Equivalent diameter distribution and (b) Axis length distribution.

and Fig. 3.10(b) respectively. The obtained mean particle size was 43.89 ± 3.38 μm. There is an error of ≈4 μm between the actual particle size and the location of the PSD peak. This error is below the resolution of the system (the obtained resolution for $D = 62$ mm is ≈7 μm). In Fig. 3.10(a), the presence of particles with diameter ≈60μm can also be observed. This indicates the presence of agglomerated or overlapping particles. In Fig. 3.10(b), the obtained ALD confirms the spherical shape of particles, as a majority of the particles are found to have an aspect ratio of 1.

3.3.4 Microspheres (10μm) in suspension

In this experiment, 10 μm particles suspended in water were examined. The sample was contained in a 12.5 mm(L) $\times$ 12.5 mm(W) $\times$ 48 mm(H) quartz cuvette. One recorded hologram was analyzed with a distance of 25 μm between two successive reconstructions covering a volume of 1mm depth size. From this single hologram, the algorithm identified 47 different particles. Figure 3.11(a) shows one reconstruction of the hologram and Fig. 3.11(b) the calculated PSD. The PSD showed that the method can measure particles

as small as 10μm with relatively large spread of $\approx$5μm around the expected mean size. As the particle size is very close to the resolution limit of the system ($\approx$ 7), the spread in PSD is quite significant. This result revealed the limited magnification of the system due to the system geometry and drew the limit of measuring minimum particle size by the lensless diverging system. This analysis concludes the fact that in order to measure the near micron sized particles, the system resolution needs to be improved, which can be achieved by introducing magnifying objective lens to the system.

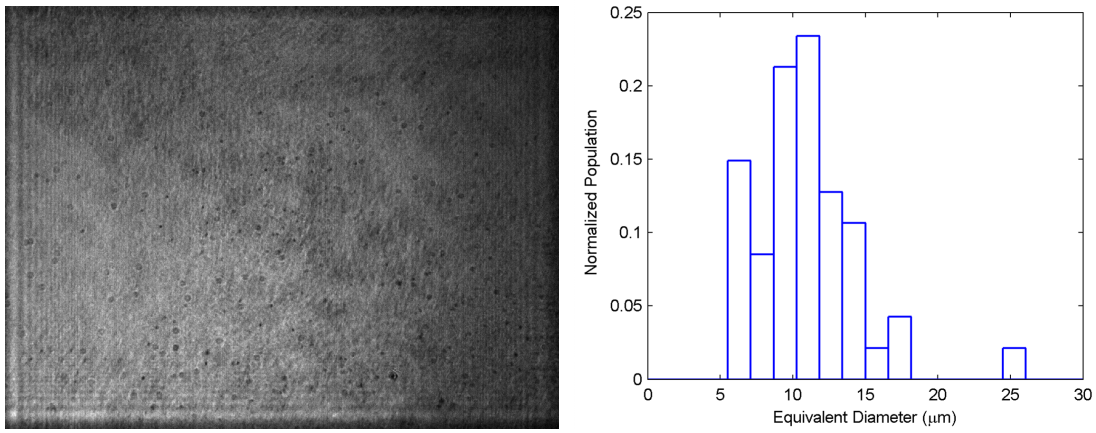

(a) (b)

Figure 3.11: Digital hologram of 10 μm particles suspended in water: (a) example of reconstruction; and (b) measured PSD from 47 identified particles.

3.3.5 Characterization of fibers

The measurement of fibers deserves special attention. Unlike the case of spheres, where each particle is best focused on a particular plane, the case of fibers is not straight-forward. Fibers that lie orthogonal to the optical axis, will be focused at a particular depth. However, for fibers that are not orthogonal to the optical axis, only a part of the fiber will be focused at particular depth. Under these situations, the algorithm would measure only the length of their projections on the reconstruction plane. In order to study this, the first set of experiments involved the measurement of a single fiber placed on a glass slide. In the

second set of experiments, measurements of a population of fibers in a solution were carried out. In this experiment, particles with needle shape were studied using carbon fibers (TOHO Tenax Type 383) suspended in water.

3.3.5.1 Single fiber on a glass slide

In the first set of experiments, a single fiber was placed on a glass slide connected to a rotatable mount that can be adjusted to obtain a desired out-of-plane tilt, as shown in Fig. 3.12. Two fibers with lengths 176 μm and 1320 μm, were allowed to be rotated

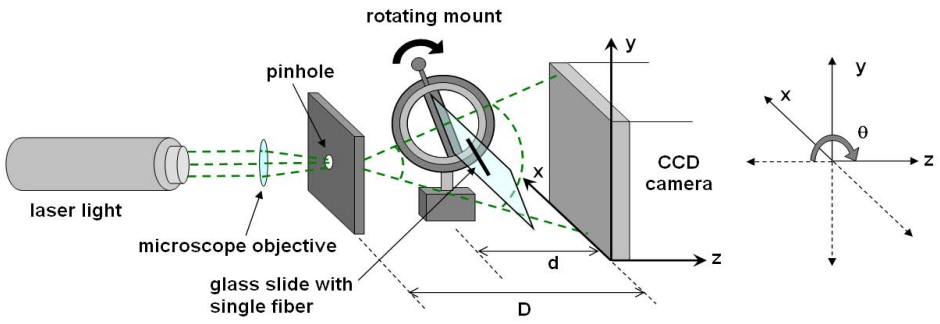

Figure 3.12: Digital holographic recording setup.

from 0° to 65° tilt at 5° interval with respect to the optical axis. The holograms were processed according to the algorithm discussed earlier. Since the fibers are clearly non-spherical, the major and minor axis obtained by fitting an ellipse were used to characterize the sizes. It is worth noting that while the fibers are rectangular, fitting an ellipse leads to an over prediction of the axis lengths. Hence, the measured length of the major and minor axis are multiplied by a factor of $\sqrt{3}/2$ to convert them to fiber length and diameter, respectively [129].

Based on the length and the angle of tilt the expected projected length, as shown by the continuous lines in Fig. 3.13(a) and Fig. 3.13(b), can be calculated. The comparison between the measured and calculated projected lengths is shown in Fig. 3.13. As it can be seen the algorithm successfully estimated the projected length of the 176 μm long fiber

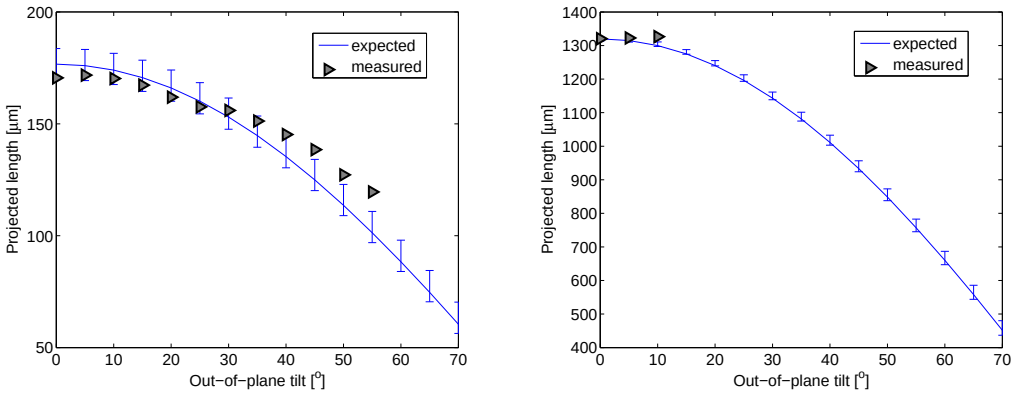

Figure 3.13: Measurement accuracy of the algorithm for fibers for out-of-plane tilt. (a) 176 μm long fiber; (b) 1320 μm long fiber. The error bars take into account the system resolution and the uncertainty in the measurement of the tilt.

within the expected accuracy even for large out-of-plane tilts. For the 1320 μm long fiber, the algorithm measured the fiber only for small tilts (cf. Fig. 3.13(b)). For higher tilts, long fibers are not entirely focused on a single reconstruction and hence the algorithm neglects such fibers, as they are not enclosed by strong edges. In this way, erroneous measurements are avoided but false negatives are introduced. It is worth pointing out that in the case of fibers, the measured lengths that are eventually identified correspond not to the real lengths but only the projected lengths.

3.3.5.2 Carbon fibers in suspension

Based on the understanding gained from the first set of experiments, measurements were performed with a population of carbon fibers contained in a quartz cuvette with dimensions 12.5 mm(L) $\times$ 12.5 mm(W) $\times$ 48 mm(H) with an optical path length of 10 mm. The recorded holograms were reconstructed with a step size of 20 μm between each other to cover a depth of 8 mm. One of the recorded holograms and a sample reconstruction are shown in Fig. 3.14(a) and Fig. 3.14(b), respectively. Using the procedure described in Section 3.2, 13 holograms were analyzed to identify 283 fibers. The resulting minor and

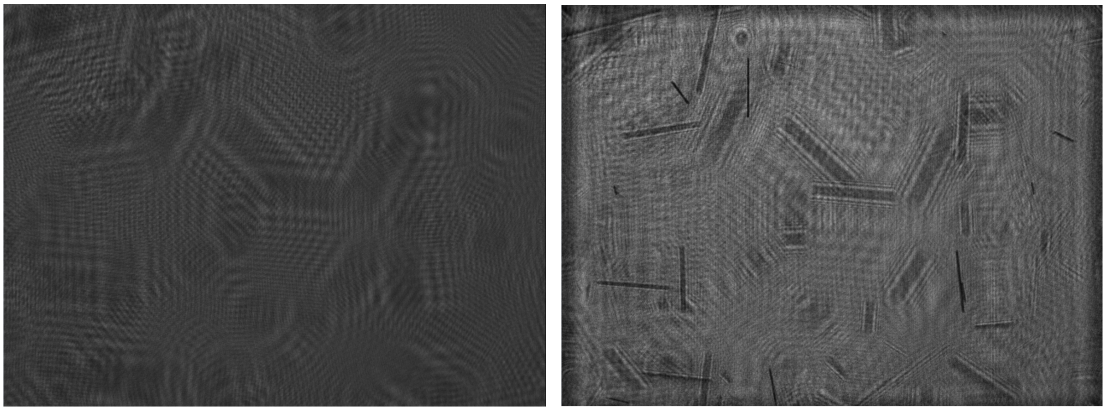

(a) (b)

Figure 3.14: Digital holographic microscopy images of carbon fibers suspended in water (a) A recorded digital hologram and (b) Example of a reconstructed image.

major axis length distributions are shown in Fig. 3.15(a) and Fig. 3.15(b), respectively. The obtained mean minor and major axis lengths of these fibers were 13.34 μm and 138.74 μm, respectively.

The axis length distribution shown in Fig. 3.15(c) is indicative of the shape of the particles and can be used to classify particle shape. While spherical particles tend to lie close to the diagonal, needle shaped particles with a very high major to minor axis ratios tend to lie near the ordinate axis. This information is of importance for researchers interested in particle characterization and is typically not obtained in conventional particle analysis systems. The ALD in Fig. 3.15(c) clearly shows that the population contains needle shaped particles with similar widths but varying lengths.

3.4 Further studies on the measurement of near-micron sized particles

Digital in-line holography based measurements addressed in this chapter are based on a lensless system, which imposed a stringent requirement for pixel size of sensor and axial

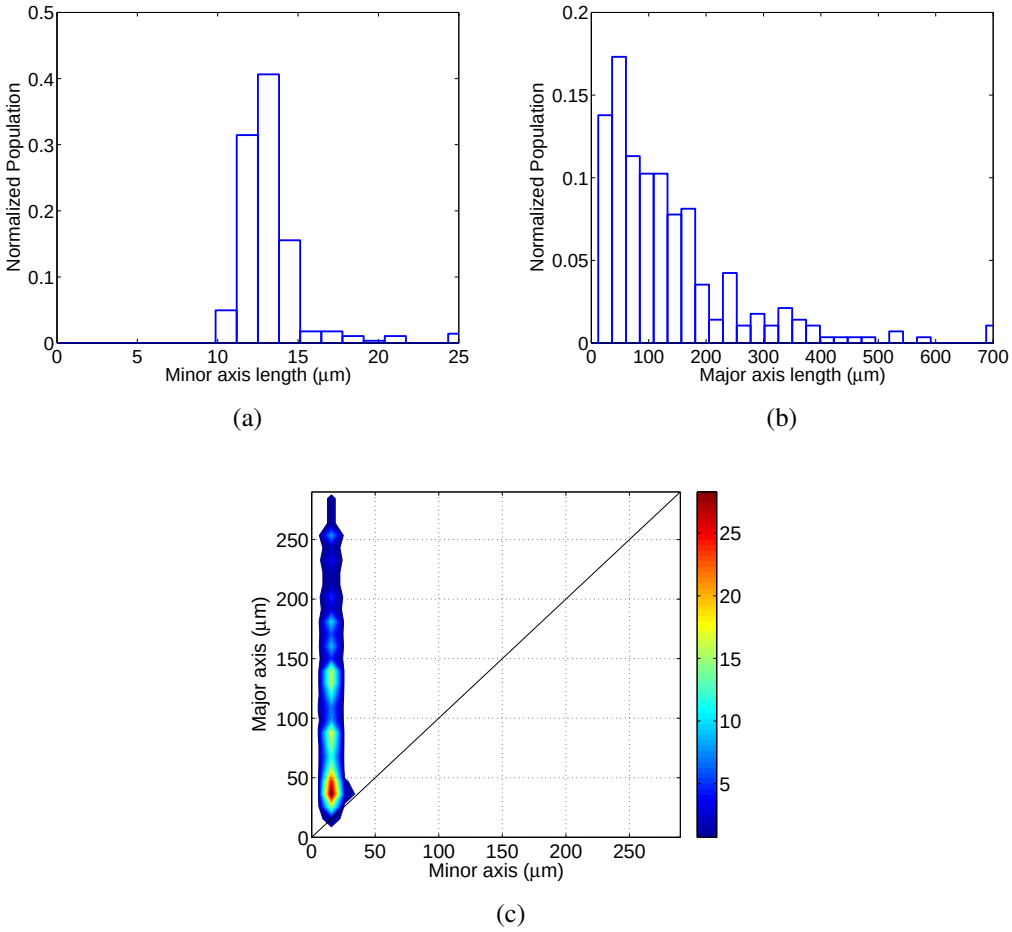

Figure 3.15: Digital holographic microscopy data of carbon fiber suspended in water: (a) Minor axis length distribution of carbon fibers; (b) Major axis length distribution of carbon fibers and (c) Axis length distribution of carbon fibers.

distances from the source of the reference and object beams to CCD. The lensless set-up provides magnification through the divergence of the beam as a function of reconstruction distance which is usually less than $5\times$. Thus the application of the lensless system is not suitable for resolving near-micron particle size. One possible way to improve the resolution and magnification of the system is to introduce a microscope objective (MO) in a in-line digital holography setup to study the near-micron particle system. This MO can be used as a relay lens inserting between samples and CCD to pre-magnify the samples. While the details of the lensless system were investigated thoroughly, those with the MO were performed as a proof-of-concept study.

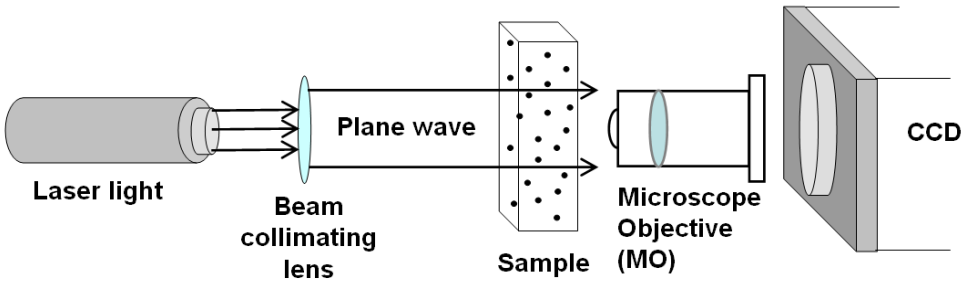

Figure 3.16: Schematic of the digital in-line holographic setup with single microscope objective.

The experimental results for quantitative measurement of near-micron particles were studied by using particles with a certified diameter of 1 μm and 5 μm to show the efficiency and reliability of the in-line setup with MO. The experimental setup used for this study is shown in Fig. 3.16. It is worth noting that unlike the lensless system where a diverging beam was used to provide the magnification, a simple collimated beam (plane wave) is used in the experiments with the MO. All the tools described for image acquisition and hologram reconstruction can be used in the exact manner as described earlier, however in a simpler form, as it is no longer necessary to account for the magnification due to the diverging beam. For extracting particle information from the reconstructed images, Canny edge detection is used to identify particles on each reconstruction as described earlier. The

list of experimental system used in this study is summarized in Table 3.3 along with their measured results. In the following sections details of the experimental results are discussed.

Table 3.3: Experimental system and measured data for the measurement of near-micron particles

Certified mean size of microspheres (μm)	*Power of MO*	*Calculated magnification, M*	*Pixel resolution, $\Delta\xi/M$, (μm/pixel)*	*Field of view, $N\Delta\xi/M$, (mm×mm)*	*Measured mean size of microspheres, (μm)*
5.003±0.040	10×	10.01	0.4645	0.595×0.446	5.13±0.32
-	20×	19.88	0.2339	0.299×0.225	5.07±0.71
1.034±0.020	40×	39.66	0.1172	0.150×0.113	1.05±0.18
-	60×	60.76	0.0765	0.098×0.073	1.05±0.15

Measurement of 5μm particles For the measurement of 5μm mono-sized microspheres in suspension, two separate experiments were conducted using 10× and 20×, respectively. A total 15 holograms of suspended particles were recorded using 10× MO and 13 holograms were recorded using 20× MO.

Figures 3.17(a) and 3.17(c) show example of digital hologram of 5μm particle suspension in volume magnified by 10× MO and 20× MO, respectively. A total 667 and 536 particles were identified by analyzing the holograms captured using 10× MO and 20× MO, respectively. The corresponding PSD of obtained particles is shown in Fig. 3.17(b) and Fig. 3.17(d), respectively. The mean particle size obtained from the PSD of 10× magnification is 5.13±0.32 μm. For the 20× magnification the measured mean size is 5.07±0.71 μm while the certified mean size of the population of microspheres is 5.003±0.040 μm showing good agreement with each other.

Measurement of 1μm particles For 1 μm polymer microspheres, a MO with higher magnification power, *e.g.*, 40× or 60×, was used to record the hologram.

A hologram of 1μm particles suspension with 40× MO is shown in Fig. 3.18(a). Twenty holograms were recorded and image analysis were applied on the reconstructions which identified total 1015 particles. The PSD obtained from this analysis is shown in

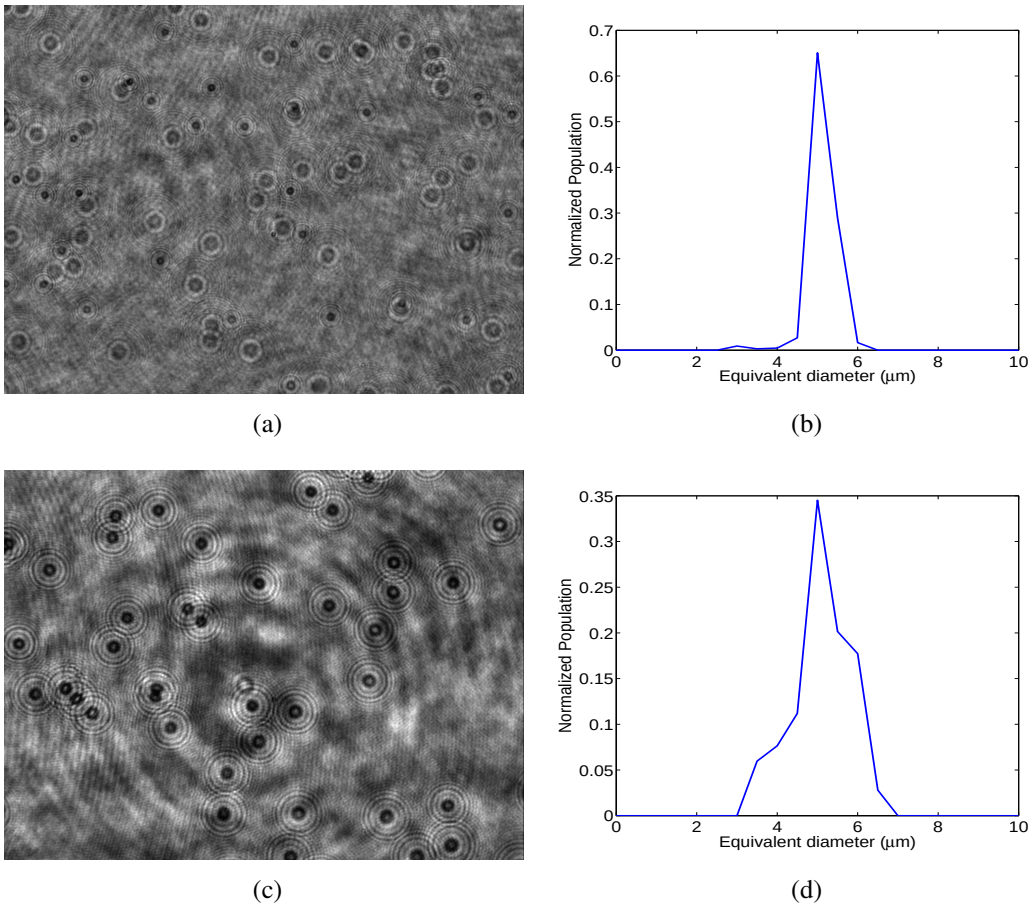

(a) (b)

(c) (d)

Figure 3.17: Characterization of 5 μm particles in suspension using digital holography with MO: (a) Hologram of 5 μm particles magnified by 10 $\times$ microscope objective;(b) Equivalent diameter distribution of 5μm particles measured from 10$\times$ magnified holograms; (c) Hologram of 5 μm particles magnified by 20$\times$ microscope objective; (d) Equivalent diameter distribution of 5 μm particles measured from 20$\times$ magnified holograms.

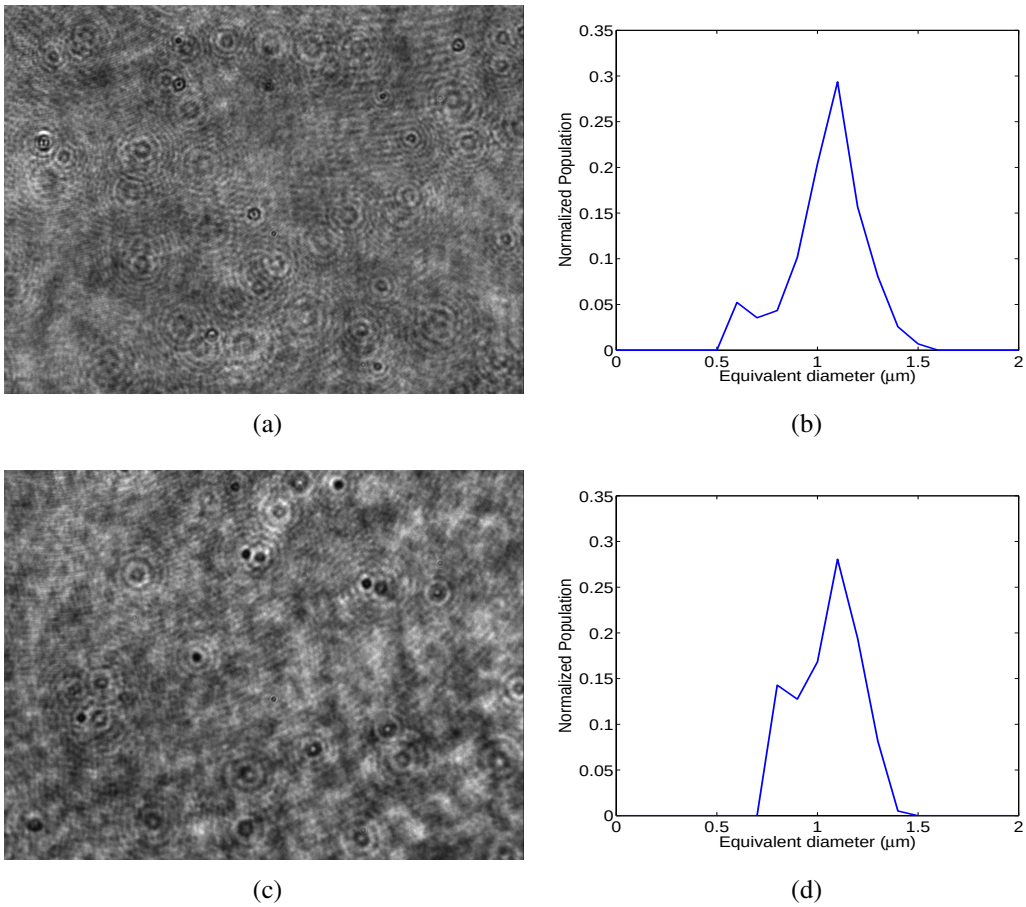

(a) (b)

(c) (d)

Figure 3.18: Characterization of 1 μm particles in suspension using digital holography with MO: (a) Hologram of 1 μm particles magnified by 40 $\times$ microscope objective; (b) Equivalent diameter distribution of 1μm particles measured from 40$\times$ magnified holograms; (c) Hologram of 1 μm particles magnified by 60$\times$ microscope objective; (d) Equivalent diameter distribution of 1μm particles measured from 60$\times$ magnified holograms

Fig. 3.18(b). The measured mean size of particles is 1.05±0.18 μm. Figure 3.18(c) shows a example of 60× magnified hologram of 1μm particles in suspension. Total 10 holograms were captured using 60× MO and processed. From the analysis of the reconstructed images, total 196 particles were identified. The corresponding size distribution of identified particles is shown in Fig. 3.18(d). The measured mean size of particles is 1.05±0.15 μm. Comparing with the certified particle size 1.034±0.020 μm, the mean size obtained using both 40× and 60× magnification gives good measurement accuracy. This approach of using microscope objective is promising and deserves further study.

3.5 Chapter summary

In this chapter, a particle size measurement methodology based on digital holographic microscopy was presented. The steps of the measuring procedure were described in detail. Apart from the known parameters related to the recording (such as the wavelength and the reconstruction distance) and the minimum size of particles to be identified, the method requires the selection of a small set of unknown parameters, namely the standard deviation of the Gaussian filter and the threshold values needed for the edge detection. The effectiveness of the algorithm, however, is not very sensitive to these parameters, as shown through a series of experiments conducted for particles with different shapes, size ranges, and conditions. It has been shown that the algorithm scanned a volume of depth ≈10 mm and successfully performed automatic focusing and quantification of particle size and shape. Hence it overcomes the challenge concerning out-of-focus objects within a volume of depth encountered in the field of photography. Even for the special case of randomly oriented fiber, the algorithm successfully measured the projected lengths with good accuracy, unless the fiber is highly tilted. Considering the fact of highly oriented needle like particles in volume, the algorithm is limited to the application of measuring projected length of those particles. Finally the applicability of digital holography for

the measurement of near micron particles (particle diameter= 1 μm and 5 μm) was also demonstrated by using a microscope objective to provide the necessary magnification. The results obtained in this chapter extend the potential of digital holography for applications in particle characterization and on-line monitoring of particulate processes.

Chapter 4

Three-dimensional imaging of needle shaped particles: 3D point cloud method

4.1 Introduction

The algorithm discussed in previous chapter was developed to measure the size of particles from the projections of the 2D reconstructed images at different plane. While this does not affect the measurement of spherical particles, retrieving the real size of needle shaped particles from the measured projected lengths requires information about the angle of orientation which is difficult to obtain [120, 130]. In literature, a few algorithms have been developed for localization and measurement of needle like particles which require prior-knowledge about the orientation or the size of the object [112–114]. However, in several practical situations, *e.g.*, for a population of fibers in a solution, such information is seldom known and hence limiting the application of these techniques. In this chapter we develop a method called as the "3D point cloud method" based on a simple optical setup to obtain 3D orientation, location, and size of micro-fibers without *a priori* knowledge of orientation, location and size of the object. The proposed method is benchmarked with a single fiber of known length and orientation. The potential of the method for accurate measurement

of fiber length is further demonstrated by applying it to a suspension of fibers of unknown lengths and orientations. Since the algorithm can be applied with no information about the orientation or the size of the fiber, it opens up the possibility of using digital holography for particle characterization where determining the size and shape of non-spherical particles is still a major challenge. The results presented in this chapter were published in Optics Express [131].

4.2 Methodology for 3D measurement of micro-fibers

To describe the algorithm, the hologram shown in Fig. 4.1 is used. The hologram was recorded using an opaque carbon fiber (type T383, Toho Tenax Europe GmbH, Wuppertal, Germany). The diameter and the length of the fiber, measured by a microscope were 7 μm and 1320 μm, respectively. The fiber shown in Fig. 4.1 is tilted to an angle of 60° along the optical axis. Figure 4.1(b) shows a reconstruction of the hologram where it can be seen that only the middle part of the fiber is in focus at this particular reconstruction distance. The reconstructed hologram shows the projection of the fiber on the xy plane, from where the length of the fiber would be erroneously measured by an image analysis method as $\sim$ 700 μm, unless the out-of-plane tilt was known. The automated technique described next measures the fiber length within a volume and not on a single projection, yielding correct size measurements without *a priori* knowledge of the fiber's tilt or position. A flow chart of the processing algorithm is shown in Fig. 4.2. In the next few sections the details of the processing steps of this method is discussed followed by experimental results.

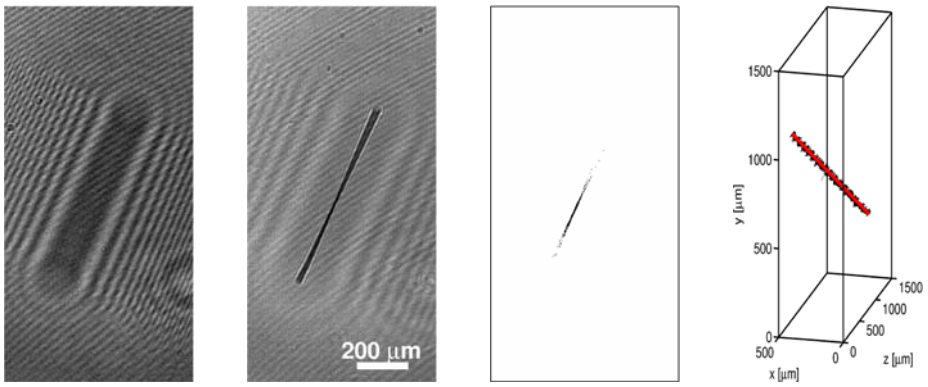

(a) (b) (c) (d)

Figure 4.1: Three-dimensional profiling of a tilted fiber: (a) recorded hologram; (b) a sample reconstruction; (c) thresholded reconstruction; and (d) point cloud with fitted line.

4.2.1 Hologram acquisition and processing of reconstructed holograms

The recording of digital holograms was performed using the setup shown in Fig. 3.12. Hologram of the sample is recorded and numerically reconstructed at several depths, with $0 < d < D$, covering the volume of the sample to be studied using the method described in Section 2.2. The number of reconstruction steps is typically set by the minimum shortest length of fibre that is expected to be detected. Small values of d result in increasing the total number of reconstructions thereby resulting in increasing the computational load. Larger increments in between two successive reconstructions might lead to errors in determining the sizes as some focused part of the object may have been missed out in that depth interval. Hence the number of reconstruction should be set close to the minimum shortest length of the fiber.

4.2.2 Image analysis

After reconstructing the hologram at N_z equally spaced intervals (taken as $N_z = 300$ with 20 μm increment in this chapter), histogram equalization is performed on the intensity

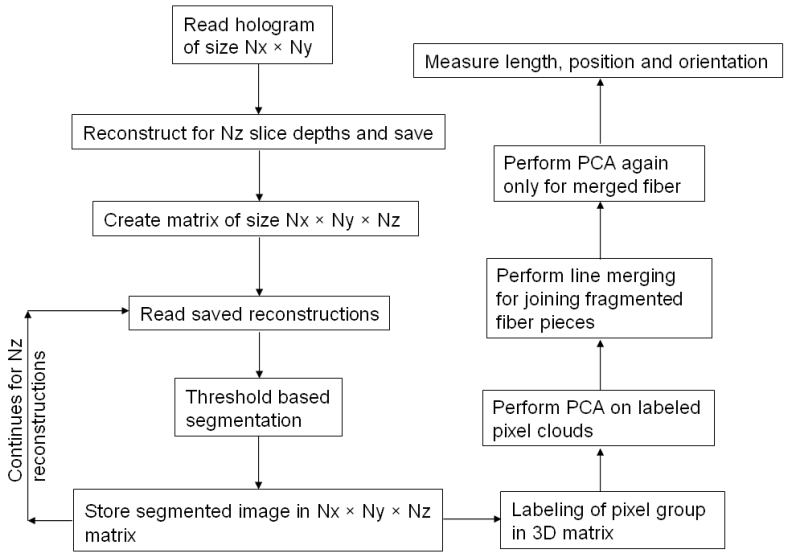

Figure 4.2: Processing algorithm flow chart for 3D point cloud method.

of the complex valued reconstructions to account for variations of the intensity's range. The gray scale images are then converted to binary images using a simple threshold. The threshold is chosen in such a way that only the darkest pixels, which correspond to pixels in focus, are accepted as being part of fiber and are set to 1 in the binary image. The rest of the pixels are considered to be background and their value is set to 0 in the binary image. In this chapter, a threshold of 5 (on a scale of 0 (black) to 255 (white)) was used for the equalized images and almost identical results were obtained for threshold values up to 15. Figure 4.1(c) shows a thresholded reconstruction where in-focus parts of the fiber appear in black.

4.2.3 Storing pixel clouds in 3D matrix

The binary images obtained after thresholding are stored in a 3D matrix A of size $N_x \times N_y \times N_z$, whereas $N_x \times N_y$ is the dimension of the image plane and N_z is the number of reconstruction. Thus the matrix A contains different clouds of points that correspond to the focused pixels of a fiber at different reconstruction depths. Pixels that are

connected in 3D are assigned identical group labels, so that each point cloud corresponds to a different fiber. Now there might have chances to appear broken up fibers due to high threshold. In order to merge the broken up parts, 3D dilation followed by 3D erosion is performed on A. To avoid identifying noise as fibers, groups with number of connected pixels smaller than a cut-off value are removed. Groups of connected pixels touching the reconstruction edges are also removed, since they are likely to be part of a fiber partially located outside the reconstruction volume. Following this, connected pixels within A are finally grouped together. Figure 4.1(d) shows the point cloud of the fiber in black.

4.2.4 Size and orientation measurement by 3D line fitting

Since the micro-fibers are elongated rods, fitting a straight line on each group of pixels yields the orientation and length. In this step, each group of pixels correspond to individual fiber is fitted with a straight line to yield their orientation and length. For fitting lines, traditional regression methods, such as least squares, are inadequate as they are based on the assumption of error free predictors. However, as it can be seen in Fig. 4.1(b), the intensity of the reconstruction is contaminated by speckle noise resulting in noisy point clouds. Hence, tools such as the principal component analysis (PCA) that can account for errors in the predictors have to be utilized [132]. Figure 4.1(d) shows the line that was fitted to the point cloud of the tilted fiber using PCA. From this line the characteristics of the corresponding fiber (location, size, and orientation) can be measured. Results verifying the accuracy of the proposed method are discussed in the next section.

4.3 Experiments and results

In this section, the proposed method for measuring real length of fiber is benchmarked with a single fiber of known length and orientation. Further, the method is demonstrated through

it's application to a suspension of fibers of unknown lengths and orientations.

4.3.1 Single tilted fiber

Performance with long fiber (1320 μm) The method outlined in Section 4.2 was applied for validation purposes first to the fiber of known length and orientation shown in Fig. 3.12. In this experiment, the fiber (type T383, Toho Tenax Europe GmbH, Wuppertal, Germany) with a diameter of 7 μm and a length of 1320 μm (measured by microscope) was positioned on a glass plate, which was fixed to a revolving mount (See Fig. 3.12). The revolving mount allowed for a setting of the out-of-plane-tilt of the sample with an accuracy of 1°, and was positioned between the pinhole and the camera. The CCD camera was positioned at a distance of $D = 63.3$ mm from the pinhole, whereas wavelength of laser light and CCD specifications were retained same as the previous experiments. A total of 17 different angles were used, varying from 0°, where the fiber is positioned perpendicular to the optical axis of the system, to 80°. For angles larger than 80°, the glass plate prevented the fiber from being seen in the reconstruction.

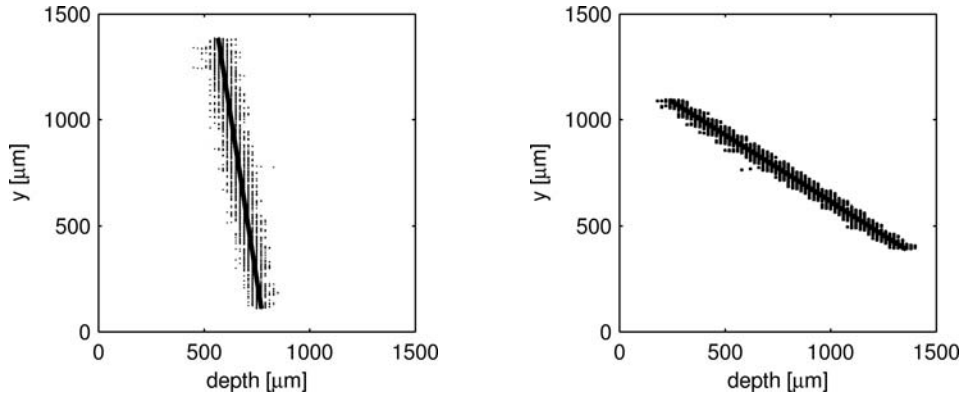

Figure 4.3: Point cloud and fitted line for 1320μm fiber: (a) for 10° tilted fiber; and (b) for 60° tilted fiber. The concentrated dots represent point clouds while the line represents the best fit.

In Fig. 4.3, the point clouds for the fiber at a tilt of 10° and 60°, along with the line

fitted to it, are shown. Figure 4.4 shows the comparison of the resulting orientation and length of the fiber with the true orientation and length. As can be seen from Fig. 4.4(a), the method accurately measures the fiber orientation with less than 3 degrees error. The same conclusion also holds for the measured fiber length, which corresponds very well to the true fiber length over a large range of tilts with relative errors below 4% (See Fig. 4.4(b)). Overall, the ability of the proposed method to accurately determine fiber location, length, and orientation has been demonstrated.

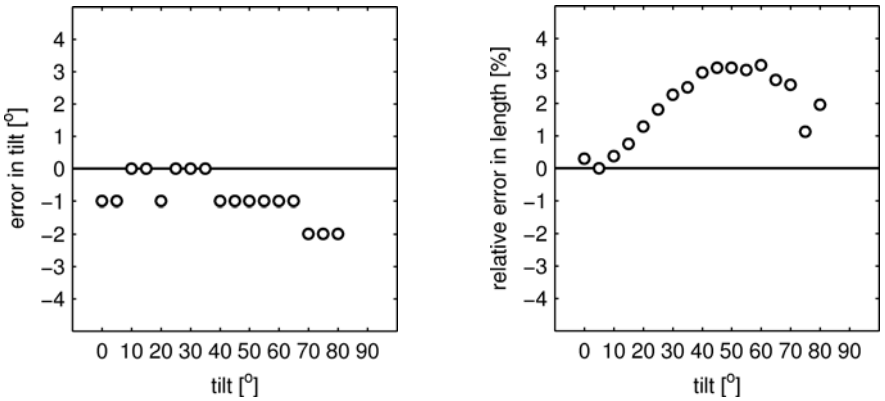

(a) (b)

Figure 4.4: Measurements for 1320 μm long fiber: (a) Error in the measurement of the fiber's orientation, and (b) relative error in the measured fiber length for different out-of-plane-tilts of the fiber.

Performance with short fiber (176 μm) The performance of the point cloud method was tested using a shorter fiber of length 176 μm. Similar to the previous case, the fiber was placed on a rotatable mount which was positioned between 0 to 65° at 5° intervals. All other system parameters were maintained as before.

Figures 4.5(a) and 4.5(b) show the point clouds of the short fiber for 10° and 60° tilt, respectively. As can be seen from Fig. 4.5, for lower tilts the point clouds show a good description of the expected 3D orientation of the fiber. However at larger tilts the owing to shorter projected lengths, the dimensions of the point clouds in the x and y directions become comparable and the PCA algorithm fails to recognize the true length of the fiber.

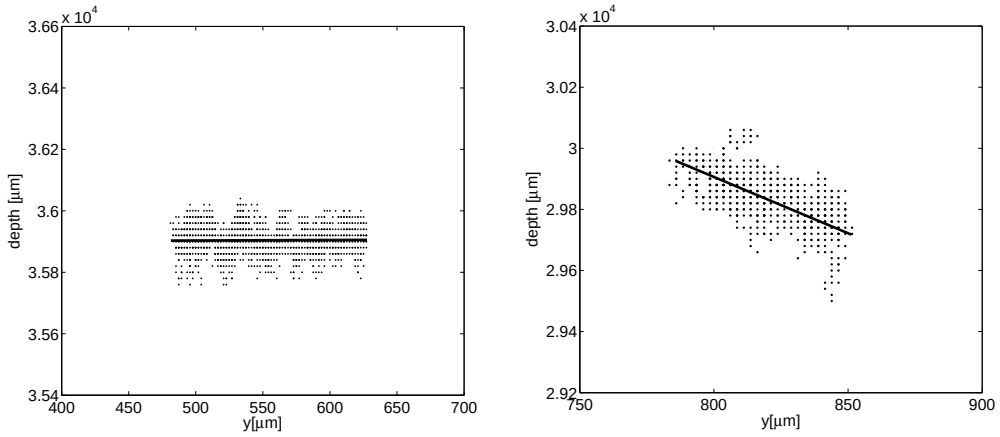

(a) (b)

Figure 4.5: Point cloud and fitted line for 176 μm long fiber: (a) for 10° tilted fiber, and (b) for 60° tilted fiber. The concentrated dots represent point clouds while the line represents the best fit.

This leads to significant errors in the measurement of these fibers. It is worth noting that in longer fibers, this limitation will be reached only for significantly larger tilts.

Figure 4.6 shows the comparison of the resulting orientation and length of the short fiber with the corresponding experimental settings. As can be seen from Fig. 4.6(a), the method measures the fiber orientation with maximum 21° error, while Fig. 4.6(b) shows the relative error in measured length is less than 10% only up to 45° tilt. At higher tilts, the measured length and tilt deviate significantly from the expected values. This illustrates that the "3D point cloud method" requires improvement for the accurate measurement of short fibers.

4.3.2 Fibers in suspension

Based on the understanding developed from the above discussion, the proposed method was applied in a real particle analysis setting. For this experiment, a suspension of carbon fibers with unknown length in water was prepared and contained in a quartz cuvette with dimensions 12.5 mm(L) $\times$ 12.5 mm(W) $\times$ 48 mm(H). The cuvette was positioned at a distance of 35 mm from the recording camera and the hologram shown in Fig. 4.7(a) was

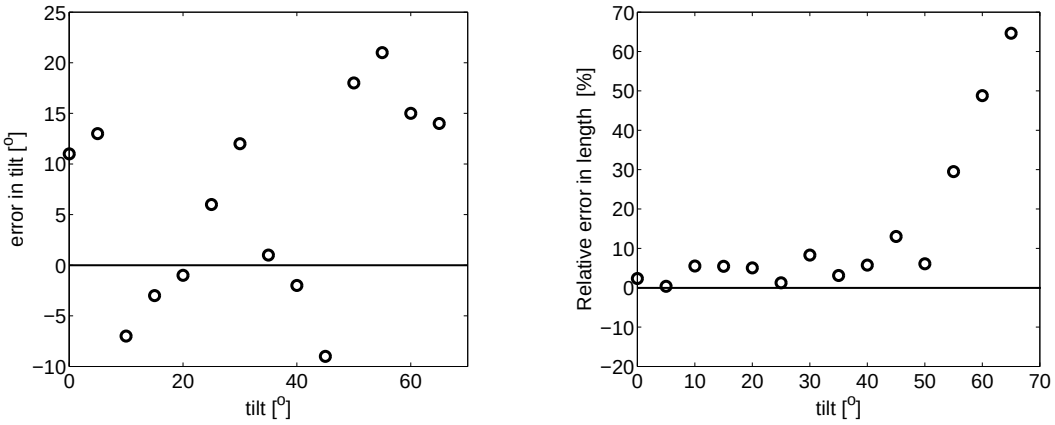

(a) (b)

Figure 4.6: Measurements for 176 μm long fiber: (a) Error in the measured orientation of the fiber by the 3D point could algorithm, and (b) relative error in the measured length by the 3D point could algorithm for different out-of-plane-tilts of the fiber.

recorded. Figure 4.7(b) shows a reconstruction of the hologram, where a few focused and several out of focus fibers at this particular reconstruction distance can be seen. The algorithm was applied to the recorded hologram and the resulting 3D image of the volume is shown in Fig. 4.8 and the corresponding measurements are listed in Table 4.1. The algorithm successfully identified 7 fibers and measured their position, length, and orientation within the studied volume.

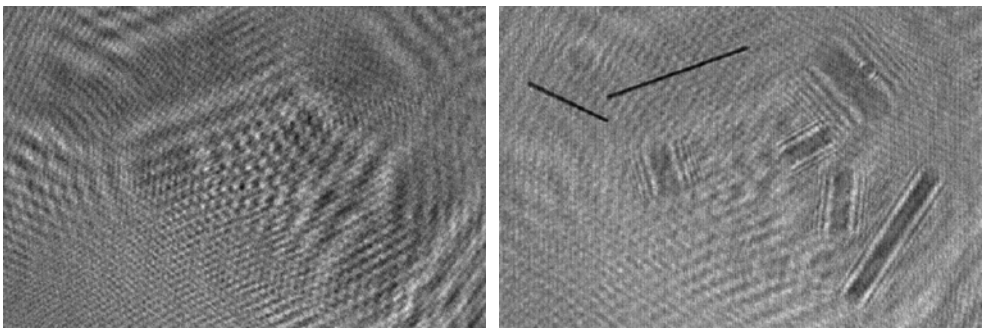

(a) (b)

Figure 4.7: Digital hologram and a corresponding reconstructed image of microfiber suspension: (a) Hologram of a suspension of fibers in water; and (b) a sample reconstruction.

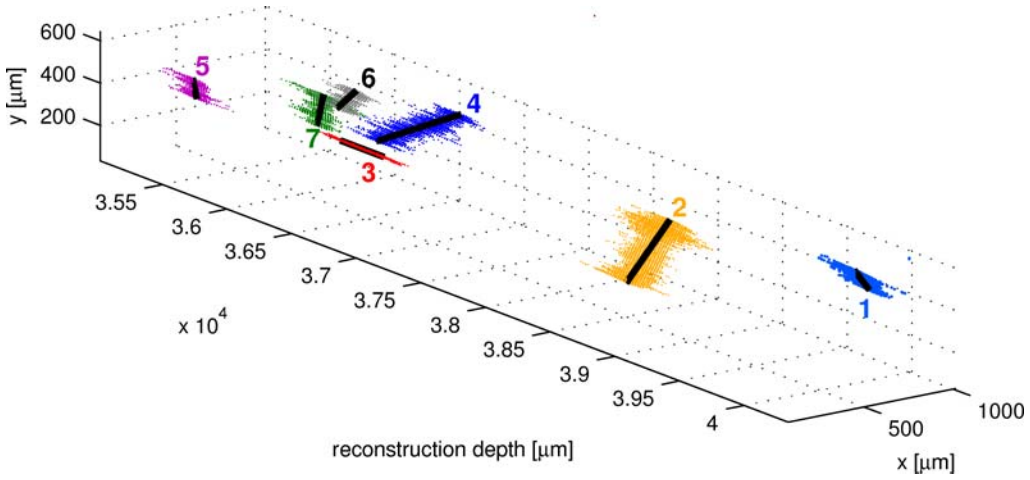

Figure 4.8: 3D image of a volume of carbon fibers in suspension, viewed from two different directions and showing both the lines fitted by PCA (black lines), as well as the point clouds (colored dots).

Table 4.1: Tilt, length and location measurements of identified fibers in Fig. 4.8.

	centroid location			orientation		
fiber	x [μm]	y [μm]	z [mm]	xy [°]	yz [°]	length [μm]
1	766	498	39.967	-48	14	166
2	918	176	38.094	57	16	352
3	169	512	36.913	-26	-38	226
4	435	538	36.985	19	59	407
5	425	372	35.264	-74	4	111
6	779	419	35.953	30	-2	133
7	876	275	35.615	85	13	159

Although the measurement accuracy of the fiber suspension cannot be inferred from this measurement, the study of fiber suspension however shows the potentiality of applying the method to the volume of fiber suspension.

4.4 Chapter summary

In this chapter, a digital holography based measurement method, '3D point cloud algorithm', has been presented for simultaneous measurement of length, orientation, and location of opaque fibers. The potential of the technique was demonstrated using single fibers of known length and orientation, and subsequently using a suspension of fibers with random orientations and unknown lengths. The results obtained for long fiber with large variety of tilts using the automated 3D point cloud algorithm showed good agreement with the known sizes and tilts. However, for short fiber the applicability of the method is still limited to the low tilted fibers. While the technique offers a distinct advantage over the '2D projection algorithm' described in Chapter 3, it has two practical shortcomings. Firstly, this method is memory intensive as the matrix used for storing the binary images can be as large as $1280 \times 960 \times 400$ for our system and results in slow processing time. Secondly, when measuring short fibers, where the length and width of the point cloud becomes comparable, the PCA yields erroneous results. However the method presented in this chapter requires no *a priori* information about the size or the orientation of the object, which is unlike to other methods reported in the literature. Hence it opens up promising possibilities in the field of particle analysis and characterization where the simultaneous measurement of both particle size and orientation is of great interest. In order to overcome the limitations of the point cloud algorithm, an alternative technique was developed and is described in the next chapter.

Chapter 5

Three-dimensional imaging of needle shaped particles: Superimposition method

5.1 Introduction

From the discussion in previous chapters, it is clear that the 2D projection algorithm is well suited for the measurement of the projected length of short fibers and the 3D point cloud algorithm performs well for the measurement of the real length of long fiber. This chapter proposes an efficient algorithm to measure size, position and orientation of a population of microfibers in a 3D volume spanning an order of magnitude in length. The image analysis routine is simpler and computationally less intensive compared to the methods described in earlier chapters. In summary, the new algorithm bridges the two techniques discussed in Chapters 3 and 4, while increasing the measurement accuracy and reducing the computational load. The performance of this method is compared with the methods, '2D projection algorithm' and '3D point cloud method', using a single fiber of known length and orientation. Further the new method has been applied to a population of microfibers

in suspension and the measurements are compared with the real particle size distribution (PSD) of the same microfiber population measured by microscopy.

5.2 Methodology of superimposition algorithm

The algorithm introduced in this chapter is called the "superimposition algorithm". The block digram of the superimposition algorithm is shown in Fig. 5.1. The major steps in the processing algorithm are described in detail in the following sections.

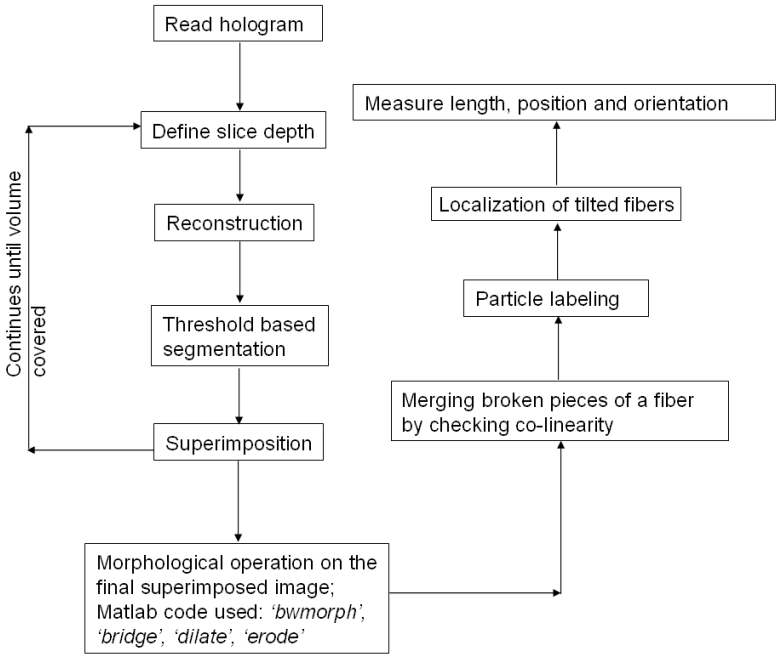

Figure 5.1: Processing algorithm flow chart for Superimposition method.

5.2.1 Recording and reconstruction

The recording and reconstruction procedure of a hologram is identical to the one described in Section 2.2. An example of a hologram is shown in Fig. 5.2(a). The key aspect of this step is the use of a convolution based reconstruction method that takes into account the magnification as a function of reconstruction distance. The number of

reconstruction steps is an important parameter. On one hand, small increments between two successive reconstructions result in increased computational load. On the other hand, larger increments between two successive reconstruction might lead to errors in determining the lengths. It is recommended that the increment be chosen such that it corresponds to the shortest length of the fiber that is expected to be detected.

5.2.2 Image segmentation

After the reconstructions have been performed, the complex valued reconstructions are converted to gray scale images (a scale from 0 (black) to 255 (white)) and then converted to binary images by choosing an appropriate threshold. While choosing the threshold several factors need to be considered, *e.g.*, it should be neither too stringent as it leads to the formation of broken fibers, nor it should be too relaxed as it increases the noise. In addition, the intensity variations due to laser imperfection, multiple object light scattering and related non-uniform illumination have to be considered. These effects can be difficult to handle using an absolute value of threshold. As an alternative, the proposed algorithm first reconstructs the hologram at half the depth of the 3D volume and the average intensity of the resulting image is calculated. A fraction of this average intensity is chosen as the threshold value for all other holograms measured for the particular experiment. The fraction is chosen, manually by visual inspection, in such a way that only the darkest pixels, which correspond to pixels in focus, are accepted as being part of fiber and are set to '1' in the binary image. In this paper, 10% and 20% of the mean intensity are used as threshold values for the analysis of holograms of dry particles and particles in supension, respectively. It should be mentioned that for dry particles with clean background nearly identical results were obtained for threshold values ranging from 5% to 15% of the mean intensity. For particles in suspension, where background is more noisy, the threshold values ranging from 18% to 25% of the mean intensity provided nearly identical results. Figure 5.2(b) shows

an example of the segmented images of reconstructions of a titled fiber obtained at various depths.

5.2.3 Superimposition

After image segmentation, the thresholded reconstructed images are superimposed onto the preceding image and this process is continued until the reconstruction of the whole sample volume is covered. In this way, all the focused parts of a single fiber at different reconstructions are merged together comprising of a full projection of the fiber on a single 2D image plane; see Fig. 5.2(c). The resulting superimposed image is then converted to a binary image. After this process, MATLAB function 'bridge' for morphological operation is performed onto the superimposed binary image to connect the zero valued pixel gap between two nonzero neighbors. After bridging, dilation followed by erosion, is performed to merge the fragmented portions belonging to a particular fiber. In addition, a tailor made collinearity method that compares the slope and proximity of two line segments is used to join broken fibers. In this method, if the difference in slopes of the two line segments is smaller than three degree and the closest distance between any two extremes of the two line segments are less than 15 pixels, the two segments are considered to be parts of a single fiber. Hence, from the superimposed image the projected length of the individual fiber is obtained. It is worth pointing out, unlike 3D point cloud method, all image processing operations are performed on a 2D image plane hence saving the memory and computational load. Finally, all the detected fibers are labeled and the major axis length of the fitted ellipse around the fiber on the 2D image plane is measured. This major axis is then multiplied by a factor of $\frac{\sqrt{3}}{2}$ to obtain the projected lengths [120].

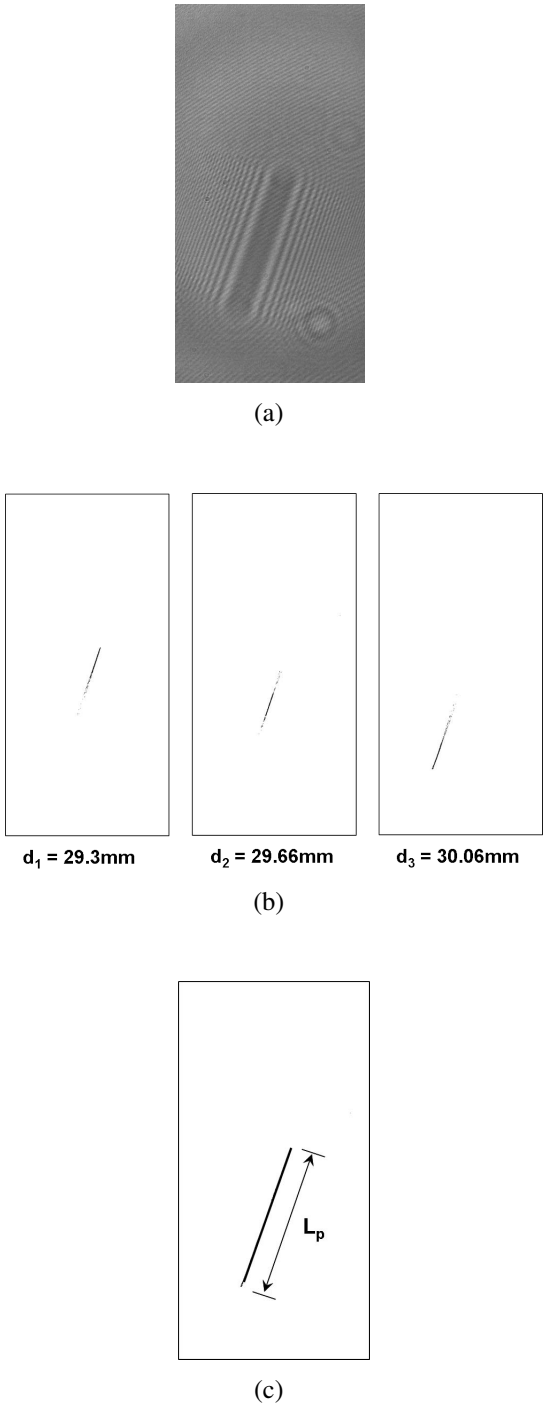

Figure 5.2: Key steps of the superimposition algorithm: (a) Hologram of a fiber of length 1320 μm and off-axis tilt of $50°$; (b) Numerically reconstructed images after applying threshold at different depths; (c) Final superimposed image constituting the projected image of the fiber. L_P refers to projected length of the fiber on the image plane, XY.

5.2.4 Localization of a tilted fiber

After the superimposition step, the projected length of the fiber is known. In order to obtain the real length of fiber, its orientation needs to be measured. The localization step identifies the position of the fiber in the 3D volume and calculates its out-of-plane tilt. For this purpose, the algorithm selects two end regions by sectioning the projected length of the individual fiber into four equal segments; see Fig. 5.3(a). In general, the number of segments can be different from four and should be chosen such that each segment contains at least 15-20 pixels to allow reliable localization of the segment based on intensity variation. It is worth pointing out that the smaller the number of pixels in each segment, the higher the chances of obtaining noisy 'intensity-depth' profile. This can lead to an erroneous measurement of the angle of tilt. The depth profiling is performed by calculating the mean intensity of the two end regions for all reconstruction depths within the volume. In this approach, the two selected end regions are expected to have the minimum mean intensity at their best focused planes. The best focus depths of the two end sections provide the axial locations of their centroids.

The depth profiling for finding focused positions of the two end regions of a single tilted fiber is shown in Fig. 5.3(b). Once the projected length and axial positions of two terminal fragments of a tilted fiber are known, the real length is calculated as

$$\theta = \tan^{-1} \frac{\Delta d}{L_c} \tag{5.1}$$

$$L_R = \frac{L_P}{\cos \theta} \tag{5.2}$$

where θ is the angle of orientation out of the image plane (*i.e.* along YZ plane in Fig. 5.3(a)), Δd is the distance between two axial positions (in Fig. 5.3(a), $\Delta d = d_3 - d_1$ along the optical axis Z) of the terminal fragments of a tilted fiber. L_c, L_P are the centroid to

centroid distance between two terminal sections of the projected fiber and projected length on the image plane, XY, respectively (see Fig. 5.3(a)), while L_R denotes the real length of the fiber. As can be seen from Eqs. 5.1 and 5.2, the measured θ depends on L_c and Δd, which affects the measurement of the real length. It is worth pointing out that if the projected length of a fiber is comparable to the depth-of-focus of the system, it affects the measurement of θ significantly, as the two end positions of the tilted fiber are not clearly distinguishable. This is particularly observed at the large out-of-plane tilts, as the projected length becomes shorter.

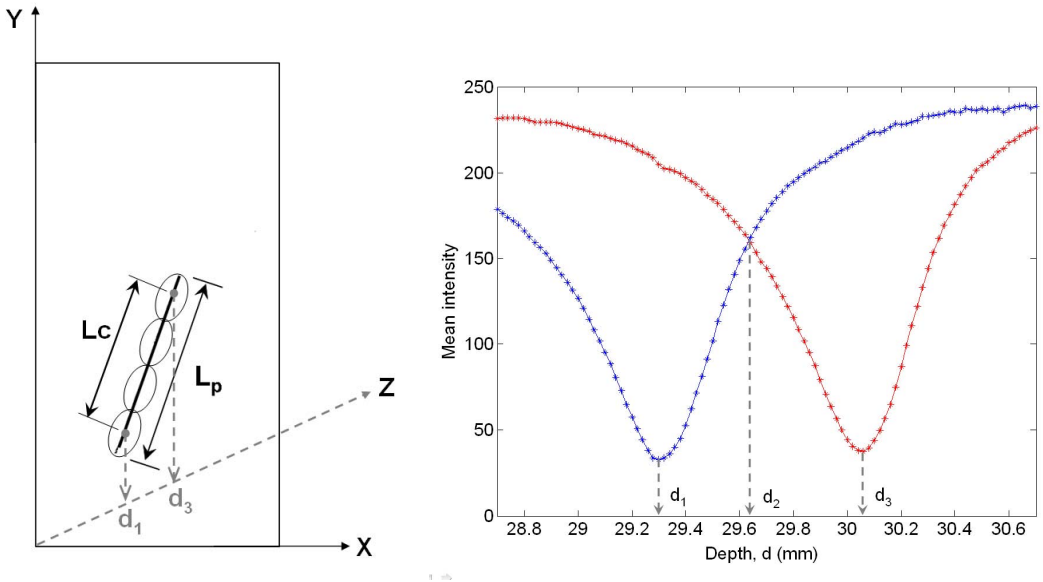

(a) (b)

Figure 5.3: Localization of the $50°$ tilted fiber shown in Fig. 5.2. The fiber is tilted both in XY (image plane) and YZ (out-of-image plane) plane while $\theta = 50°$ corresponds to the tilt along YZ plane: (a) Sectioning of the superimposed fiber for calculating average intensity of the terminal sections; The ellipses indicate four equal sections; (b) Depth profiling of the two terminal sections determining the tilted position of the fiber out of the image plane.

5.3 Experiments and results

The experimental setup used is depicted in Fig. 3.12. In this set-up, a laser source (Lambda Photometrics DPGL3020, Harpenden, UK) with a wavelength of 532 nm is focused on to a 1 μm pinhole which is located at a distance $D = 64$ mm from the CCD camera (The Imaging Source DMK41BF02, Bremen, Germany) with 1280 $\times$ 960 pixels measuring 4.65 $\times$ 4.65 μm each. Two systems, namely a single microfiber placed on a rotating mount and a suspension of microfibers in solution were studied. For microfiber suspension, the experiment was conducted using a cuvette (12.5 mm(L)$\times$12.5 mm(W)$\times$48 mm(H)) containing the suspension of a population of carbon fibers (Asbury PAN type carbon fiber, USA) in water.

5.3.1 Single fiber on a glass slide

In this section, the performance of the superimposition method is compared with the '2D projection algorithm' and the '3D point cloud algorithm'. In order to benchmark the algorithm it is applied to holograms of single fiber of known length and off-axis tilt. For this purpose, the experimental setup shown in Fig. 3.12 was used. In this setup, a single fiber of known length was placed on a glass slide. The glass slide along with the fiber was held by a rotating mount capable of providing a known off-axis tilt. Two fibers with lengths 1320 μm (called long fiber) and 176 μm (called short fiber), were rotated from 0° to 65° tilt at 5° intervals. A hologram was recorded for every tilt and processed for 100 reconstructions using the method described in Section 5.2. From the recorded hologram the projected length, angle of orientation and real length were measured and compared with the known values.

Figure 5.4 shows comparison of the projected lengths measured by the two algorithms, 2D-projection and superimposition method, along with theoretically expected values. For the long fiber the 2D-projection algorithm successfully measures the projected length only

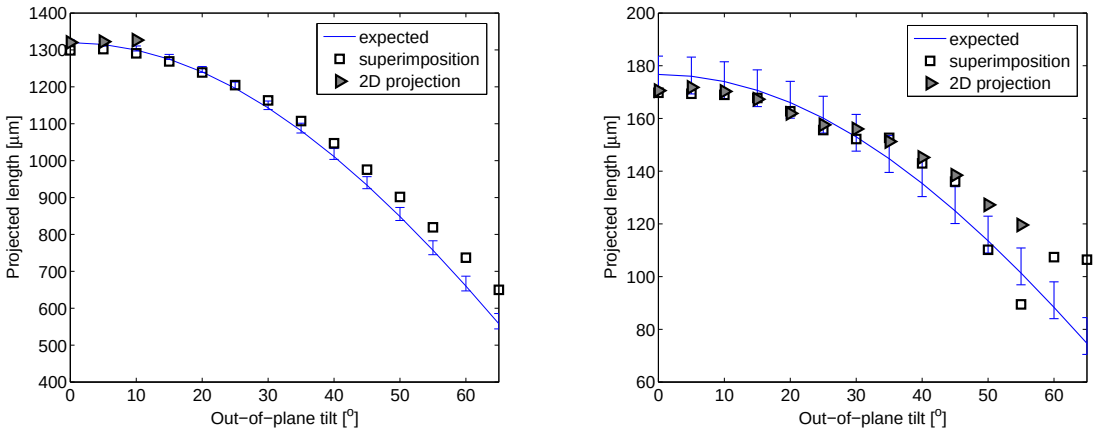

Figure 5.4: Projected length measurements of a single fiber: (a) long fiber (1320 μm); (b) short fiber (176 μm). The error bars are theoretically calculated based on the resolution of the measurement systems.

up to $\theta = 15°$. For $\theta > 15°$, the 2D-projection algorithm fails to detect the fiber; see Chap 3 for details. In comparison, the superimposition algorithm successfully measures the projected length even at high degree tilts. For short fiber both methods yield good measurements of projected lengths up to $55°$ tilt. At tilts larger than $55°$ the 2D-projection failed to detect the fiber while the superimposition algorithm detects the fiber for all tilts; see Fig. 5.4(b). It is worth noting that the projected length of fiber at large tilt becomes comparable to the depth-of-focus, hence, the chances of detecting projected lengths of short fiber at large tilts by 2D projection algorithm increases. In Fig. 5.4(a) and 5.4(b), it is also observed that at tilts above $45°$ projected length is overestimated using both 2D-projection and superimposition methods. This overestimation might occur due to refraction of the laser light by the tilted glass slide.

Figure 5.5 shows the relative error in the measured real length for different out-of-plane tilts using superimposition and 3D point cloud algorithm. As can be seen from Fig. 5.5(a), the superimposition method accurately measures the length of the long fiber over a large range of tilts with relative error less than 4%. Here, the measurement accuracy for both

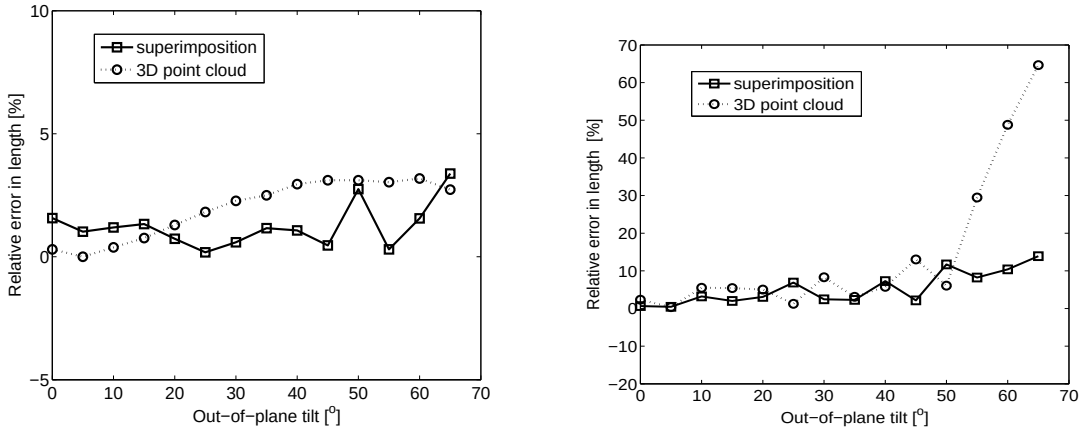

(a) (b)

Figure 5.5: Measurement of the real length of a single fiber: (a) long fiber (1320 μm) and, (b) short fiber (176 μm). Symbols represent the experimental measurements while the lines show the trend.

3D point cloud algorithm and superimposition method are comparable. For the short fiber, the relative error in the measured length is comparable for both superimposition and 3D point cloud method only up to 45° tilt; see Fig. 5.5(b). The maximum error obtained from superimposition method is 13%, while the 3D point cloud method significantly overestimates the length for $\theta > 45^\circ$. In summary, this experiment confirms the accuracy of the superimposition method over 3D point cloud method. Furthermore, the superimposition algorithm requires significantly lower computational time in comparison to the 3D point cloud method. For the holograms of single fiber, the superimposition method usually took only 3 minutes, while the 3D point cloud method took 3 hours to process the same hologram although the number of reconstructions were the same. It is worth noting that, the single fiber experiment is not only tested for fiber length 1320 μm and 176 μm. It is also tested for 512 μm, 253 μm and 150 μm fiber that are not reported here. In all cases, the verification provided excellent performance of the algorithm with almost similar observation with the current analysis.

5.3.2 3D measurements of microfibers in suspension

Next, the method was applied to the population of fibers, a situation encountered in practice. For validation purposes, carbon fibers were placed flat on glass slides and their lengths were measured using a microscope. It was assumed that all fibers were flat and the length measured corresponded to their real lengths. Over 600 microscopy images were acquired and the lengths of identified fibers were measured by image analysis.

For the holographic measurements only the superimposition algorithm is considered as this method yields accurate results for both long and short fiber. Each hologram is reconstructed at 400 image planes covering a depth of 8 mm. The algorithm took approximately 7 minutes to process a single hologram with 400 reconstructed images. A total of 514 holograms of fiber suspension were recorded and analyzed. A sample hologram of fiber suspension, the corresponding superimposed image and 3D distribution of the detected fibers are shown in Figs. 5.6(a), 5.6(b) and 5.6(c), respectively. A sample of the microscopy image is also shown in Fig. 5.6(d).

Figure 5.7 shows the length distribution of fiber population in suspension. To avoid any erroneous measurements at large tilts due to the limitations of DOF, fibers with tilts larger than 60° and lengths smaller than 176 μm are neglected. We have chosen 176 micron as the minimum length, because this value is close to the length of the shortest fiber we have measured on a glass slide accurately. A total of 2338 fibers are identified using holography. The resulting real length distribution of the fiber population obtained by analyzing the holograms is shown in Fig. 5.7(a). The distribution of real lengths obtained from the microscopy images of the same fiber population is also shown in Fig. 5.7(a). For a fair comparison, we have only considered fibers with length larger than 176 μm from the microscopy data. As can be seen from Fig. 5.7(a), projected length distribution obtained using holography is shifted to the left from the real length distribution obtained using microscopy measurements, while the real length distribution obtained by incorporating the

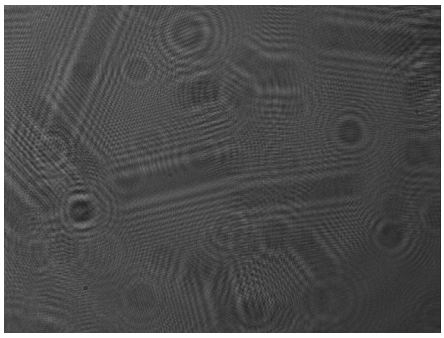

(a)

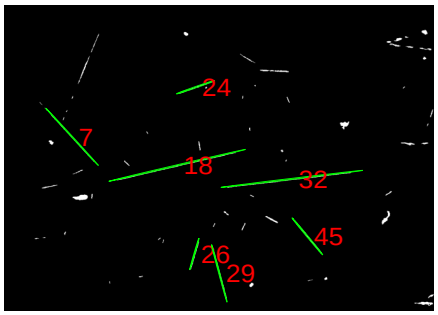

(b)

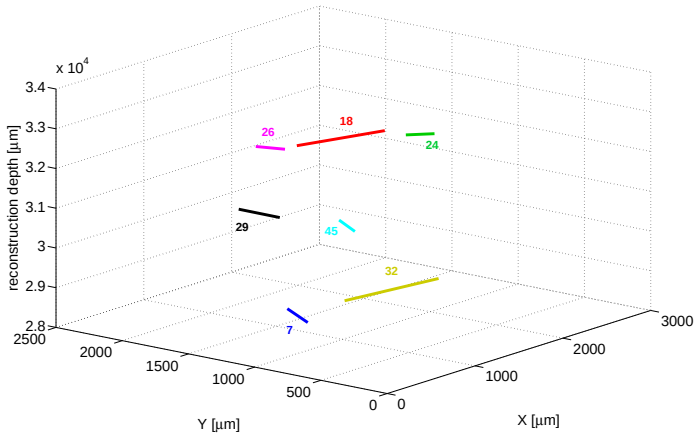

(c)

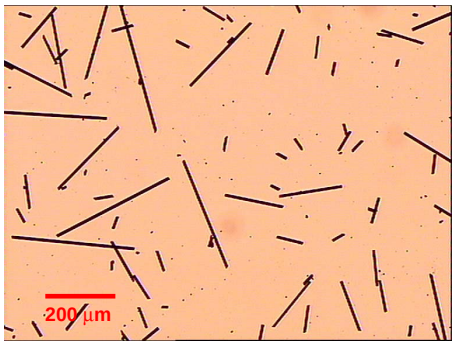

(d)

Figure 5.6: Digital holography data of microfiber suspension: (a) A sample hologram of fiber suspension in a cuvette; (b) The corresponding superimposed image of the reconstructions. Numbers indicated represent the index of individual fiber detected finally from the hologram; (c) 3D distribution of identified fibers showing their orientations and lengths; (d) Sample microscopy image of same fiber population on a glass slide.

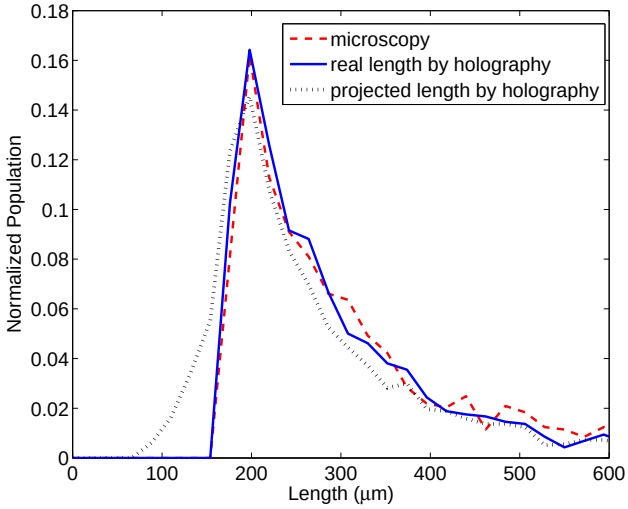

(a)

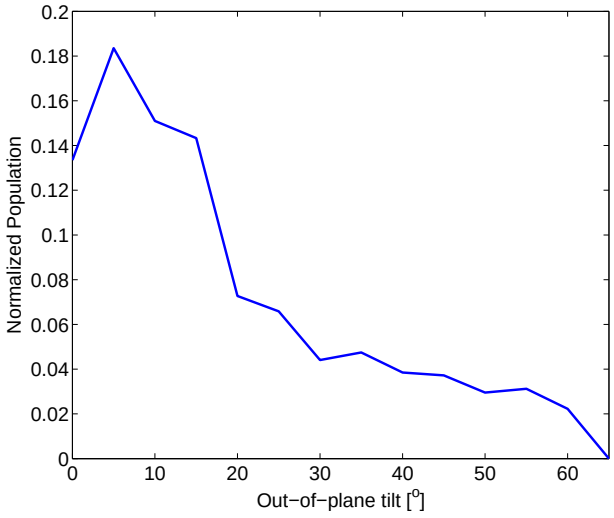

(b)

Figure 5.7: Characterization of fibers in suspension:(a) length distribution of fiber population in suspension (for fibers longer than 176 μm); Dotted line represents the projected length distribution directly obtained by holography without incorporating the angle of orientation in suspension; (b) Corresponding angle distribution of the fiber population in suspension.

angle of orientation in holography measurement matches very well with the microscopy measurements.

The corresponding distribution of angle of orientation of the fiber population is shown in Fig. 5.7(b). As no tools are available for measuring the true tilt distribution of the population of particles, the accuracy of the measured tilt distribution cannot be verified. However, a few observations can be made. Firstly, the fibers show a range of orientation. Secondly, most of the fibers in this experiment have tilts less than 20° and there seems to be a preferred orientation for this system. This underlines the fact that the orientations of fibers depend on the particular system that is being investigated. Hence, the assumption of equal probabilities for all orientations, which is a frequently used assumption for the 2D inversion techniques [95, 133], is not necessarily valid.

5.4 Chapter summary

In this chapter, a novel method, namely, 'superimposition algorithm', for the measurement of length, position and off-axis tilt of needle like particles with no a priori information about the orientation of particles, has been developed. The method was validated using fibers of known length and orientation. The method was successfully applied to the population of fibers suspension to measure real length distribution from the measured projected lengths and their angle of orientation in the 3D volume. The obtained real length distribution showed good agreement with those obtained from microscopy measurements. The method has distinct advantage over '2D projection algorithm' and '3D point cloud method'. Firstly, the method is able to measure the projected lengths with added advantage of measuring angle of orientation of needle shaped particles in volume. Secondly, the method has increased accuracy to measure the real lengths of short fibers with substantial reduction in computational load. The successful application of the new method on the volume of fiber suspension clearly demonstrates its applicability as a novel tool for 3D analysis of needle

shaped particles. However the applicability of the method has only been demonstrated for fiber sizes larger than 176 micron. As with the decrease in fiber length, the measurement of tilts greatly depends on the system depth-of-focus, it requires further investigation for measuring fibers with lengths smaller than 176 μm.

Chapter 6

On-line monitoring of crystallization processes

6.1 Introduction

This chapter presents the experimental study of measuring transparent crystals using the digital holography based measurement method. As a test system, batch cooling crystallization of oxalic acid in water is studied. Oxalic acid can be crystallized with two different shapes when the supersaturated solution is cooled at two different rates during the crystallization process [134]. Figures 6.1(a) and 6.1(b) show two different morphology of the crystals, rectangular prism and needle shape, with step cooling ($\approx$40°C/hr) and shock cooling ($\approx$120°C/hr) rates, respectively.

In this study, only step cooling crystallization is used to produce rectangular prism shaped crystals. The following section describes the experimental protocol adopted in the study; measurement of crystal characteristics, *i.e.*, PSD, ALD and comparison with microscopy data. The second half of this chapter demonstrates the use of digital holography to obtain in-line, real-time measurements of growth of the crystals.

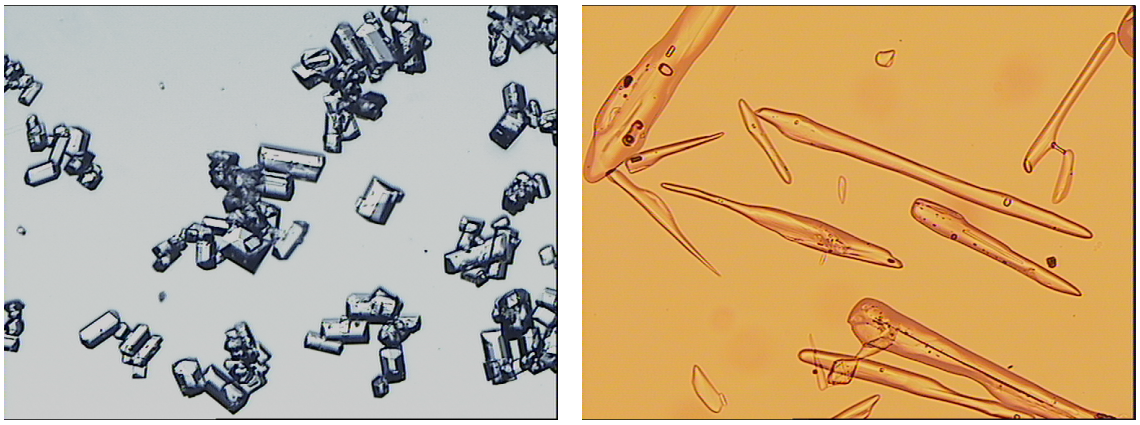

(a) (b)

Figure 6.1: Microscopy image of oxalic acid crystals produced from cooling crystallization: (a) Rectangular prism shape crystals produced by cooling from 40° to 24°C at a rate, $\approx 40°C/hr$; (b) Needle shape crystals produced by cooling from 40° to 10°C at shock cooling rate, $\approx 120°C/hr$.

6.2 Crystallization of oxalic acid

6.2.1 Crystallizer set-up

The crystallization set-up, shown in Fig. 6.2 was equipped with a jacketed 500 mL borosilicate glass reactor with an inner diameter of 80 mm (Kimble Chase-Kontes, USA). The reactor was placed on top of a magnetic stirrer and a stir bar of size 2.5 cm was used for stirring the solution. The stirrer was operated at approximately 300 rpm. The temperature of the reactor was controlled using NESLAB RTE10 thermostat (Thermo Fisher Scientific, Newington, NH). Figure 6.2(b) shows the schematic of the setup for on-line imaging of crystals using digital holography. For the flow-through-system, a quartz flow-cell with dimension of 12.5 mm(L)$\times$12.5 mm(W)$\times$65 mm(H) was equipped with a peristaltic pump (Gardner Denver Welch Vacuum, USA) for circulating the solution at a flow rate of 250 mL/min. Alternately, the flow-cell can be replaced with a quartz cuvette for off-line analysis, when on-line imaging is not required.

For recording of digital hologram of the crystals in solution, a laser (Lambda

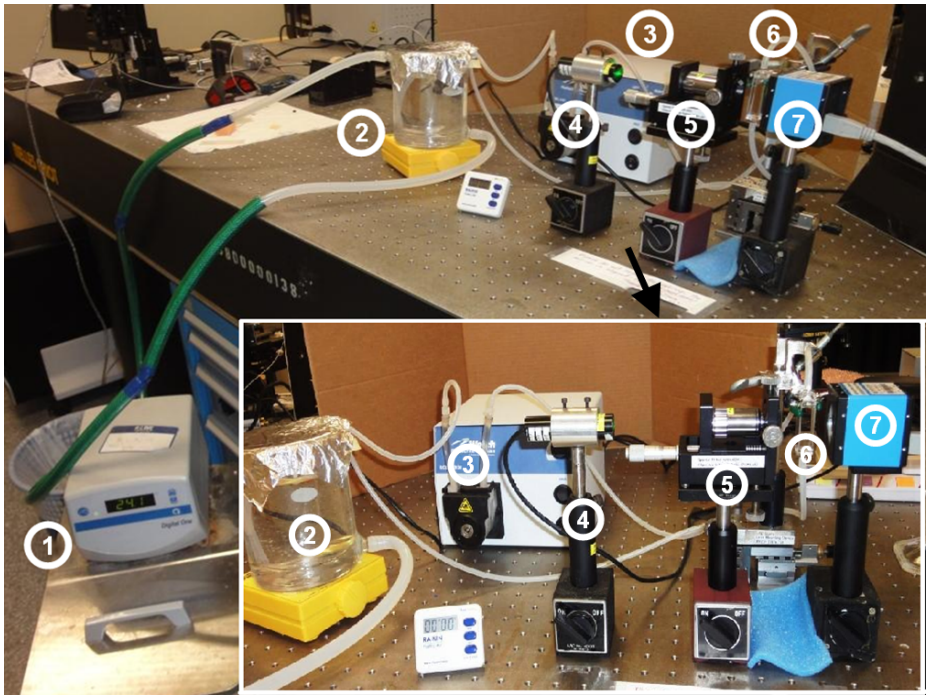

(a)

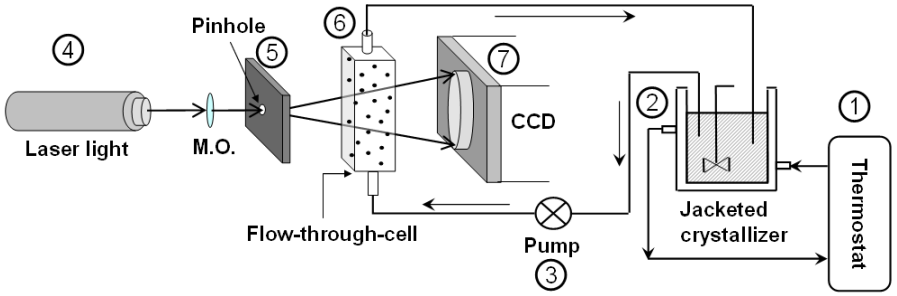

(b)

Figure 6.2: Set-up for on-line imaging of crystallization using digital holography: (a) Experimental set-up for oxalic acid crystallization. Inset shows the zoomed view of the digital holography set-up with flow-cell; (b) Schematic of the set-up. 1. Thermostat; 2. Jacketed reactor placed on a magnetic stirrer; 3. Liquid circulating pump; 4. Laser; 5. Pinhole; 6. Flow-cell and 7. Imaging device, CCD.

Photometrics DPGL3020, Harpenden, UK) with wavelength, λ=532 nm and a CCD (The Imaging Source DMK41BF02, Bremen, Germany, 1280$\times$960 pixels, 4.65$\times$4.65 μm pixel size) were used. Laser light was focused on to 1μm pinhole by a 60$\times$ microscope objective lens. The CCD was positioned 60.5 mm from the pinhole. Sample was placed in between pinhole and CCD to record the hologram.

6.2.2 Materials and methods

To carry out the experiment, a solution was prepared with 51 g of oxalic acid dihydrate (purity $>$ 99%, Sigma Aldrich) in 350 mL of fresh distilled water (saturation temperature 27°C). The solution was then heated to 40°C and the crystallizer was held at that temperature for $\approx$ 1 hr. This ensured the complete dissolution of oxalic acid solids into the solution (c.f. the solubility curve shown in Fig. 6.3). The solution was then cooled to 24°C at a cooling rate of $\approx$0.7°C/min. At this cooling rate rectangular shaped crystals are expected to be crystallized out.

6.3 Measurements of crystals

In this section, measurement of transparent crystals using digital holography is validated with those obtained from microscopy. For this purpose, a portion of crystals produced in solution was withdrawn using a disposable dropper. Care was taken to remove the sample as soon as they are visually discernible. This procedure was adopted so as to prevent the sampling of agglomerates which are likely to form at high solid concentrations. The samples were filtered and dried at room temperature.

To perform microscopy measurements, dried crystals were sprinkled on microscopy glass slide and placed under the microscope to capture the images. In this manner, a total 409 microscopy images of crystals samples were captured and analyzed using edge

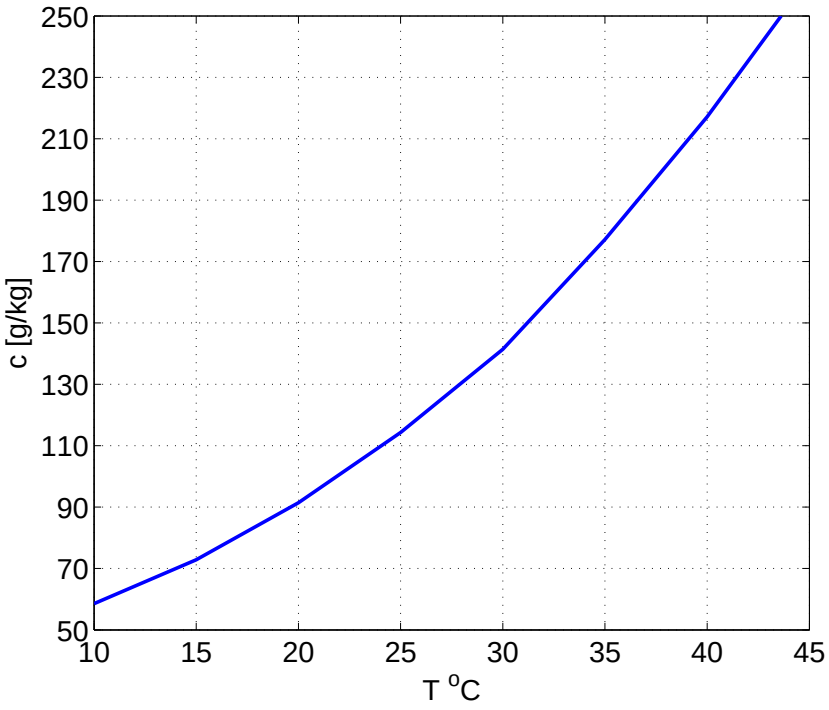

Figure 6.3: Solubility curve for oxalic acid crystals in water [1]. 'c' denotes the solubility of oxalic acid crystals in g of solute/ kg of solution and 'T' denotes the temperature.

detection based image analysis. A total of 1041 crystals were identified and the crystal size distribution (CSD) of the sample population was obtained.

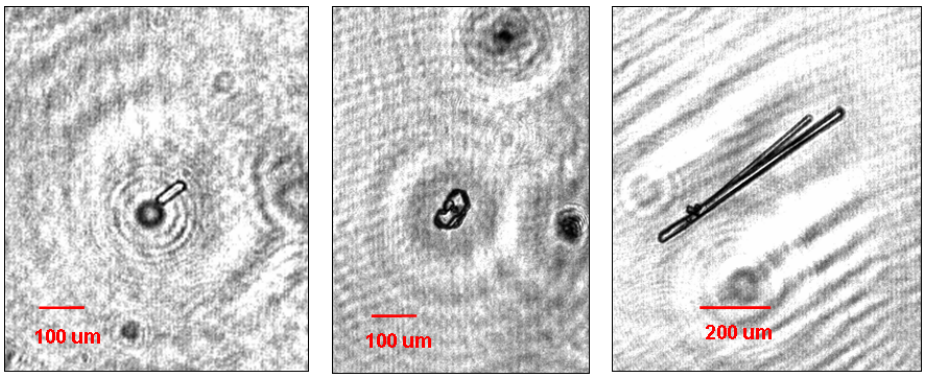

Figure 6.4: Example of some zoomed portion of reconstructed images showing focused transparent crystals appeared at different holograms of oxalic acid suspension.

While measuring the CSD of crystals placed on a glass slide using digital holography is expected to be straightforward, our aim was to measure them in solution. To perform the digital holography measurement, crystals on the glass slides were transferred to a 3.5 mL capacity quartz cuvette ($12.5\ \mathrm{mm(L)} \times 12.5\ \mathrm{mm(W)} \times 48\ \mathrm{mm(H)}$) filled with saturated solution of oxalic acid at room temperature. Once the crystals were transferred, the holographic measurements were made without much delay in order to avoid the growth of the crystals. A total of 197 holograms of oxalic acid crystal suspension were recorded and processed using superimposition method described in Chapter 5 yielding 4088 crystals. Figure 6.4 shows some reconstructed images of different holograms of oxalic acid suspension showing focused transparent crystals. It is important to note that reconstructions of the holograms reveal the transparent character of the oxalic acid crystals which are clearly evident from the microscopy images. However, it is also seen that the edges of the crystals have dark edges making them amenable to image segmentation.

Figures 6.5(a) and 6.5(b) show a hologram of suspension of oxalic acid crystals and a reconstructed image of the hologram at a particular plane, respectively. The corresponding superimposed image is shown in Fig. 6.5(c), which was obtained by reconstructing the

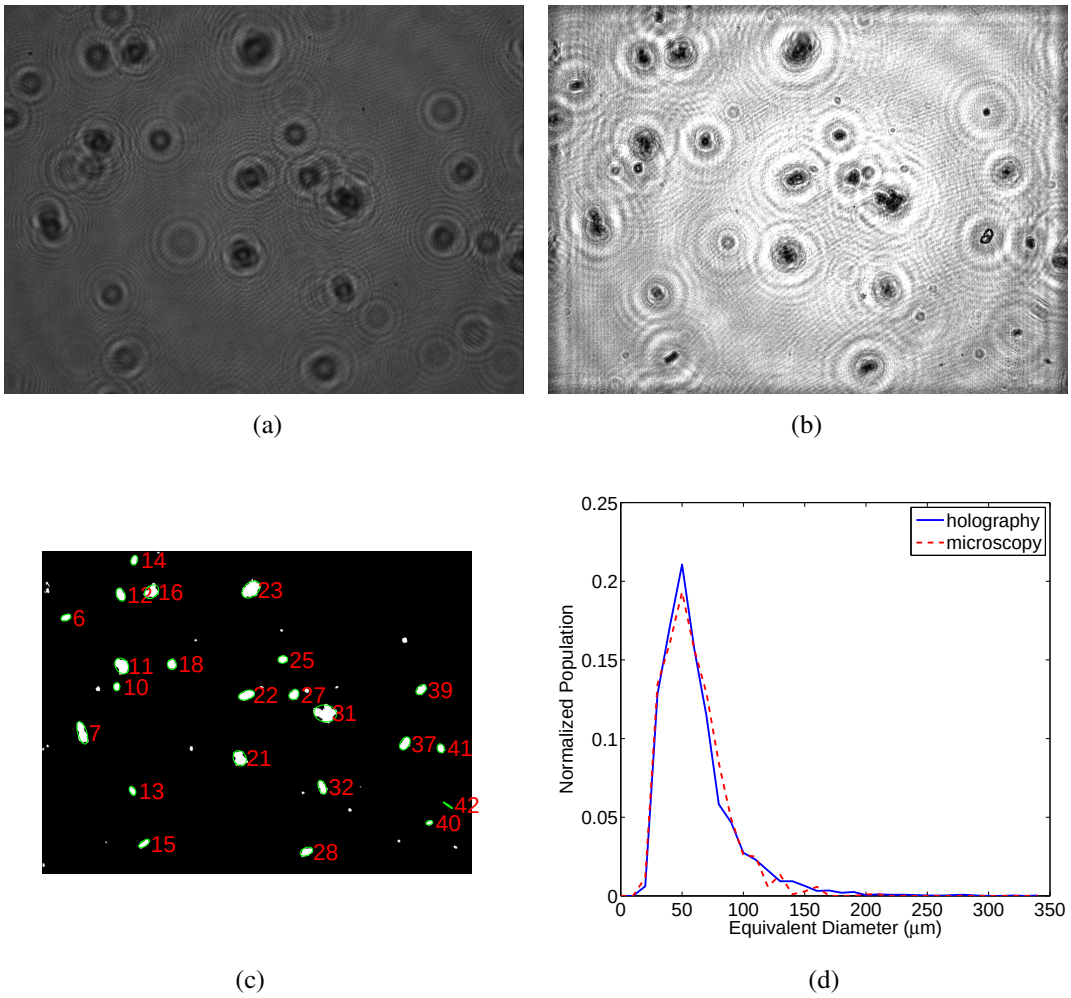

Figure 6.5: Digital holography data of oxalic acid crystals in solution: (a) Hologram of oxalic acid crystals in saturated solution; (b) example of a reconstructed image; and (c) Corresponding superimposed image. Numbers indicated represent the index of individual particle detected in that hologram; (d) Equivalent diameter distribution of population of oxalic acid crystals in saturated solution.

hologram using 400 steps covering a volume of 8 mm depth. The final CSDs of oxalic acid crystals obtained by analyzing all the microscopy images and recorded holograms are shown in Fig. 6.5(d). The comparison showed excellent match between the measurements from two methods. It is worth pointing out that only projected lengths of crystals were considered using superimposition method in holography based measurements. Orientation of crystals in the volume were neglected here, as the crystals were assumed to have low aspect ratio, thereby having less impact of the orientation on the size measurements.

Figures 6.6(a) and 6.6(b) show axis length distribution of population of transparent oxalic acid crystals measured by microscopy and holography, respectively. As can be seen from Fig. 6.6(a), the major and minor axis lengths for most of the crystals are comparable, *i.e.* aspect ratio is close to 1. Presence of some crystals with aspect ratio slightly higher than 1 can be attributed to the presence of crystals that have one characteristics length slightly longer than the others, *e.g.*, rectangular shaped crystals. Microscopy image shown in the inset of Fig. 6.6(a) also confirms the presence of such crystals. Almost similar results are observed from ALD measured by holography based method as shown in Fig. 6.6(b). Here, presence of some crystals in the size range of $\approx$ 100-150μm length with the width of $\approx$ 8-25μm range is also observed. The inset images in Fig. 6.6(b) display the reconstructed images of a hologram at two distances confirming the presence of needle like crystals in the crystal suspension. It is worth pointing out that dried crystals were measured by microscopy while the crystals measured by holography were suspended in saturated solution. Hence, oxalic acid crystals possibly started growing with time in the solution, preferentially in one dimension. Thus small percentage of needle like crystal were observed in holography measurement while they were absent in the microscopy measurements.

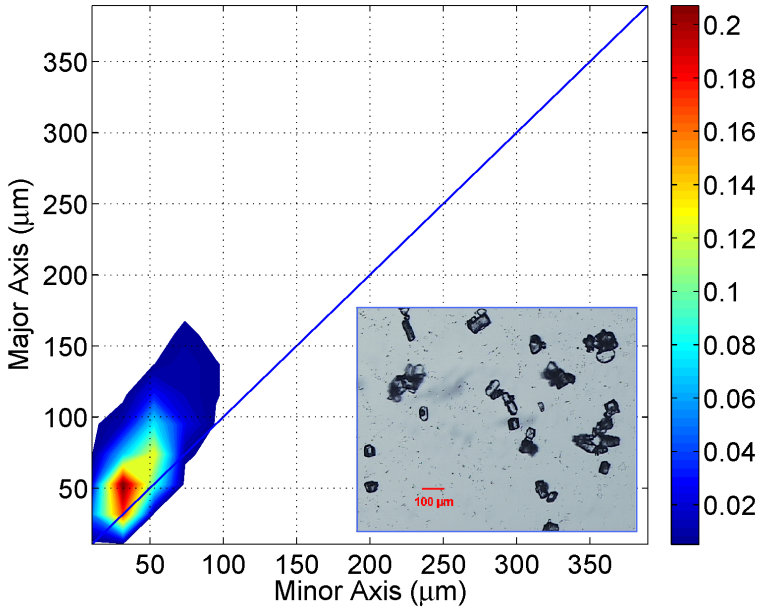

(a)

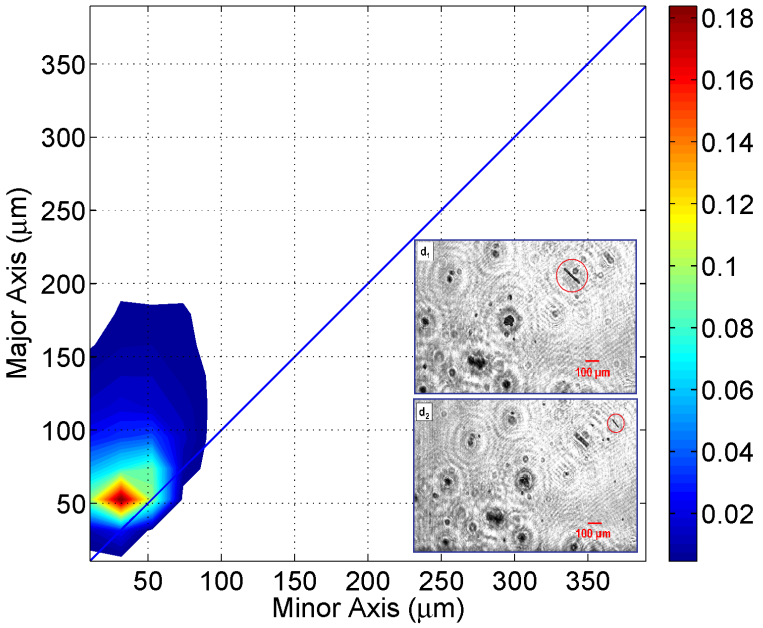

(b)

Figure 6.6: Axis length distribution of Oxalic acid crystals produced from cooling crystallization: (a) ALD obtained by microscopy. Inset microscopy image of dried crystals confirms the shape characteristics; (b) ALD obtained by holography. Reconstructed image at two different distance are displayed in the inset confirming the presence of rod like crystals in solution. Circle encloses rod like crystals.

6.4 Monitoring growth of crystals

In this section, the feasibility of estimating the growth rates of oxalic acid crystals using on-line digital holography system is demonstrated. For this purpose, the holographic microscopy set-up with flow-through-cell shown in Fig. 6.2(a) was used. The details of the set-up and experimental procedure are discussed in Section 6.2. The solution of oxalic acid crystals was continuously circulated by the pump. The exposure time of the camera was set to 170.3 μsec in order to avoid the motion blur in the recorded holograms. Holograms were acquired at 2 second interval to capture the onset of crystal appearance and to monitor the growth of crystals in the solution during crystallization process. Starting at 40°C, image acquisition continued until the temperature of the crystallizer reached 24°C. Evolution of crystal size with time was measured by processing each hologram using the superimposition method by reconstructing 400 steps covering a volume with depth 8 mm.

Figure 6.7 shows the mean size of oxalic acid crystals measured by digital holography in 24 second time. Each point in the plot represents the average equivalent diameter obtained from all detected crystals from a single hologram captured in 2 sec time intervals. The starting point (t = 0) indicates the onset of crystal appearance in the solution. From the onset of crystal appearance, the evolution of crystal size with time can be illustrated from Fig. 6.7. As can be seen, at the onset, average size is 15μm, while the mean size grows to 31 μm in 24 second time showing a rapid growth in the system. Figures 6.8(a), 6.8(b) and 6.8(c), show the example of reconstructed images of hologram captured at t = 0 s, t= 4 s and t = 12 s, respectively. The focused crystals appeared at different time in the reconstructed images provide the visual confirmation of the growth of oxalic acid crystals in the system. This qualitative study demonstrates the applicability of digital holography technique to monitor the growth of crystals in crystallization process. It is worth pointing out that for time longer than 24 second, the solid concentration became so high that it prevented the reference beam from being transmitted properly through the system. Hence

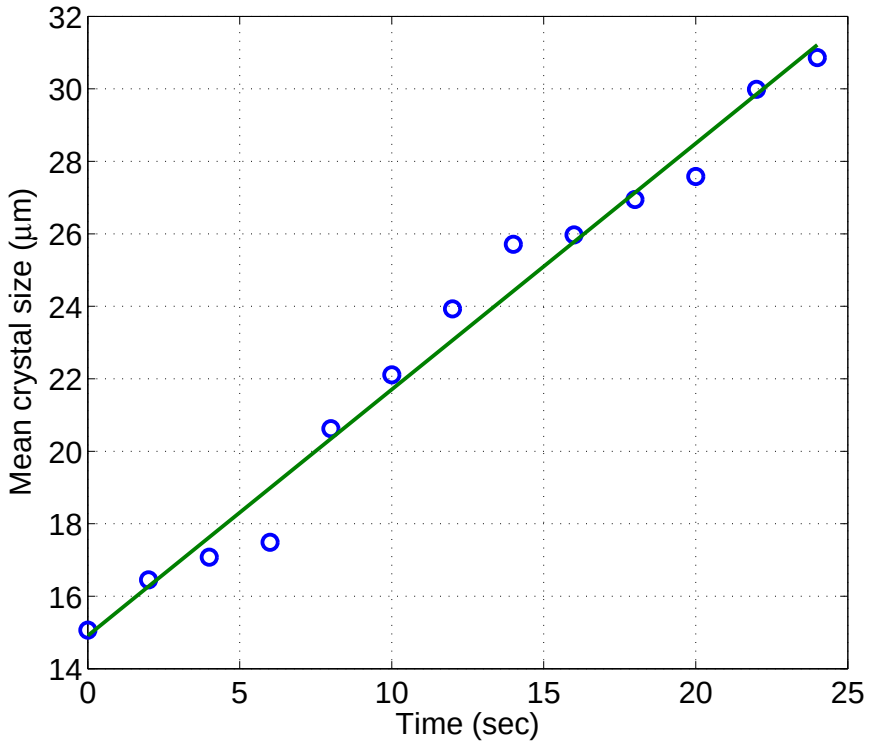

Figure 6.7: Growth of oxalic acid crystals in 24 second time period. Each point represents mean equivalent diameter of detected crystals obtained by processing single hologram recorded at that particular time. The time, t=0 corresponds to the onset of crystal appearance in the hologram.

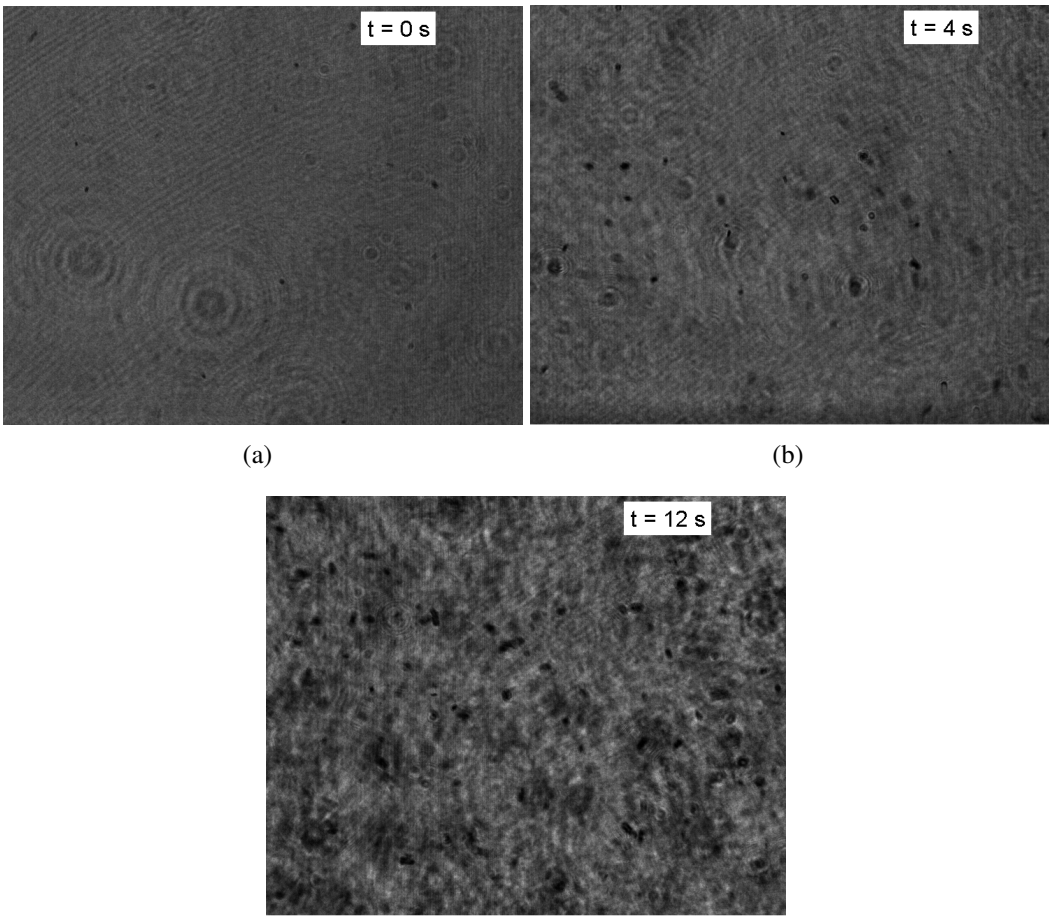

Figure 6.8: Example of reconstructed image of hologram captured at different times: (a) reconstructed image at d = 25.06 mm of a hologram captured at t = 0 s; (b) reconstructed image at d = 31.2 mm of a hologram captured at t = 4 s; (c) reconstructed image d = 24.66 mm of a hologram captured at t = 12 s.

difficulties were encountered in acquiring good holograms. It is worth pointing out that the problem with high solid concentration is inherent for all transmission based imaging system [129], where difficulties were faced in image analysis for improper light contrast due to high slid concentration. For this purpose, dilution step is required for capturing images to make use of transmission based imaging technique [129].

6.5 Chapter summary

In this chapter, the use of digital holography has been explored for the measurement of transparent crystals in solution and for monitoring real time growth of crystals in crystallization processes. The digital holography based method successfully identified transparent crystals from solution and measured their size using superimposition algorithm described in previous chapter. The measurement of crystals was validated with those obtained by microscopy. Further, the use of digital holography has been demonstrated for the measurement of growth of oxalic acid crystals in the crystallization process. This study reveals promising possibilities for potential use of digital holography as novel tool, which has several distinct advantages over conventional photography technique for on-line monitoring of crystallization process.

Chapter 7

Conclusions and future work

7.1 Conclusions

This work mainly contributed to the development of on-line particle size and shape measurement tool which is based on the digital in-line holography technique. Several automated image analysis algorithms are developed for extracting particle size and shape from numerically reconstructed images of a hologram at different plane of focus. The developed methods are benchmarked for different size of particles spanning a range of 10-1000μm with different shape characteristics.

First, an algorithm is presented for digital holography based particle measurement which is based on the analysis of the projections of particles in the camera plane. The method used Canny edge detection for the segmentation of particles from the reconstructed images and a localization algorithm is coupled with the segmentation method for identifying the best focusing depth of a particle. Localization of the particles was verified with known position of the particles. The method was applied to the experimentally recorded holograms of spheres, elliptical beads and needle shaped fibers with different physical state, *e.g.*, static, suspended and flowing conditions. Holograms analyzed using the algorithm to measure 1D equivalent diameter of spheres and 2D measurement (projected length and width) of

elliptical to needle shaped particles. The measurement from each experiment was verified either by those measured by independent technique or by certified known sizes and shapes showing good performance and measurement accuracy of the method. At the end of this stage, limitation of the projection based algorithm for extremely non-spherical particles that were oriented randomly were highlighted. Measurement of single fiber of known out-of-plane tilts verified that, size measured by 2D projection algorithm underestimate the real length significantly. Further, by using a microscope objective, the potential of digital holography to accurately measure the size of near micron particles was also investigated.

In the second step, the work focused on to solve the limitation of the projection algorithm for randomly oriented non-spherical particles. A novel combination of automated image analysis and statistical techniques applied on the intensity of reconstructed digital holograms was used to accurately determine the characteristics of the micro-fibers. The image analysis used a stringent threshold for particle segmentation and segmented pixels clouds correspond to the particles obtained at each reconstruction depth were stored in a 3D matrix. The line fitted to the pixel clouds correspond to the individual fiber yielded size, position and orientation of microfiber without no *a priori* knowledge of size, position and orientation. The potential of the 3D point cloud method was validated using single fibers of known sizes and orientations and subsequently demonstrated using a suspension of fibers. Nevertheless, the method has distinct advantages over projection algorithm, it suffers from excessive computational load and the statistical method applied to the 3D pixel clouds does not work reliably for the measurement of short fiber.

As an improvement of the 3D point cloud method, an alternate method, namely 'superimposition' method, to measure size, orientation, and position of micro-fiber was developed. As compared to the previous method, the improved method provides reliable measurement of size, tilt and position of microfibers for a large range (176-1200μm) of lengths. In addition, the method is simpler and computationally less intensive compared to

the previous methods. The performance of the method over previous 2D projection and 3D point cloud methods was verified using single fibers of known lengths and tilts. Further, the method was used to measure the population of microfibers in solution. The measurement accuracy was verified with those obtained by microscopy and showed good agreement with each other.

Lastly, the use of digital holography based measurement was investigated for the measurement of characteristics (*e.g.*, PSD, ALD) of transparent crystals in solution. The superimposition method was applied for the measurement of population of transparent crystals in solution. The verification of the measured PSD and ALD by digital holography based measurement showed excellent agreement with those measured by microscopy. Further, the use of digital holography based method was demonstrated for measuring on-line growth of oxalic acid crystals in the crystallization processes. This proof of concept study for on-line growth of crystals opens up promising possibilities in the field of crystallization processes where on-line size and shape measurement of the crystals is of great requirement for controlling product quality.

7.2 Future directions

Measurement of sub-mircon particles In Chapter 3, preliminary studies on the use of microscope objective showed that digital holography has the potential to measure near-micron particles. In several applications there is a strong interest in measuring sub-micron particles. This is an area which is worth investigating in the future. While achieving near micron resolution is still possible using simple lasers, measuring sub-micron particles can be a challenge owing to the limit of diffraction of lasers with wavelengths in the range of visible light. Using lasers with wavelength in the ultra-violet region can be a possibility to overcome this challenge.

Study with high suspension density system In this work we benchmarked the system for relatively low suspension density, as the digital in-line holography set-up we used was transmission based, *i.e.*, the light must transmit through the sample. It is challenging to obtain reliable holograms for solutions with high suspension density or turbid samples. In future, it is required to check the performance of the system for maximum suspension density and turbidity that it can handle. One possible way to handle high suspension density is the use of flow-through-system, which could be modified either by incorporating a dilution system into the circulation loop or reducing the optical path length of the flow-cell. Another possible alternative to the transmission based holography is the reflection based digital holography which might overcome the problem. In future, the reflection based holography set-up for handling high suspension density could be addressed.

Extensive investigation of dynamic growth of crystals and inference of 3D shape of crystals The current study of the measurement of crystal growth has only proved the potentiality of digital holography based measurement in the field of crystallization processes. Further investigation in measuring dynamic growth of crystals considering controlled operating conditions is greatly required, as several issues such as transformation of polymorphic form of crystals, high suspension density, turbidity and inference of 3D shape of crystals need to be explored while dealing with crystallization processes. Although we developed tool for measuring 3D characteristics of needle like particles, inference of complex 3D shape is still need to be addressed in future. The phase information of digital holography could be a possible way to extract the 3D shape of transparent crystals.

Bibliography

[1] W. Omar and J. Ulrich. Solid liquid equilibrium, metastable zone, and nucleation parameters of the oxalic acid-water system. *Crystal Growth and Design*, 6(8):1927–1930, 2006.

[2] N. Variankaval, A. S. Cote, and M. F. Doherty. From form to function: Crystallization of active pharmaceutical ingredients. *AIChE J.*, 54(7):1682–1688, 2008.

[3] J. W. Mullin. *Crystallization*. Butterworth-Heinemann, Oxford, UK, 2001.

[4] P. A. Larsen, P. A. Larsen, D. B. Patience, and J. B. Rawlings. Industrial crystallization process control. *Control Systems Magazine, IEEE*, 26(4):70–80, 2006.

[5] H. Connell, J. Zhu, and A. Bassi. Effect of particle shape on crossflow filtration flux. *J. Membr. Sci.*, 153(1):121–139, 1999.

[6] B. Benli Gnl, zcan, B. McEnaney J. Rouquerol F. Rodriguez-Reinoso, and K. Unger. The effect of particle shape on the filtration rate and shear strength of quartz and dolomite mineral filter cakes. In *Studies in Surface Science and Catalysis*, volume Volume 144, pages 315–322. Elsevier, 2002.

[7] L. X. Liu, I. Marziano, A. C. Bentham, J. D. Litster, E.T.White, and T. Howes. Effect of particle properties on the flowability of ibuprofen powders. *Int. J. Pharm.*, 362(1-2):109–117, 2008.

[8] D. Winn and M. F. Doherty. Modeling crystal shapes of organic materials grown from solution. *AIChE J.*, 46(7):1348–1363, 2000.

[9] P. Barrett, B. Smith, J. Worlitschek, V. Bracken, B. O'Sullivan, and D. O'Grady. A review of the use of process analytical technology for the understanding and optimization of production batch crystallization processes. *Org. Process Res. Dev.*, 9(3):348–355, 2005.

[10] A. Blasco. On-line particle size analysis for process control. *Cem. Int.*, 7(1):86–89, 2009.

[11] M. Dietrich. Ceramic manufacturing overview. In *Bioceramics and Alternative Bearings in Joint Arthroplasty*, Ceramics in Orthopaedics, pages 169–173. Steinkopff, 2005.

[12] D. Pugh and J. Scotland. Particle size analysis for process control process control. *American Ceramic Society Bulletin*, 86(7):30–32, 2007.

[13] O. H. Ahmed, N. M. A. Majid, and M. B. Jalloh. Effect of grain size on selected physico-chemical properties of clay. *Am. J. Environ. Sci.*, 5(5):610–612, 2009.

[14] M. Brni, I. Brada, B. Tripalo, D. Jeek, V. Obradovi, S. Karlovi, and T. Bosiljkov. Ultrasonically improved sieving of food materials for manufacturing of direct expanded extrudates. *Agric. Consp. Sci*, 74(3):149–153, 2009.

[15] J. V. Koleske. Paint and coating testing manual (14th edition): (mnl 17), 1995.

[16] E. J. Hukkanen and R. D. Braatz. Measurement of particle size distribution in suspension polymerization using in situ laser backscattering. *Sens. Actuators, B*, 96(1-2):451–459, 2003.

[17] V. G. Gomes. Advanced monitoring and control of multi-monomer system in emulsion polymerization. *Macromolecular Reaction Engineering*, 4(11-12):672–681.

[18] O. Kammona, E. G. Chatzi, and C. Kiparissides. Recent developments in hardware sensors for the on-line monitoring of polymerization reactions. *J. Macromol. Sci., Rev. Macromol. Chem. Phys.*, 39(1):57–134, 1999.

[19] E. J. Hukkanen and R. D. Braatz. Identification of particle-particle interactions in suspension polymerization reactors. In *Proceedings of the American Control Conference*, volume 2, pages 925–930, 2005.

[20] G. Polacco, C. Basile, M. Palla, and D. Semino. Simple technique for measuring particle size distributions during suspension polymerization. *Polym. J.*, 32(8):688–693, 2000.

[21] M. Belhabri, J. Legrand, N. Le Sauze, and A. Arhaliass. On-line determination of particle size distributions in flowing dispersions. *Part. Part. Syst. Char.*, 21(5):365–371, 2004.

[22] J. Gantt and E. Gatzke. Control of a granulation process using a nonlinear MPC formulation. In *Proceedings of the American Control Conference*, volume 5, pages 4231–4236, 2004.

[23] J. Huang, G. Kaul, J. Utz, P. Hernandez, V. Wong, D. Bradley, A. Nagi, and D. O'Grady. A PAT approach to improve process understanding of high shear wet

granulation through in-line particle measurement using FBRM C35. *J. Pharm. Sci.*, 99(7):3205–3212, 2010.

[24] V. Liotta and V. Sabesan. Monitoring and feedback control of supersaturation using ATR-FTIR to produce an active pharmaceutical ingredient of a desired crystal size. *Org. Process Res. Dev.*, 8(3):488–494, 2004.

[25] J. B. Rawlings, S. M. Miller, and W. R. Witkowski. Model identification and control of solution crystallization processes: A review. *Industrial and Engineering Chemistry Research*, 32(7):1275–1296, 1993.

[26] L. L. Simon, K. Abbou Oucherif, Z. K. Nagy, and K. Hungerbuhler. Bulk video imaging based multivariate image analysis, process control chart and acoustic signal assisted nucleation detection. *Chem. Eng. Sci.*, 65(17):4983–4995, 2010.

[27] L. L. Simon, Z. K. Nagy, and K. Hungerbuhler. Comparison of external bulk video imaging with focused beam reflectance measurement and ultra-violet visible spectroscopy for metastable zone identification in food and pharmaceutical crystallization processes. *Chem. Eng. Sci.*, 64(14):3344–3351, 2009.

[28] J. Lu and S. Rohani. Polymorphism and crystallization of active pharmaceutical ingredients (apis). *Current Medicinal Chemistry*, 16:884–905, 2009.

[29] A. Shukla, A. Prakash, and S. Rohani. Particles settling studies using ultrasonic techniques. *Powder Technol.*, 177(2):102–111, 2007.

[30] B. De Clercq, P. A. Lant, and P. A. Vanrolleghem. Focused beam reflectance technique for in situ particle sizing in wastewater treatment settling tanks. *J. Chem. Technol. Biotechnol.*, 79(6):610–618, 2004.

[31] J. Chen, S. Chen, M. M. Altunbay, and E. Tyurin. A new method of grain size determination for sand-control completion applications. In *Proceedings - SPE*

International Symposium on Formation Damage Control, volume 2, pages 683–692, 2010.

[32] M. Byrne, A. Slayter, and P. McCurdy. Improved selection criteria for sand control - when are ”fines” fines? In *Proceedings - SPE International Symposium on Formation Damage Control*, volume 2, pages 755–768, 2010.

[33] T. Narvanen, T. Lipsanen, O. Antikainen, H. Raikkonen, and J. Yliruusi. Controlling granule size by granulation liquid feed pulsing. *International Journal of Pharmaceutics*, 357(1-2):132–138, 2008.

[34] A. M. Juppo, J. Yliruusi, L. Kervinen, and P. Strom. Determination of size distribution of lactose, glucose and mannitol granules by sieve analysis and laser diffractometry. *International Journal of Pharmaceutics*, 88(1-3):141–149, 1992.

[35] V. S. P. Bitra, R. Alvin, N. Chevanan, and S. Sokhansanj. Comminution properties of biomass in hammer mill and its particle size characterization. In *American Society of Agricultural and Biological Engineers Annual International Meeting 2008*, volume 3, pages 1779–1800, 2008.

[36] K. M. Djamarani and I. M. Clark. Characterization of particle size based on fine and coarse fractions. *Powder Technology*, 93(2):101–108, 1997.

[37] Henk G. Merkus. *Particle size measurements: Fundamentals, practice, quality*. Springer, The Netherlands, 2009.

[38] X. Renliang. *Particle characterization: Light scattering methods*. Kluwer academic publishers, AH Dordrecht, The Netherlands, 2000.

[39] A. Khoshmanesh, R. Sharma, and R. Beckett. Biomass of sediment bacteria by sedimentation field-flow fractionation. *Journal of Environmental Engineering*, 127(1):19–25, 2001.

[40] J. W. Sibley. A study of soil particle characteristics and post-depositional processes in a deagon (queensland, australia) clay profile. *Engineering Geology*, 38(1-2):25–34, 1994.

[41] A. J. Plumpton and L. Heymann. Centrifugal air classification of finely-sized industrial minerals. In *Preprint - Society of Mining Engineers of AIME*, 1990.

[42] T. F. Dumm and R. Hogg. Particle size distribution of airborne dust in coal mines. pages 510–516, 1987.

[43] S. A. Vogelaar, D. Posthuma, D. Boomsma, and C. Kluft. Blood sample stability at room temperature for counting red and white blood cells and platelets. *Vasc. Pharmacol.*, 39(3):123–125, 2002.

[44] M. C. Phelan and G. Lawler. Cell counting. *Current protocols in cytometry / editorial board, J. Paul Robinson, managing editor ... [et al.]*, Appendix 3, 2001.

[45] G. Mernier, N. Piacentini, R. Tornay, N. Buffi, and P. Renaud. Cell viability assessment by flow cytometry using yeast as cell model. *Sens. Actuators, B*, 2009.

[46] J. F. Drake and H. M. Tsuchiya. Differential counting in mixed cultures with coulter counters. *J. Appl. Microbiol.*, 26(1):9–13, 1973.

[47] B. R. Robertson, D. K. Button, and A. L. Koch. Determination of the biomasses of small bacteria at low concentrations in a mixture of species with forward light scatter measurements by flow cytometry. *Appl. Environ. Microbiol.*, 64(10):3900–3909, 1998.

[48] M. D. Persidsky, V. Richards, and J. Leef. Volume changes in bone marrow and ehrlich ascites cells after freezing as an index of preservation efficiency. *Cryobiology*, 3(2):59–67, 1966.

[49] A. D. Randolph and K. Rajagopal. Direct measurement of crystal nucleation and growth rate kinetics in a backmixed crystal slurry: Study of the K2SO4 system. *Ind. Eng. Chem. Fundam.*, 9(1):165–171, 1970.

[50] R. D. Rovang and A. D. Randolph. On-line particle size analysis in the fines loop of a KCI crystallizer. *AIChE Symposium Series*, 76(193):18–26, 1980.

[51] T. Allen. *Particle size measurement*. Chapman and Hall, New York, USA, 1981.

[52] N. G. Stanely-Wood and R. W. Lines. *Particle size analysis*. Royal Society of Chemistry, Cambridge, UK, 1992.

[53] U. Yucel and J. N. Coupland. Ultrasonic attenuation measurements of the mixing, agglomeration, and sedimentation of sucrose crystals suspended in oil. *JAOCS, Journal of the American Oil Chemists' Society*, 88(1):33–38, 2011.

[54] M. N. K. Prakash and K. V. R. Ramana. Ultrasound and its application in the food industry. *Journal of Food Science and Technology*, 40(6):563–570, 2003.

[55] A. Shukla, A. Prakash, and S. Rohani. Online measurement of particle size distribution during crystallization using ultrasonic spectroscopy. *Chemical Engineering Science*, 65(10):3072–3079, 2010.

[56] P. Mougin, A. Thomas, D. Wilkinson, G. White, K. J. Roberts, N. Herrmann, R. Jack, and R. Tweedie. On-line monitoring of a crystallization process. *AIChE Journal*, 49(2):373–378, 2003.

[57] P. Mougin, D. Wilkinson, and K. J. Roberts. In situ ultrasonic attenuation spectroscopic study of the dynamic evolution of particle size during solution-phase crystallization of urea. *Crystal Growth and Design*, 3(1):67–72, 2003.

[58] P. Mougin, D. Wilkinson, K. J. Roberts, and R. Tweedie. Characterization of particle size and its distribution during the crystallization of organic fine chemical products as measured in situ using ultrasonic attenuation spectroscopy. *Journal of the Acoustical Society of America*, 109(1):274–282, 2001.

[59] A. K. Hipp, B. Walker, M. Mazzotti, and M. Morbidelli. In-situ monitoring of batch crystallization by ultrasound spectroscopy. *Industrial and Engineering Chemistry Research*, 39(3):783–789, 2000.

[60] Ulrich Riebel and Friedrich Loeffler. On-line measurement of particle size distribution and particle concentration in suspensions by ultrasonic spectrometry. *Chemical Engineering and Technology*, 12(6):433–438, 1989.

[61] A. Shukla, A. Prakash, and S. Rohani. Particle size monitoring in dense suspension using ultrasound with an improved model accounting for low-angle scattering. *AIChE Journal*, 56(11):2825–2837, 2010.

[62] F. Lionetto and A. Maffezzoli. Polymer characterization by ultrasonic wave propagation. *Advances in Polymer Technology*, 27(2):63–73, 2008.

[63] L. Cavin, A. Renken, and Th Meyer. On-line conversion monitoring through ultrasound velocity measurements in bulk styrene polymerization in a recycle reactor - part ii: mathematical model. *Polymer Reaction Engineering*, 8(3):225–240, 2000.

[64] S. Canegallo, M. Apostolo, G. Storti, and M. Morbidelli. On-line conversion monitoring through ultrasound propagation velocity measurements in emulsion polymerization. *Journal of Applied Polymer Science*, 57(11):1333–1346, 1995.

[65] A. Abbas, D. Nobbs, and J. A. Romagnoli. Investigation of on-line optical particle characterization in reaction and cooling crystallization systems. current state of the art. *Meas. Sci. Technol.*, 13(3):349–356, 2002.

[66] B. O'Sullivan, P. Barrett, G. Hsiao, A. Carr, and B. Glennon. In situ monitoring of polymorphic transitions. *Org. Process Res. Dev.*, 7(6):977–982, 2003.

[67] R. Kobayashi, Y. Fujimaki, T. Ukita, and Y. Hiyama. Monitoring of solvent-mediated polymorphic transitions using in situ analysis tools. *Org. Process Res. Dev.*, 10(6):1219–1226, 2006.

[68] B. O'Sullivan and B. Glennon. Application of in situ FBRM and ATR-FTIR to the monitoring of the polymorphic transformation of D-mannitol. *Org. Process Res. Dev.*, 9(6):884–889, 2005.

[69] P. Barrett and B. Glennon. Characterizing the metastable zone width and solubility curve using lasentec FBRM and PVM. *Chem. Eng. Res. Des.*, 80(7):799–805, 2002.

[70] P. Barrett and B. Glennon. In-line FBRM monitoring of particle size in dilute agitated suspensions. *Part. Part. Syst. Char.*, 16(5):207–211, 1999.

[71] R. A. Williams, S. J. Peng, and A. Naylor. In situ measurement of particle aggregation and breakage kinetics in a concentrated suspension. *Powder Technology*, 73(1):75–83, 1992.

[72] P. Jeffers, S. Raposo, M. E. Lima-Costa, P. Connolly, B. Glennon, and P. M. Kieran. Focussed beam reflectance measurement (fbrm) monitoring of particle size and morphology in suspension cultures of morinda citrifolia and centaurea calcitrapa. *Biotechnology Letters*, 25(23):2023–2028, 2003.

[73] G. Rudolph, P. Lindner, A. Bluma, K. Joeris, G. Martinez, B. Hitzmann, and T. Scheper. Optical inline measurement procedures for counting and sizing cells in bioprocess technology, 2010.

[74] A. P. Pearson, B. Glennon, and P. M. Kieran. Comparison of morphological characteristics of streptomyces natalensis by image analysis and focused beam reflectance measurement. *Biotechnology Progress*, 19(4):1342–1347, 2003.

[75] Erik F. Hobbel, Reg Davies, Foster W. Rennie, Terence Allen, Larry E. Butler, Edward R. Waters, James T. Smith, and Robert W. Sylvester. Modern methods of on-line size analysis for particulate process streams. *Particle and Particle Systems Characterization*, 8(1):29–34, 1991.

[76] J. Jager, H. J. M. Kramer, E. J. De Jong, and S. De Wolf. On-line particle size measurement in dense slurries. *Powder Technology*, 62(2):155–162, 1990.

[77] A. Ruf, J. Worlitschek, and M. Mazzotti. Modeling and experimental analysis of PSD measurements through FBRM. *Part. Part. Syst. Char.*, 17(4):167–179, 2000.

[78] W. Yu and K. Erickson. Chord length characterization using focused beam reflectance measurement probe - methodologies and pitfalls. *Powder Technol.*, 185(1):24–30, 2008.

[79] M. Li, D. Wilkinson, and K. Patchigolla. Obtaining particle size distribution from chord length measurements. *Part. Part. Syst. Char.*, 23(2):170–174, 2006.

[80] M. Li and D. Wilkinson. Determination of non-spherical particle size distribution from chord length measurements. part 1: Theoretical analysis. *Chem. Eng. Sci.*, 60(12):3251–3265, 2005.

[81] N. Kail, W. Marquardt, and H. Briesen. Estimation of particle size distributions from focused beam reflectance measurements based on an optical model. *Chem. Eng. Sci.*, 64(5):984–1000, 2009.

[82] A. R. Heath, P. D. Fawell, P. A. Bahri, and J. D. Swift. Estimating average particle size by focused beam reflectance measurement (fbrm). *Particle and Particle Systems Characterization*, 19(2):84–95, 2002.

[83] O. Monnier, J. P. Klein, C. Hoff, and B. Ratsimba. Particle size determination by laser reflection: Methodology and problems. *Particle and Particle Systems Characterization*, 13(1):10–17, 1996.

[84] A. Tadayyon and S. Rohani. Determination of particle size distribution by partec 100: Modeling and experimental results. *Particle and Particle Systems Characterization*, 15(3):127–135, 1998.

[85] D. B. Patience and J. B. Rawlings. Particle-shape monitoring and control in crystallization processes. *AIChE J.*, 47(9):2125–2130, 2001.

[86] P. A. Larsen, J. B. Rawlings, and N. J. Ferrier. Model-based object recognition to measure crystal size and shape distributions from in situ video images. *Chem. Eng. Sci.*, 62(5):1430–1441, 2007.

[87] J. Calderon De Anda, X. Z. Wang, X. Lai, and K. J. Roberts. Classifying organic crystals via in-process image analysis and the use of monitoring charts to follow polymorphic and morphological changes. *J. of Process Control*, 15(7):785–797, 2005.

[88] X. Z. Wang, K. J. Roberts, and C. Ma. Crystal growth measurement using 2D and 3D imaging and the perspectives for shape control. *Chem. Eng. Sci.*, 63(5):1173–1184, 2008.

[89] D. Sarkar, D. Xuan-Tien, and R. Ying, Z.and Srinivasan. In situ particle size estimation for crystallization processes by multivariate image analysis. *Chem. Eng. Sci.*, 64(1):9–19, 2009.

[90] Y. Zhou, R. Srinivasan, and S. Lakshminarayanan. Critical evaluation of image processing approaches for real-time crystal size measurements. *Comput. Chem. Eng.*, 33(5):1022–1035, 2009.

[91] J. Chen and X. Z. Wang. A wavelet method for analysis of droplet and particle images for monitoring heterogeneous processes. *Chemical Engineering Communications*, 192(4-6):499–515, 2005.

[92] W. N. Al Nasser, A. Shaikh, C. Morriss, M. J. Hounslow, and A. D. Salman. Determining kinetics of calcium carbonate precipitation by inline technique. *Chemical Engineering Science*, 63(5):1381–1389, 2008.

[93] D. Lu. Detection and substitution of clouds/hazes and their cast shadows on ikonos images. *International Journal of Remote Sensing*, 28(18):4027–4035, 2007.

[94] B. Bujak and M. Bottlinger. Three-dimensional measurement of particle shape. *Part. Part. Syst. Char.*, 25(4):293–297, 2008.

[95] M. Kempkes, J. Eggers, and M. Mazzotti. Measurement of particle size and shape by fbrm and in situ microscopy. *Chem. Eng. Sci.*, 63(19):4656–4675, 2008.

[96] D. E. Bugay. Characterization of the solid-state: Spectroscopic techniques. *Adv. Drug Delivery Rev.*, 48(1):43–65, 2001.

[97] B. Rodriguez-Spong, C. P. Price, A. Jayasankar, A. J. Matzger, and N. Rodriguez-Hornedo. General principles of pharmaceutical solid polymorphism: A supramolecular perspective. *Advanced Drug Delivery Reviews*, 56(3):241–274, 2004.

[98] U. Schnars and W. Jueptner. *Digital Holography: Digital Hologram Recording, Numerical Reconstruction, and Related Techniques*. Springer, Berlin, 2005.

[99] V. R. Singh, J. Miao, Z. Wang, G. Hegde, and A. Asundi. Dynamic characterization of mems diaphragm using time averaged in-line digital holography. *Opt. Commun.*, 280(2):285–290, 2007.

[100] V. R. Singh and A. Asundi. In-line digital holography for dynamic metrology of mems. *Chinese Optics Letters*, 7(12):1117–1122, 2009.

[101] W. Xu, M. H. Jericho, I. A. Meinertzhagen, and H. J. Kreuzer. Digital in-line holography for biological applications. *Proceedings of the National Academy of Sciences of the United States of America*, 98(20):11301–11305, 2001.

[102] M. Malek, D. Lebrun, and D. Allano. Digital in-line holography system for 3D-3C particle tracking velocimetry. In *Particle Image Velocimetry*, pages 155–170. 2008.

[103] G. Shen and R. Wei. Digital holography particle image velocimetry for the measurement of 3Dt-3c flows. *Opt. Lasers Eng.*, 43(10):1039–1055, 2005.

[104] C. S. Vikram. *Particle field holography*. Cambridge University Press, Cambridge, UK, 1992.

[105] S. Murata and N. Yasuda. Potential of digital holography in particle measurement. *Opt. Laser Technol.*, 32(7-8):567–574, 2000.

[106] C. Buraga-Lefebvre, S. Coetmellec, D. Lebrun, and C. Ozkul. Application of wavelet transform to hologram analysis: Three-dimensional location of particles. *Opt. Lasers Eng.*, 33(6):409–421, 2000.

[107] W. Xu, M. H. Jericho, I. A. Meinertzhagen, and H. J. Kreuzer. Digital in-line holography of microspheres. *Appl. Opt.*, 41(25):5367–5375, 2002.

[108] L. Denis, C. Fournier, T. Fournel, C. Ducottet, and D. Jeulin. Direct extraction of the mean particle size from a digital hologram. *Appl. Opt.*, 45(5):944–952, 2006.

[109] J. Sheng, E. Malkiel, and J. Katz. Digital holographic microscope for measuring three-dimensional particle distributions and motions. *Appl. Opt.*, 45(16):3893–3901, 2006.

[110] V. R. Singh, G. Hegde, and A. Asundi. Particle field imaging using digital in-line holography. *Curr. Sci.*, 96(3):391–397, 2009.

[111] G. Haussmann and W. Lauterborn. Determination of size and position of fast moving gas bubbles in liquids by digital 3-D image processing of hologram reconstructions. *Appl. Opt.*, 19(20):3529–3535, 1980.

[112] M. Malek, S. Coetmellec, D. Allano, and D. Lebrun. Formulation of in-line holography process by a linear shift invariant system: Application to the measurement of fiber diameter. *Opt. Commun.*, 223(4-6):263–271, 2003.

[113] L. Denis, T. Fournel, C. Fournier, and D. Jeulin. Reconstruction of the rose of directions from a digital microhologram of fibres. *Journal of Microscopy*, 225(3):283–292, 2007.

[114] D. Lebrun, A. Benkouider, S. Cotmellec, and M. Malek. Particle field digital holographic reconstruction in arbitrary tilted planes. *Opt. Express*, 11(3):224–229, 2003.

[115] L. Xu, X. Peng, Z. Guo, J. Miao, and A. Asundi. Imaging analysis of digital holography. *Opt. Express*, 13(7):2444–2452, 2005.

[116] J. Garcia-Sucerquia, W. Xu, S. K. Jericho, P. Klages, M. H. Jericho, and H. J. Kreuzer. Digital in-line holographic microscopy. *Appl. Opt.*, 45(5):836–850, 2006.

[117] T. M. Kreis, M. Adams, and W. Jueptner. Methods of digital holography: a comparison. *Opt. Ins. Micromeas. II*, 3098(1):224–233, 1997.

[118] T. Kreis and W. Adams, M.and Jueptner. Digital in-line holography in particle measurement. *Proceedings of SPIE - The International Society for Optical Engineering*, 3744:54–64, 1999.

[119] V. R. Asundi, A.; Singh. Circle of holographydigital in-line holography for imaging, microscopy and measurement. *J. Hologr. Speckle*, 3:106–111, 2006.

[120] E. Darakis, T. Khanam, A. Rajendran, V. Kariwala, T. J. Naughton, and A. K. Asundi. Microparticle characterization using digital holography. *Chem. Eng. Sci.*, 65(2):1037–1044, 2010.

[121] T. Khanam, E. Darakis, A. Rajendran, V. Kariwala, A. K. Asundi, and T. J. Naughton. On-line digital holographic measurement of size and shape of microparticles for crystallization processes. In *Proceedings of SPIE - The International Society for Optical Engineering*, volume 7155, 2008.

[122] E. Darakis, T. Khanam, A. Rajendran, V. Kariwala, A. K. Asundi, and T. J. Naughton. Processing of digital holograms for size measurements of microparticlese. In *Ninth International Symposium on Laser Metrology*, volume 7155, pages 715524–12. SPIE, 2008.

[123] S. Soontaranon, J. Widjaja, and T. Asakura. Extraction of object position from in-line holograms by using single wavelet coefficient. *Opt. Commun.*, 281(6):1461–1467, 2008.

[124] E. Malkiel, J. N. Abras, and J. Katz. Automated scanning and measurements of particle distributions within a holographic reconstructed volume. *Meas. Sci. Technol.*, 15(4):601–612, 2004.

[125] J. Calderon De Anda, X. Z. Wang, and K. J. Roberts. Multi-scale segmentation image analysis for the in-process monitoring of particle shape with batch crystallisers. *Chem. Eng. Sci.*, 60(4):1053–1065, 2005.

[126] J. Canny. Computational approach to edge detection. *IEEE Transactions on Pattern Analysis and Machine Intelligence*, PAMI-8(6):679–698, 1986.

[127] C. P. McElhinney, B. M. Hennelly, and T. J. Naughton. Extended focused imaging for digital holograms of macroscopic three-dimensional objects. *Appl. Optics*, 47(19), 2008.

[128] Anonymous. Application Note: Particle size and shape measurement using image analysis. *Malvern Instruments*, Image analysis application note, MRK664-01.

[129] J. Eggers, M. Kempkes, and M. Mazzotti. Measurement of size and shape distributions of particles through image analysis. *Chem. Eng. Sci.*, 2008.

[130] P. A. Larsen and J. B. Rawlings. The potential of current high-resolution imaging-based particle size distribution measurements for crystallization monitoring. *AIChE J.*, 55(4):896–905, 2009.

[131] M. Kempkes, E. Darakis, T. Khanam, A. Rajendran, V. Kariwala, M. Mazzotti, T. J. Naughton, and A. K. Asundi. Three dimensional digital holographic profiling of micro-fibers. *Opt. Express*, 17(4):2938–2943, 2009.

[132] S. Wold, K. Esbensen, and P. Geladi. Principal component analysis. *Chemom. Intell. Lab. Syst.*, 2(1-3):37–52, 1987.

[133] R. F. Li, G. B. Thomson, G. White, X. Z. Wang, J. C. De Anda, and K. J. Roberts. Integration of crystal morphology modeling and on-line shape measurement. *AIChE J.*, 52(6):2297–2305, 2006.

[134] S. Aslananian and I. Kostov. Einflu der bersttigung auf den habitus der kristalle von oxalsure. *Krist. Tech.*, 7(5):511–518, 1972.